University of Alberta

Water-Dispersible Magnetic Particle-Graphene Oxide Composites: Synthesis, Characterization and Application in the Removal of Selenium Oxyanions

by

You Fu

A thesis submitted to the Faculty of Graduate Studies and Research
in partial fulfillment of the requirements for the degree of

Master of Science
in
Chemical Engineering

Department of Chemical and Materials Engineering

Spring 2014
Edmonton, Alberta

ABSTRACT

Selenium is toxic in excess with a high mobility in water. Existing adsorbents only show some removal capacity for selenite but perform poorly (typical removal percentage < 50 %) for selenate, the more bioavailable and soluble species. In this thesis, two Magnetic particle-Graphene Oxide composites (MGOs) were synthesized, characterized and applied to selenium removal from simulated water, with an significant removal percentage of > 99.9 % for selenite and 80 – 95 % for selenate at pH ~ 6 within 10 seconds. Acidic pH and low temperature could enhance the selenium adsorption on MGOs. It is proposed that the selenium adsorption on MGOs involves the formation of inner-sphere and outer-sphere complexes. MGOs can be separated effectively under an external magnetic field and recycle. Our results show that MGOs composites have excellent removal capability of selenite and selenate from simulated water and can be applied for the removal of selenium from wastewater.

ACKNOWLEDGEMENT

Looking back on the past two and a half years, challenging as the projects seem like, unknown as the way the world is, I am still grateful and possessing the courage to conquer all the difficulties in my life journey, because of all the encouraging words, selfless help, tears and laughter we shared.

I would like to express my gratitude to my supervisors, Professor Qingxia (Chad) Liu and Professor Hongbo Zeng, for all their support, trust and guidance. Professor Liu is an excellent scholar with abundant industry experience. His insights and understanding of the projects have great inspiration on me. Professor Zeng’s personal charm and profound knowledge makes him my role model. He would always spare time to help me to make the idea clear, no matter in conducting experiment, writing articles, or time management.

At the same time, my thanks to Dr. Jingyi Wang, a respectable mentor and friend, for her endless help and company for my research and life; my colleagues, Ling Zhang, Kaiwen Liu, Yaguan Ji, Peiling Sun, Dr. Qingye Lu, Jun Huang, Andreas Kusuma, Jing Wang, Haipeng Li, Meijiao Deng, Dr. Zhenzhen Lu and all the other group members, for all the help, encouragement and discussions which I benefit a lot from; and my summer students, Junmeng Li, Junchen Yan, Eric Gao, and Yves Lai, for their hard work on the experiment.

I would also like to acknowledge Dr. Jian Chen, for the delightful collaboration, technical support and friendship; Dr. Shihong Xu, Dr. Anqiang He, Dr. Guangcheng Chen, Dr. Xin Zhang, Dr. Nancy Zhang, Dr. Xuejun Sun, Dr. Shiau-Yin Wu, Dr. Jie Ru, Dr. Shiraz Merali, Dr. Ni Yang, Dr. Xinsong Lin and

Dr. Mingsheng Ma for all the technical support in the characterization instruments.

My appreciations to Ms. Patricia Siferd, for her kind help for me and the whole group; to Mr. Kevin Heidebrecht and Mr. Clark Bicknell from the machine shop; to Ms. Marion Pritchard and Ms. Lily Laser for the kind office help.

Here I want to express my acknowledgement to our sponsor, Teck Resources Ltd., Natural Sciences and Engineering Research Council of Canada (NSERC) and Canada Foundation for Innovation (CFI).

Last but not least, I would like to donate my special thanks to my family for their support from the very beginning; to my dear boyfriend for his care; and my friends for being there for me all the time.

TABLE OF CONTENTS

Chapter 1 Introduction 1

1.1 Background of Selenium Pollution and Toxicity in the Environment 1

1.2 Water Chemistry of Selenium Oxyanions in Aqueous System 3

1.3 Selenium Management Methods and Technologies 6

1.3.1 Precipitation 6

1.3.1.1 Precipitation with Ferric-chloride 7

1.3.1.2 Precipitation with Ferrous Hydroxides 7

1.3.1.3 Lime Softening 9

1.3.2 Ion Exchange (IX) 10

1.3.3 Solvent extraction (SX) 12

1.3.4 Reverse Osmosis (RO) 12

1.3.5 Nanofiltration 13

1.3.6 Emulsion Liquid Membranes 15

1.3.7 Oxidation 16

1.3.8 Reduction Process 17

1.3.8.1 Reduction with Ferrous Hydroxide 17

1.3.8.2 Reduction with Zero-Valent Iron (ZVI) 19

1.3.8.3 Biological Reduction 20

1.3.9 Biological Treatment 22

1.3.10 Adsorption 23

1.3.10.1 Adsorption with Ferric-chloride 23

1.3.10.2 Adsorption with Activated Alumina (AA)........................ 24

1.3.10.3 Adsorption with Activated Carbon (AC) 25

1.3.10.4 Challenging with Adsorption Method and Commonly-used Adsorbents 25

1.3.11 Summary of Advantages and Disadvantages of Different Selenium Treatment Technologies 27

1.4 Graphene/Graphene Oxide (GO) Based Adsorbents 29

1.4.1 Advantages of Graphene/Graphene Oxide (GO) Based Adsorbents 29

1.4.2 Challenges in Graphene/Graphene Oxide (GO) Based Adsorbents 31

1.5 Nano Iron Oxide Adsorbent 31

1.5.1 Magnetic Carrier Technology (MCT) 31

1.5.2 Iron Oxides: Affinity with High Valence Selenium Oxyanions . 33

1.6 Design and Scope 36

1.7 Outline of This Thesis 38

1.8 References 39

Chapter 2 Experimental Section 53

2.1 Chemicals 53

2.1 Adsorbents Synthesis 53

2.1.1 Preparation of GO 53

2.1.2 Preparation of MGO 54

2.1.3 Preparation of MGO-EG 54

2.2 Selenium Adsorption Experiments........ 55

2.3 Characterization Methods 56

2.3.1 AFM 56

2.3.2 XRD 59

2.3.3 FTIR 61

2.3.4 XPS........ 64

2.3.5 TGA........ 65

2.3.6 TEM 67

2.3.7 SEM........ 69

2.3.8 Magnetic properties measurement........ 70

2.3.9 Zeta potential measurement........ 71

2.3.10 ICP-MS........ 73

2.3.11 IC........ 75

2.4 References........ 75

Chapter 3 Water-Dispersible Magnetic Nanoparticle−Graphene Oxide Composites for Selenium Removal........ 82

3.1 Introduction........ 82

3.2 Results and Discussion 84

3.2.1 Atomic Force Microscopy (AFM) imaging 85

3.2.2 X-ray diffraction (XRD) analysis........ 86

3.2.3 Fourier Transform Infrared Spectroscopy (FTIR) analysis........ 88

3.2.4 X-ray Photoelectron Spectroscopy (XPS) analysis........ 89

3.2.5 Thermo Gravimetric Analysis (TGA) analysis 92

3.2.6 Characterization by Transmission Electron Microscopy (TEM) and Scanning Electron Microscope (SEM) 93

3.2.7 Magnetic properties of MGO 95

3.2.8 Possible MGO synthesis and selenium adsorption mechanism .. 96

3.2.9 Definition of adsorption capacity Q (mg g^{-1}) and removal percentage q (%) 97

3.2.10 Adsorption curves fitting with Freundlich and Langmuir adsorption Models 99

3.2.11 Effect of pH value on selenium adsorption 100

3.2.12 Kinetics of selenium adsorption on MGO 102

3.2.13 Discussion of possible selenium adsorption mechanism 103

3.2.14 Comparison between MGO, GO and pure Fe_3O_4 particles (400 nm and 10 - 20 nm) for adsorption of selenite and selenate ions at different concentrations. 104

3.2.15 MGO recycling tests 106

3.3 Conclusions 108

3.4 Experimental Section 108

3.4.1 Chemicals and Materials 108

3.4.2 Synthesis of GO 109

3.4.3 Preparation of MGO 110

3.4.4 Adsorption experiment 110

3.4.5 Characterization Methods 111

3.5 Acknowledgements ... 112

3.6 References ... 112

Chapter 4 Removal of High-Valence Selenium Ion with Water-Dispersible Magnetic Particle-Graphene Oxide Composites Reducedby Ethylene Glycol ... 119

4.1 Introduction ... 119

4.2 Experimental Section ... 122

4.2.1 Chemicals ... 122

4.2.2 Synthesis for GO ... 122

4.2.3 Preparation for MGO-EG ... 123

4.2.4 Adsorption experiment ... 123

4.2.5 Characterization Methods ... 124

4.3 Results and Discussion ... 125

4.3.1 Characterization of as synthesized GO and MGO-EG ... 125

4.3.1.1 Atomic Force Microscopy (AFM) imaging ... 125

4.3.1.2 Characterization by Transmission Electron Microscopy (TEM), Scanning Electron Microscope (SEM) and Energy Dispersive Spectrometry (EDS) ... 128

4.3.1.3 X-ray diffraction (XRD) analysis ... 130

4.3.1.4 Fourier Transform Infrared Spectroscopy (FTIR) analysis 131

4.3.1.5 X-ray Photoelectron Spectroscopy (XPS) analysis ... 132

4.3.1.6 Thermo Gravimetric Analysis (TGA) analysis ... 135

4.3.1.7 Magnetic properties of MGO-EG 136

4.3.2 MGO-EG synthesis mechanism 138

4.3.3 Selenium adsorption tests with MGO-EG................................ 139

4.3.3.1 Definition of adsorption capacity Q (mg g^{-1}) and removal percentage q (%) 140

4.3.3.2 Adsorption curves fitted with Freundlich and Langmuir adsorption Models.. 142

4.3.3.3 Effect of pH value on selenium adsorption....................... 144

4.3.3.4 Kinetics of selenium adsorption on MGO-EG................. 145

4.3.3.5 Effect of adsorption temperature on selenium adsorption 146

4.3.3.6 Comparison between MGO, GO and pure Fe_3O_4 particles (400 nm and 10 - 20 nm) for adsorption of selenite and selenate ions at different concentrations. 148

4.3.4 Selenium adsorption mechanism with MGO-EG..................... 150

4.3.5 MGO-EG recycling tests 153

4.3.6 Effects of Interfering ions... 155

4.3.6.1 Effects of Interfering ions of different initial concentrations 155

4.3.6.2 Effects of Interfering ions under different pH.................. 161

4.4 Conclusions... 166

4.5 References.. 167

Chapter 5 Conclusions and Future Work... 173

5.1 Conclusions... 173

5.2 Future Work 176

5.2.1 Adsorption mechanism study with EXAFS (Extended X-ray Absorption Fine Structure) 176

5.2.2 Surface properties and interaction using AFM and SFA 179

5.2.3 Interfering ions control 180

5.2.4 Universal adsorption potential for other heavy metal ions (Cr^{2+}, Pb^{2+} ,Zn^{2+}, As, Hg^{2+}, Cu^{2+}, etc.) and organic dyes 180

5.3 References 181

Appendix 184

LIST OF TABLES

Table 1-1 Global selenium fluxes. 2

Table 1-2 Chemical states of selenium in the environment. 4

Table 1-3 Comparison between other adsorbents (the uncited data are obtained in this work with initial selenium concentration: 10 ppm). 26

Table 1-4 Selenium treatment methods and their advantages and disadvantages. 27

Table 1-5 Selenium removal ability of different types of iron oxides. 34

Table 3-1 Freundlich and Langmuir adsorption isotherm parameters for adsorption of Se (IV) and Se (VI) ions on MGO. 100

Table 4-1 Freundlich and Langmuir adsorption isotherm parameters for Se (IV) and Se (VI) adsorption on MGO-EG. 144

Appendix 1 Selenite concentration after adsorption with MGO with different initial selenite concentration. MGO dosage 1 g L^{-1}, under neutral pH (~ 6), room temperature (~ 25 ℃), shaking rate 300 rpm, adsorption time for 24 hours. 184

Appendix 2 Selenate concentration after adsorption with MGO with different initial selenite concentration. MGO dosage 1 g L^{-1}, under neutral pH (~ 6), room temperature (~ 25 ℃), shaking rate 300 rpm, adsorption time for 24 hours. 185

Appendix 3 Effect of pH on selenite adsorption: MGO dosage 1 g L^{-1}, initial selenium concentration 300 ppb room temperature (~ 25 ℃), shaking rate 300 rpm, adsorption time for 24 hours. 186

Appendix 4 Effect of pH on selenate adsorption: MGO dosage 1 g L^{-1}, initial selenium concentration 300 ppb room temperature (~ 25 ℃), shaking rate 300 rpm, adsorption time for 24 hours. 186

Appendix 5 Effect of adsorption time on selenite adsorption: MGO dosage 1 g L^{-1}, under neutral pH (~ 6), initial selenium concentration 300 ppb, room temperature (~ 25 ℃), shaking rate 300 rpm.. 187

Appendix 6 Effect of adsorption time on selenate adsorption: MGO dosage 1 g L^{-1}, under neutral pH (~ 6), initial selenium concentration 300 ppb, room temperature (~ 25 ℃), shaking rate 300 rpm.. 188

Appendix 7 Removal percentage of selenite with different recycle times. Recycle was done using acid-washing method. Tests were done at: MGO dosage 1 g L^{-1}, under neutral pH (~ 6), initial selenium concentration 300 ppb, room temperature (~ 25 ℃), shaking rate 300 rpm, adsorption time for 24 hours. 189

Appendix 8 Removal percentage of selenate with different recycle times. Recycle was done using acid-washing method. Tests were done at: MGO dosage 1 g L^{-1}, under neutral pH (~ 6), initial selenium concentration 300 ppb, room temperature (~ 25 ℃), shaking rate 300 rpm, adsorption time for 24 hours. 190

Appendix 9 Selenite concentration after adsorption with MGO-EG with different initial selenite concentration. MGO-EG dosage 1 g L^{-1}, under neutral pH (~ 6), room temperature (~ 25 ℃), shaking rate 300 rpm, adsorption time for 24 hours. 191

Appendix 10 Selenate concentration after adsorption with MGO-EG with different initial selenate concentration. MGO-EG dosage 1 g L^{-1}, under neutral pH (~ 6), room temperature (~ 25 ℃), shaking rate 300 rpm, adsorption time for 24 hours... 192

Appendix 11 Effect of pH on selenite adsorption: MGO-EG dosage 1 g L^{-1}, initial selenium concentration 300 ppb room temperature (~ 25 ℃), shaking rate 300 rpm, adsorption time for 24 hours. 193

Appendix 12 Effect of pH on selenate adsorption: MGO-EG dosage 1 g L^{-1}, initial selenium concentration 300 ppb room temperature (~ 25 ℃), shaking rate 300 rpm, adsorption time for 24 hours. 194

Appendix 13 Effect of adsorption time on selenite adsorption: MGO-EG dosage 1 g L^{-1}, under neutral pH (~ 6), initial selenium concentration 300 ppb, room temperature (~ 25 ℃), shaking rate 300 rpm. 195

Appendix 14 Effect of adsorption time on selenate adsorption: MGO-EG dosage 1 g L^{-1}, under neutral pH (~ 6), initial selenium concentration 300 ppb, room temperature (~ 25 ℃), shaking rate 300 rpm. 196

Appendix 15 Effect of adsorption temperature on selenite adsorption: MGO-EG dosage 1 g L^{-1}, under neutral pH (~ 6), initial selenium concentration 300 ppb, shaking rate 300 rpm, adsorption time for 24 hours. 197

Appendix 16 Effect of adsorption temperature on selenate adsorption: MGO-EG dosage 1 g L^{-1}, under neutral pH (~ 6), initial selenium concentration 300 ppb, shaking rate 300 rpm, adsorption time for 24 hours. 198

Appendix 17 Removal percentage of selenite with different recycle times. Recycle was done using acid-washing method. Tests were done at: MGO-EG dosage 1 g L^{-1}, under neutral pH (~ 6), initial selenium concentration 300 ppb, room temperature (~ 25 ℃), shaking rate 300 rpm, adsorption time for 24 hours. 199

Appendix 18 Removal percentage of selenate with different recycle times. Recycle was done using acid-washing method. Tests were done at: MGO-EG dosage 1 g L^{-1}, under neutral pH (~ 6), initial selenium concentration 300 ppb, room temperature (~ 25 ℃), shaking rate 300 rpm, adsorption time for 24 hours. 200

Appendix 19 Selenite and Ca^{2+} removal percentage by MGO-EG with different initial Ca^{2+} concentrations. Tests were done at: MGO-EG dosage 1 g L^{-1}, under neutral pH (~ 6), initial selenium concentration 300 ppb, room temperature (~ 25 ℃), shaking rate 300 rpm, adsorption time for 24 hours........ 201

Appendix 20 Selenate and Ca^{2+} removal percentage by MGO-EG with different initial Ca^{2+} concentrations. Tests were done at: MGO-EG dosage 1 g L^{-1}, under neutral pH (~ 6), initial selenium concentration 300 ppb, room temperature (~ 25 ℃), shaking rate 300 rpm, adsorption time for 24 hours........ 202

Appendix 21 Selenite and Mg^{2+} removal percentage by MGO-EG with different initial Mg^{2+} concentrations. Tests were done at: MGO-EG dosage 1 g L^{-1}, under neutral pH (~ 6), initial selenium concentration 300 ppb, room temperature (~ 25 ℃), shaking rate 300 rpm, adsorption time for 24 hours........ 203

Appendix 22 Selenate and Mg^{2+} removal percentage by MGO-EG with different initial Mg^{2+} concentrations. Tests were done at: MGO-EG dosage 1 g L^{-1}, under neutral pH (~ 6), initial selenium concentration 300 ppb, room temperature (~ 25 ℃), shaking rate 300 rpm, adsorption time for 24 hours........ 204

Appendix 23 Selenite and NO_3^- removal percentage by MGO-EG with different initial NO_3^- concentrations. Tests were done at: MGO-EG dosage 1 g L^{-1}, under neutral pH (~ 6), initial selenium concentration 300 ppb, room temperature (~ 25 ℃), shaking rate 300 rpm, adsorption time for 24 hours.................................. 205

Appendix 24 Selenate and NO_3^- removal percentage by MGO-EG with different initial NO_3^- concentrations. Tests were done at: MGO-EG dosage 1 g L^{-1}, under neutral pH (~ 6), initial selenium concentration 300 ppb, room temperature (~ 25 ℃), shaking rate 300 rpm, adsorption time for 24 hours.................................. 206

Appendix 25 Selenite and SO_4^{2-} removal percentage by MGO-EG with different initial SO_4^{2-} concentrations. Tests were done at: MGO-EG dosage 1 g L^{-1}, under neutral pH (~ 6), initial selenium concentration 300 ppb, room temperature (~ 25 ℃), shaking rate 300 rpm, adsorption time for 24 hours.................................. 207

Appendix 26 Selenate and SO_4^{2-} removal percentage by MGO-EG with different initial SO_4^{2-} concentrations. Tests were done at: MGO-EG dosage 1 g L^{-1}, under neutral pH (~ 6), initial selenium concentration 300 ppb, room temperature (~ 25 ℃), shaking rate 300 rpm, adsorption time for 24 hours.................................. 208

Appendix 27 Selenite and PO_4^{3-} removal percentage by MGO-EG with different initial PO_4^{3-} concentrations. Tests were done at: MGO-EG dosage 1 g L^{-1}, under neutral pH (~ 6), initial selenium concentration 300 ppb, room temperature (~ 25 ℃), shaking rate 300 rpm, adsorption time for 24 hours.................................. 209

Appendix 28 Selenate and PO_4^{3-} removal percentage by MGO-EG with different initial PO_4^{3-} concentrations. Tests were done at: MGO-EG dosage 1 g L^{-1}, under neutral pH (~ 6), initial selenium concentration 300 ppb, room temperature (~ 25 ℃), shaking rate 300 rpm, adsorption time for 24 hours.................................. 210

Appendix 29 Selenite and Ca^{2+} removal percentage by MGO-EG with different pH. Tests were done at: MGO-EG dosage 1 g L^{-1}, initial selenium concentration 300 ppb, room temperature (~ 25 ℃), shaking rate 300 rpm, adsorption time for 24 hours. 211

Appendix 30 Selenate and Ca^{2+} removal percentage by MGO-EG with different pH. Tests were done at: MGO-EG dosage 1 g L^{-1}, initial selenium concentration 300 ppb, room temperature (~ 25 ℃), shaking rate 300 rpm, adsorption time for 24 hours. 212

Appendix 31 Selenite and Mg^{2+} removal percentage by MGO-EG with different pH. Tests were done at: MGO-EG dosage 1 g L^{-1}, initial selenium concentration 300 ppb, room temperature (~ 25 ℃), shaking rate 300 rpm, adsorption time for 24 hours. 213

Appendix 32 Selenate and Mg^{2+} removal percentage by MGO-EG with different pH. Tests were done at: MGO-EG dosage 1 g L^{-1}, initial selenium concentration 300 ppb, room temperature (~ 25 ℃), shaking rate 300 rpm, adsorption time for 24 hours. 214

Appendix 33 Selenite and NO_3^- removal percentage by MGO-EG with different pH. Tests were done at: MGO-EG dosage 1 g L^{-1}, initial selenium concentration 300 ppb, room temperature (~ 25 ℃), shaking rate 300 rpm, adsorption time for 24 hours. 215

Appendix 34 Selenate and NO_3^- removal percentage by MGO-EG with different pH. Tests were done at: MGO-EG dosage 1 g L^{-1}, initial selenium concentration

300 ppb, room temperature (~ 25 ℃), shaking rate 300 rpm, adsorption time for 24 hours.. 216

Appendix 35 Selenite and SO_4^{2-} removal percentage by MGO-EG with different pH. Tests were done at: MGO-EG dosage 1 g L^{-1}, initial selenium concentration 300 ppb, room temperature (~ 25 ℃), shaking rate 300 rpm, adsorption time for 24 hours.. 217

Appendix 36 Selenate and SO_4^{2-} removal percentage by MGO-EG with different pH. Tests were done at: MGO-EG dosage 1 g L^{-1}, initial selenium concentration 300 ppb, room temperature (~ 25 ℃), shaking rate 300 rpm, adsorption time for 24 hours.. 218

Appendix 37 Selenite and PO_4^{3-} removal percentage by MGO-EG with different pH. Tests were done at: MGO-EG dosage 1 g L^{-1}, initial selenium concentration 300 ppb, room temperature (~ 25 ℃), shaking rate 300 rpm, adsorption time for 24 hours.. 219

Appendix 38 Selenate and PO_4^{3-} removal percentage by MGO-EG with different pH. Tests were done at: MGO-EG dosage 1 g L^{-1}, initial selenium concentration 300 ppb, room temperature (~ 25 ℃), shaking rate 300 rpm, adsorption time for 24 hours.. 220

Appendix 39 Selenite concentration after adsorption with MGO-EG with different initial selenite concentration. MGO-EG dosage 1 g L^{-1}, under neutral pH (~ 6), room temperature (~ 25 ℃), shaking rate 300 rpm, adsorption time for 24 hours. 221

Appendix 40 Selenate concentration after adsorption with MGO-EG with different initial selenite concentration. MGO-EG dosage 1 g L^{-1}, under neutral pH (~ 6), room temperature (~ 25 ℃), shaking rate 300 rpm, adsorption time for 24 hours. ... 222

Appendix 41 Selenite concentration after adsorption with MGO with different initial selenite concentration. MGO dosage 1 g L^{-1}, under neutral pH (~ 6), room temperature (~ 25 ℃), shaking rate 300 rpm, adsorption time for 24 hours. ... 223

Appendix 42 Selenate concentration after adsorption with MGO with different initial selenite concentration. MGO dosage 1 g L^{-1}, under neutral pH (~ 6), room temperature (~ 25 ℃), shaking rate 300 rpm, adsorption time for 24 hours. ... 224

Appendix 43 Selenite concentration after adsorption with GO with different initial selenite concentration. GO dosage 1 g L^{-1}, under neutral pH (~ 6), room temperature (~ 25 ℃), shaking rate 300 rpm, adsorption time for 24 hours. ... 225

Appendix 44 Selenate concentration after adsorption with GO with different initial selenite concentration. GO dosage 1 g L^{-1}, under neutral pH (~ 6), room temperature (~ 25 ℃), shaking rate 300 rpm, adsorption time for 24 hours. ... 226

Appendix 45 Selenite concentration after adsorption with Fe_3O_4 (400 nm) with different initial selenite concentration. Fe_3O_4 (400 nm) dosage 1 g L^{-1}, under neutral pH (~ 6), room temperature (~ 25 ℃), shaking rate 300 rpm, adsorption time for 24 hours. ... 227

Appendix 46 Selenate concentration after adsorption with Fe_3O_4 (400 nm) with different initial selenite concentration. Fe_3O_4 (400 nm) dosage 1 g L^{-1}, under neutral pH (~ 6), room temperature (~ 25 ℃), shaking rate 300 rpm, adsorption time for 24 hours. 228

Appendix 47 Selenite concentration after adsorption with Fe_3O_4 (10 - 20 nm) with different initial selenite concentration. Fe_3O_4 (10 - 20 nm) dosage 1 g L^{-1}, under neutral pH (~ 6), room temperature (~ 25 ℃), shaking rate 300 rpm, adsorption time for 24 hours. 229

Appendix 48 Selenate concentration after adsorption with Fe_3O_4 (10 - 20 nm) with different initial selenite concentration. Fe_3O_4 (10 - 20 nm) dosage 1 g L^{-1}, under neutral pH (~ 6), room temperature (~ 25 ℃), shaking rate 300 rpm, adsorption time for 24 hours. 230

LIST OF FIGURES

Figure 1-1 Simplified schematic diagram (adapted from literature[4]) of the cycling of selenium from the environment to man. The main geochemistry and health pathways are shown in red/thicker arrows. 2

Figure 1-2 Buckyballs (bottom left), carbon nanotubes (bottom center) and ten layers graphite (bottom right) all share the same honeycomb polycyclic molecular structure of graphene (top). Figure adapted from literature.[94] 30

Figure 1-3 Diagram of magnetic separation in water treatment process. 33

Figure 1-4 Scheme of MGO synthesis, application stripping and reuse.............. 37

Figure 2-1 Block diagram of AFM using beam deflection detection. 58

Figure 2-2 Diagram of the powder X-ray diffract meter. 61

Figure 2-3 Schematic diagram of a Michelson interferometer, configured for FTIR. 63

Figure 2-4 Principle of XPS (figure adapted from literature[22]). 65

Figure 2-5 Principle of TGA measurement (figure adapted from literature[26]). .. 66

Figure 2-6 Instrument of Transmission Electron Microscope (figure adapted from literature[30]). 68

Figure 2-7 Diagram of SEM imaging. 70

Figure 2-8 Schematic representation of zeta potential... 72

Figure 2-9 Layout of ICP-MS (figure adapted from literature[45])....................... 74

Figure 3-1 Tapping mode AFM image of GO sheets with height profile for mono layer GO (~ 1.03 nm)... 86

Figure 3-2 Powder X-ray diffraction patterns of (a) graphite, (b) GO and (c) MGO. 87

Figure 3-3 FTIR spectra of (a) graphite, (b) GO and (c) MGO. 89

Figure 3-4 XPS patterns of (a) C1s spectra of GO (top) and MGO (bottom), (b) O1s spectra of GO (top) and MGO (bottom); (c) Fe 2p spectra of MGO; (d) Se 3d after Se (IV) (top) and Se (VI) (bottom) adsorption using MGO. 91

Figure 3-5 TGA curves of (a) Graphite, (b) GO, and (c) MGO. 93

Figure 3-6 TEM images of (a) GO, (b) MGO and (c) HRTEM image and selected area diffraction pattern of single magnetic iron oxide particles, marked by yellow square. The up-right inset is the image of the same iron oxide particle after Wiener Filter processing. The diffractogram of the iron oxide is shown on the bottom right side of the image. Diffraction simulation (on top of the diffractogram) using Desktop Microscopist suggests this single iron oxide is $Fe_{2.67}O_4$. The orientation of this particle is [-112].; (d) EDS spectrum indicates the presence of elements O, C, and Fe; (e) EELS spectrum of iron oxide nanoparticles in MGO. 94

Figure 3-7 SEM images of MGO in (a) low magnification and (b) high magnification. 95

Figure 3-8 (a) Magnetic hysteresis loop of MGO with a bottom right inset of a close view of the hysteresis loop. (b) MGO dispersed in selenium containing solution before magnetic separation and (c) The effect of magnetic separation after about ten seconds. 96

Figure 3-9 MGO synthesis process and possible selenium adsorption mechanism. 97

Figure 3-10 (a) Q-C_0 and (b) q-C_0 curves of Se (IV) and Se (VI) adsorption using MGO. 98

Figure 3-11 Fitting curves using Freundlich and Langmuir Models under different (a) Se (IV) and (b) Se (VI) equilibrium concentrations. 100

Figure 3-12 Effect of pH on selenium adsorption, at room temperature (25 ℃), with an adsorption time of 2 h, MGO dosage 1 g L^{-1}, and initial selenium concentration 300 ppb. 101

Figure 3-13 Effect of adsorption time on selenium adsorption, at room temperature (25 ℃), pH ~ 6, MGO dosage 1 g L^{-1}, and initial selenium concentration 300 ppb. 102

Figure 3-14 Comparison between MGO, GO and pure Fe_3O_4 particles (400 nm and 10 - 20 nm) for adsorption of (a) Se (IV) and (b) Se (VI) ions at different concentrations. 106

Figure 3-15 Normalized selenium removal percentage using MGO with different recycle times. Recycle was done using standard acid-base method. Tests were done at room temperature (25 ℃), pH ~ 6, with MGO dosage 1 g L^{-1}, and initial selenium concentration 300 ppb. 107

Figure 4-1 Tapping mode AFM image of GO sheets with height profile for mono layer GO (~ 1.09 nm). 127

Figure 4-2 TEM images of (a) GO, and (b) MGO-EG. 129

Figure 4-3 SEM images of (a) MGO-EG and (b) EDS spectrum and element content analysis. 129

Figure 4-4 Powder X-ray diffraction patterns of (A) graphite, (B) GO and (C) MGO-EG. 131

Figure 4-5 FTIR spectra of (A) graphite, (B) GO and (C) MGO-EG. 132

Figure 4-6 XPS patterns of (a) C1s, (b) O1s for GO and MGO-EG; (c) GO and MGO-EG survey; (d) Fe 2p; (e) Se 3d after adsorption using MGO-EG. 134

Figure 4-7 TGA curves of (A) Graphite, (B) GO, and (C) MGO-EG. 136

Figure 4-8 (a) Magnetic hysteresis loop of MGO-EG with a bottom inset (b) of a close view of the hysteresis loop. (c) Before and (d) after the magnetic separation after about ten seconds. 138

Figure 4-9 (a) Schematic of graphite structure; (b) schematic of GO structure; (c) schematic of MGO-EG structure; (d) proposed selenite (Se (IV)) and selenate (Se (VI)) adsorption reaction mechanism on MGO-EG; (e) Scheme of MG-EG synthesis, selenium adsorption on MGO-EG, and MGO-EG stripping and reuse. 139

Figure 4-10 (a) Q-C_0 curves with different initial Se (IV) and Se (VI) concentrations. MGO-EG dosage 1 g L^{-1}, under neutral pH (~ 6), room temperature (~ 25 ℃), shaking rate 300 rpm, adsorption time for 24 hours. 141

Figure 4-11 q-C_0 curves with different initial Se (IV) and Se (VI) concentrations. MGO-EG dosage 1 g L^{-1}, under neutral pH (~ 6), room temperature (~ 25 ℃), shaking rate 300 rpm, adsorption time for 24 hours. 142

Figure 4-12 Fitting curves using Freundlich and Langmuir Models under different initial (a) Se (IV) and (b) Se (VI) concentrations.. 143

Figure 4-13 Effect of pH on selenium adsorption: MGO-EG dosage 1 g L^{-1}, initial selenium concentration 300 ppb room temperature (~ 25 °C), shaking rate 300 rpm, adsorption time for 24 hours.. 145

Figure 4-14 Effect of adsorption time on selenium adsorption: MGO-EG dosage 1 g L^{-1}, under neutral pH (~ 6), initial selenium concentration 300 ppb, room temperature (~ 25 °C), shaking rate 300 rpm.. 146

Figure 4-15 Effect of adsorption temperature on selenium adsorption: MGO-EG dosage 1 g L^{-1}, under neutral pH (~ 6), initial selenium concentration 300 ppb, shaking rate 300 rpm, adsorption time for 24 hours. 148

Figure 4-16 Comparison between MGO-EG, GO, pure Fe_3O_4 particles (10 - 20 nm), and pure Fe_3O_4 particles (400 nm) for (a) selenite and (b) selenate adsorption.. 150

Figure 4-17 Zeta potential of MGO-EG, dispersed in water solution. 153

Figure 4-18 Removal percentage of selenium with different recycle times. Recycle was done using acid-washing method. Tests were done at: MGO-EG dosage 1 g L^{-1}, under neutral pH (~ 6), initial selenium concentration 300 ppb, room temperature (~ 25 °C), shaking rate 300 rpm, adsorption time for 24 hours. 154

Figure 4-19 Removal percentages of (a) selenite and (b) selenate in the presence of various interfering ions of different initial concentrations. Tests were done at: MGO-EG dosage 1 g L^{-1}, under neutral pH (~ 6), initial selenium concentration

300 ppb, room temperature (~ 25 ℃), shaking rate 300 rpm, adsorption time for 24 hours.......... 155

Figure 4-20 Selenium and Ca^{2+} removal percentage by MGO-EG with different initial Ca^{2+} concentrations. Tests were done at: MGO-EG dosage 1 g L^{-1}, under neutral pH (~ 6), initial selenium concentration 300 ppb, room temperature (~ 25 ℃), shaking rate 300 rpm, adsorption time for 24 hours.......... 157

Figure 4-21 Selenium and Mg^{2+} removal percentage by MGO-EG with different initial Mg^{2+} concentrations. Tests were done at: MGO-EG dosage 1 g L^{-1}, under neutral pH (~ 6), initial selenium concentration 300 ppb, room temperature (~ 25 ℃), shaking rate 300 rpm, adsorption time for 24 hours.......... 158

Figure 4-22 Selenium and NO_3^- removal percentage by MGO-EG with different initial NO_3^- concentrations. Tests were done at: MGO-EG dosage 1 g L^{-1}, under neutral pH (~ 6), initial selenium concentration 300 ppb, room temperature (~ 25 ℃), shaking rate 300 rpm, adsorption time for 24 hours.......... 159

Figure 4-23 Selenium and SO_4^{2-} removal percentage by MGO-EG with different initial SO_4^{2-} concentrations. Tests were done at: MGO-EG dosage 1 g L^{-1}, under neutral pH (~ 6), initial selenium concentration 300 ppb, room temperature (~ 25 ℃), shaking rate 300 rpm, adsorption time for 24 hours.......... 160

Figure 4-24 Selenium and PO_4^{3-} removal percentage by MGO-EG with different initial PO_4^{3-} concentrations. Tests were done at: MGO-EG dosage 1 g L^{-1}, under neutral pH (~ 6), initial selenium concentration 300 ppb, room temperature (~ 25 ℃), shaking rate 300 rpm, adsorption time for 24 hours.......... 161

Figure 4-25 Removal percentages of (a) selenite and (b) selenate in the presence of various interfering ions at different pH. Tests were done at: MGO-EG dosage 1 g L^{-1}, initial selenium concentration 300 ppb, initial interfering ions concentration 20 ppm, room temperature (~ 25 ℃), shaking rate 300 rpm, adsorption time for 24 hours. 162

Figure 4-26 Selenium and Ca^{2+} removal percentage by MGO-EG with different pH. Tests were done at: MGO-EG dosage 1 g L^{-1}, initial selenium concentration 300 ppb, room temperature (~ 25 ℃), shaking rate 300 rpm, adsorption time for 24 hours. 163

Figure 4-27 Selenium and Mg^{2+} removal percentage by MGO-EG with different pH. Tests were done at: MGO-EG dosage 1 g L^{-1}, initial selenium concentration 300 ppb, room temperature (~ 25 ℃), shaking rate 300 rpm, adsorption time for 24 hours. 164

Figure 4-28 Selenium and NO_3^- removal percentage by MGO-EG with different pH. Tests were done at: MGO-EG dosage 1 g L^{-1}, initial selenium concentration 300 ppb, room temperature (~ 25 ℃), shaking rate 300 rpm, adsorption time for 24 hours. 164

Figure 4-29 Selenium and SO_4^{2-} removal percentage by MGO-EG with different pH. Tests were done at: MGO-EG dosage 1 g L^{-1}, initial selenium concentration 300 ppb, room temperature (~ 25 ℃), shaking rate 300 rpm, adsorption time for 24 hours. 165

Figure 4-30 Selenium and PO_4^{3-} removal percentage by MGO-EG with different pH. Tests were done at: MGO-EG dosage 1 g L^{-1}, initial selenium concentration

300 ppb, room temperature (~ 25 ℃), shaking rate 300 rpm, adsorption time for 24 hours. 166

Figure 5-1 The wave vector of a photoelectron. 178

LIST OF NOMENCLATURE AND ABBREVIATIONS

AA	Activated Alumina
AC	Activated Carbon
AFM	Atomic Force Microscope
BAT	Best Available Technology
DL	Double Layer
EPA	Environmental Protection Agent
FTIR	Fourier Transform Infrared
GO	Graphene Oxide
IC	Ion Chromatography
ICP-MS	Inductively Coupled Plasma Mass Spectrometry
IX	Ion Exchange
MAC	Maximum Acceptable Concentration
MCT	Magnetic Carrier Technology
MGO	Magnetic particle-Graphene Oxide composites
MGO-EG	Ethylene Glycol Reduced Magnetic particle-Graphene Oxide composites
NMP	1-methyl-2-pyrrolidone
RO	Reverse Osmosis
SEM	Scanning Electron Microscope
SX	Solvent Extraction
TDS	Total Dissolved Solids

TEM	Transmission Electron Microscope
TGA	Thermogravimetric Analysis
WHO	World Health Organization
XPS	X-ray Photoelectron Spectroscopy
XRD	X-Ray Diffraction
ZVI	Zero-Valent Iron

LIST OF SYMBOLS

F	Force in Hook’s law
k	Stiffness of the lever in Hook’s law
z	Distance that the lever is bent in Hook’s law
λ	Wavelength of X-ray Cu Kα (0.154 nm) in Bragg’s equation and Sherrer’s Equation
d	Interlayer spacing in Bragg’s equation
θ	Diffraction angle in Bragg’s equation
KE	Electron Kinetic Energy
BE	Electron Binding Energy
φ_{spec}	Spectrometer Work Function
D	Crystallite size in Sherrer’s Equation
β	Full width at half maximum (radian) of the diffraction peak in Sherrer’s Equation
Q	Adsorption capacity (mg g^{-1})
q	Removal percentage (%)
C_0	Initial Se (IV) or Se (VI) concentration (ppm) in adsorption equation
C	Equilibrium concentration of Se (IV) or Se (VI) (ppm) in adsorption equation
W	Weight of adsorbent (g)
V	Total solution volume (mL)

K	Freundlich constant in Freundlich adsorption model
n	Freundlich constant in Freundlich adsorption model
a	Langmuir constant in Langmuir adsorption model, indicate the saturate adsorption capacity (mg g^{-1})
b	Langmuir constant in Langmuir adsorption model, related to adsorption free energy (L mg^{-1})

Chapter 1 Introduction

1.1 Background of Selenium Pollution and Toxicity in the Environment

Selenium is an essential nutrient metalloid element for life in trace amount, but extremely toxic in excess.[1] Selenium has the narrowest ranges between dietary deficiency (< 40 μg day^{-1}) and toxic levels (> 400 μg day^{-1}).[2] One of the isotopes, ^{79}Se is a long-lived radionuclide (half-life: 6.5×10^4 years), which could be released from nuclear fuel waste depositories through underground water and cause cumulative radioactivity within biosphere.[3]

Selenium is derived from both natural and man-made sources: selenium is found in all natural materials on Earth including rocks, soils, waters, air, and plant and animal tissues; selenium compounds can be released to the environment during the combustion of coal and petroleum fuels, mining and extraction processes of coal and metals (e.g. copper, lead, zinc, uranium).

At the global scale, selenium is constantly recycled in the environment via the atmosphere, marine, and terrestrial systems (Figure 1-1). It has been estimated that 76,000 – 88,000 tons per year of selenium[4] are released globally from anthropogenic activity, which is the major source of selenium release in the cycle, compared to natural releases of 4,500 tons per year (Table 1-1). **[4, 5]** The selenium flus then released to soil and water and later can be transferred to plants, animal organisms and life cycles, resulting in serious health and environmental issues.

Cycle	Selenium flux (tones year^{-1})
Anthropogenic	76,000 - 88,000
Marine	38,250
Terrestrial	15,380
Atmospheric	15,300

Table 1-1 Global selenium fluxes.

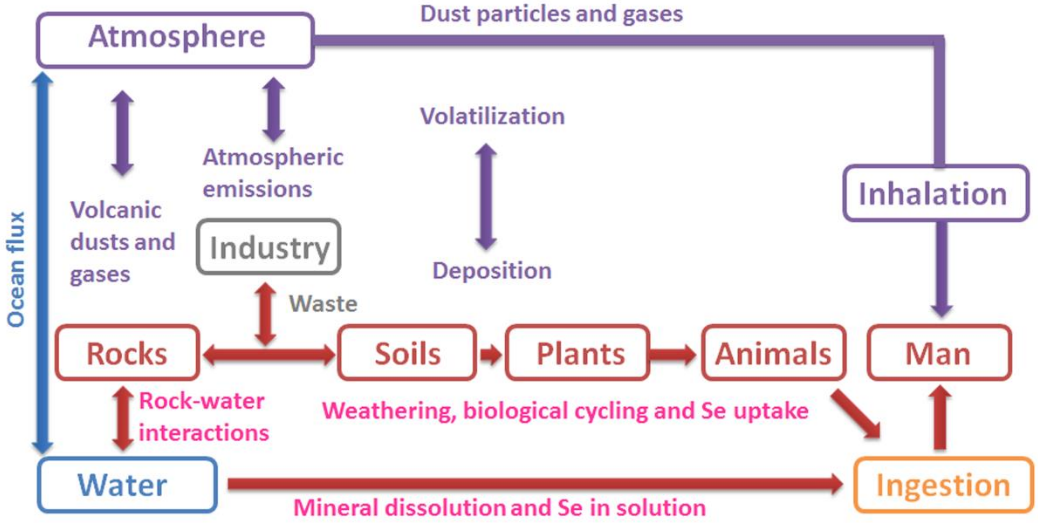

Figure 1-1 Simplified schematic diagram (adapted from literature**[4]**) of the cycling of selenium from the environment to man. The main geochemistry and health pathways are shown in red/thicker arrows.

Plants can suffer selenium toxicity via the following processes[6-8] : Selenium competes with essential metabolites for sites in the plant biochemical structure; Selenium may replace essential ions, mainly the major cations (for example, iron, manganese, copper, and zinc); Selenate can occupy the sites for essential groups such as phosphate and nitrate; Selenium can be incorporated into analogues of essential sulfur compounds in plant tissues.

The short term health effect that selenium potentially causes to human includes: hair and fingernail changes, damage to the peripheral nervous system, and fatigue and irritability; while in long term, selenium can cause hair and fingernail loss, damage to kidney and liver tissue as well as the nervous and circulatory systems.[9]

Hence, it is crucial to characterize selenium distribution in the environment and carefully control selenium intakes by human, plants, and other animals from aqueous environment, soils and atmosphere. This work focuses on the removal of excess selenium from aqueous media, mainly caused by anthropogenic processes, to aid the amelioration of health problems associated with selenium toxicity.

1.2 Water Chemistry of Selenium Oxyanions in Aqueous System

It is estimated that the annual global flux of selenium from land to the oceans is 14,000 tons per year via surface and ground water, which represent a major pathway of selenium loss from land in the selenium cycle.[4]

Selenium is a metalloid element that is located just below sulfur in the periodic table. It resembles sulfur and forms many of the same compounds. The solubility of selenium is similar to sulfur salts. Also, most selenate salts are more soluble than selenite salts.

Selenium exists in the environment with chemical forms of: selenide (Se^{2-}), amorphous or polymeric elemental selenium (Se^0), selenite (SeO_3^{2-}), selenate (SeO_4^{2-}), and organic Se (Table 1-2).

Oxidative state	Chemical forms
Se^{2-}	Selenide (Se^{2-}, HSe^-, H_2Se_{aq})
Se^0	Element selenium (Se^0)
Se^{4+}	Selenite (SeO_3^{2-}, $HSeO_3^-$, $H_2SeO_{3\ aq}$)
Se^{6+}	Selenate (SeO_4^{2-}, $HSeO_4^{2-}$, $H_2SeO_{4\ aq}$)
Organic Se	Selenomethionine, selenocysteine

Table 1-2 Chemical states of selenium in the environment.

While several species of selenium are stable, in aqueous environments, it is most often found as the oxygenated anions of selenite and selenate. This is illustrated in Eh-pH diagram,[10] which shows that selenite is present as the single charged anion, $HSeO_3^-$, below pH 7, but as the double charged anion, SeO_3^{2-}, above pH 7. In contrast, the more oxidized selenate carries a double charge whenever the pH is higher than above 2. The result of this complexity is that both the speciation and the pH of the water must be taken into account when attempting to remediate the selenium. This was demonstrated in early studies focusing on coagulation filtration and lime softening, which concluded that neither approach was effective for complete selenium removal, but that they could be optimized with controlling pH. [11]

The term bioavailability describes the mobility and uptake of selenium into plants and animals. The bioavailability order of different forms of selenium is: selenate (Se^{6+}) > selenomethionine > selenocysteine > selenite (Se^{4+}) > selenium (Se^{0}) > selenide (Se^{2-}).[7]

Under most natural redox conditions, selenite and selenate are the predominant inorganic phases in aqueous solutions. Selenium combines with oxygen to form several other selenium compounds as well. In oxygenated environments, selenium is typically present in the selenate form, while selenite is predominant in reducing conditions. Selenate is more water soluble, more mobile, more bioavailable and less well adsorbed on solid substrates than selenite, thus making selenate a major harmful selenium species in aqueous system.

Selenium forms a very minor component in natural water and rarely exceeds 10 ppb (10 $\mu g\ L^{-1}$) in concentration.[4] A garlic odor has been noted in waters containing 10 - 25 ppb selenium, whereas waters containing 100 - 200 ppb selenium have an acerbic taste.[2, 7] The World Health Organization (WHO) currently set 40 ppb (40 $\mu g\ L^{-1}$) selenium as the Maximum Acceptable Concentration (MAC) for drinking water.[2]

As described above, it is clear that selenium is present in various quantities in the environment as a result of natural and man-made processes. Selenate is the major water-borne selenium species and is difficult to be removed. Therefore, there is an urgent need to develop an efficient method for the removal of the water-borne selenium with high removal capacity.

1.3 Selenium Management Methods and Technologies

Different solution treatment technologies potentially applicable to remove selenium include: precipitation, ion exchange (IX), solvent extraction (SX), reverse osmosis (RO), emulsion liquid membrane, nanofiltration, reduction/ oxidation, lime softening and adsorption. Only some of these technologies reasonably meet the requirements for selenium removal efficiency. The processes described in this section are promising technologies to meet the requirements for selenium removal in water treatment applications.

1.3.1 Precipitation

Precipitation is a commonly used technology to remove ions from aqueous media. By controlling the pH and adding precipitation reagents (sulphors, carbonates, phosphates), coagulation-flocculation agents (iron chloride, aluminum hydroxide) and polymer feeding into the raw water, ions could be separated by sedimentation or filtration and then be collected during the clarification or filtration stage.[12]

The precipitation method has been extended to industry applications due to its simplification, versatility and low cost.[13] However, problems associated with precipitation method include: solid-liquid separation, disposal of large amount of high water content sludge, and secondary contamination due to inappropriate disposal of the unstable precipitates that leach out ions.[14]

1.3.1.1 Precipitation with Ferric-chloride

Ferric-chloride is the commonly used iron salt for selenium precipitation, with an effective pH range of 5 - 8.[12] It works well for selenite, but ineffective for selenate. Therefore, pre-reduction of selenate is required. The precipitation of elemental selenium has not been reported yet.

The chemical reaction for selenite precipitation with ferric-chloride is as follows:[12, 14] (the ferric-chloride does not adsorb selenate, unless it is reduced to selenite)

$$Fe^{3+} + 3\ H_2O \rightarrow Fe(OH)_3\ (solid) + 3\ H^+ \qquad (1)$$

$$SeO_4^{2-} + Fe(OH)_3\ (solid) + 4\ H_2O \rightarrow Fe(OH)_3\text{-}SeO_4^{2-} + 8\ H^+ \qquad (2)$$

The presence of other aqueous species in the solution to be treated may influence the removal of selenite, i.e., the order of adsorption (at pH 7) has been shown to be phosphate > silicate = arsenic (V) ≥ bicarbonate/carbonate ≥ citrate = selenite ≥ molybdate ≥ oxalate > fluoride = selenate ≥ sulfate.[14, 15]

1.3.1.2 Precipitation with Ferrous Hydroxides

The iron ions in previous discussion could also be provided in the in situ form of ferrous hydroxides. Briefly, the precipitation with ferrous hydroxides under alkaline conditions and produce magnetic iron oxide and sodium hydroxide.[16] During this process, ferrous hydroxides reduce selenite and selenate to elemental selenium. These elemental selenium particles remain within iron oxide and can be separate by magnetic separation or adding a strong acid thereto.[16]

The reduction reaction for selenate in the presence of excess ferrous hydroxides to produce magnetite is:[16]

$$Na_2SeO_4 + 9\ Fe(OH)_2 \rightarrow Se^0 + 3\ Fe_3O_4 + 2\ NaOH + 8\ H_2O \qquad (3)$$

The reduction reaction for selenate in the presence of excess ferrous hydroxides to produce maghemite is:[16]

$$Na_2SeO_4 + 6\ Fe(OH)_2 \rightarrow Se^0 + 3\ Fe_2O_3 + 2\ NaOH + 5\ H_2O \qquad (4)$$

The reduction reaction for selenite in the presence of excess ferrous hydroxides to produce magnetite is:[16]

$$Na_2SeO_3 + 6\ Fe(OH)_2 \rightarrow Se^0 + 2\ Fe_3O_4 + 2\ NaOH + 5\ H_2O \qquad (5)$$

The reduction reaction for selenite in the presence of excess ferrous hydroxides to produce maghemite is:[16]

$$Na_2SeO_3 + 4\ Fe(OH)_2 \rightarrow Se^0 + 2\ Fe_2O_3 + 2\ NaOH + 3\ H_2O \qquad (6)$$

These reactions rates reach a maximum criticality at the pH about 9, and drop sharply at pH greater than 10 or less than 8.[16] This is the reason why the reaction will tend to be reversed at high pH, as indicated from the reaction mechanism; while at low pH, the ferrous hydroxides will be dissolved and cannot effectively precipitate.

Parida et al[17] conducted selenite adsorption with different ferrous hydroxides and concluded that the adsorption capacity followed the order of β-FeOOH < α-FeOOH < γ-FeOOH < δ-FeOOH < amorphous ferrihydrite, which was more or less the similar trends of surface area, surface hydroxyl functional group, and total exchange capacity.

Amorphous ferrous hydroxides precipitation has been extensively investigated[13, 17, 18] and has been identified by the US-EPA as one of the best available technology for selenium removal in mining wastes.[9]

1.3.1.3 Lime Softening

Lime softening is also known as Clark's process that utilizes the addition of limewater (calcium hydroxide) to remove ions by precipitation.[19] It is normally applied to reduce the hardness of water (the hardness of is the sum of all multivalent ions, which in typical water treatment applications are mainly the sum of calcium and magnesium) and sometimes to enhance clarification prior to filtration.[20]

The Best Available Technology (BAT) for treating selenium bearing drinking and groundwaters are listed by EPA[9] to include ferric coagulation-filtration (removals = 40 – 80 % for selenite; < 40 % for selenate) and lime softening (removals = 40 – 80 % for selenite; < 40 % for selenate). Briefly, the advantages of lime softening include the fact that it is an effective and reliable treatment process with little pretreatment procedures.

However, the application of these lime softening unit operations for selenium removal from mine water has not been made. The other limitations for lime softening include the high volume of selenium residuals that is discharged into the environment; the fact that filtration is usually required as the after-treatment; high sulfate content water may be significantly interfered with the selenium removal efficiency; and the potential safety issues that cause by operators that dealing with large volume of chemical handlings.[21-23]

1.3.2 Ion Exchange (IX)

Ion Exchange (IX) is widely used for treatment of drinking waters and ground waters for metals, arsenics and selenium removal. Selenium removal is accomplished by using a strong base anion ion exchange resin. Selenate is extracted much more effective than selenite. The extraction of selenate is a function of sulfate concentration. The order of ion exchange selectivity for the strong base resins is roughly as follows:

$HCrO_4^- > CrO_4^- > ClO_4^- > SeO_4^{2-} > SO_4^{2-} > NO_3^- > Br^- > (HPO_4^{2-}, HAsO_4^{2-}, SeO_3^{2-}, CO_3^{2-}) > CN^- > NO_2^- > Cl^- > (H_2PO_4^-, H_2AsO_4, HCO_3^-) > OH^- > CH_3COO^- > F^-$.[12]

There are several drawbacks to the use of ion exchange in this application. Selenium, when present in the form of selenate, is in many ways very similar to sulfate, in fact they are most often found together, and as such are fairly easily removed with a strong base anion exchange resin. The similarities however create another issue. The levels of sulfate are often several factors of a thousand times higher than the selenate concentration. Ion exchange is based on selectivity, removing more selective ions first and less selective later. Because the sulfate and selenium are removed congruently to reach low ppb levels of selenium the ion exchange unit needs remove all of the sulfate as well as the selenium. Since sulfate is a competing component, ion exchange is typically only useful if employed on waters of low TDS and low sulfate concentration. Tailored resins show good selectivity for selenium in the presence of sulfate but only laboratory studies have been performed. Further laboratory studies (on mine water) are recommended.[24]

Another problem for ion exchange is that the ion exchange process will be terminated when the resin reaches the saturation exchange capacity. The regeneration process will consume a large amount of chemicals and convert the resin back to its initial composition incompletely. Therefore, resin fouling and scaling is another potential problem. The discharged resin contains the removed pollutants, making it hazardous waste. Considering the sulfate interfering effect mentioned above, this significantly increases the cost to regenerate the resin bed. This additional cost often makes ion exchange uneconomical for selenium removal in high salt streams.[15, 24]

Unless there is an on-site opportunity to co-treat this waste stream with other wastewaters, such as in an evaporator or membrane separation system or chemical precipitation, disposal of the regenerant may be problematic and expensive.[25]

1.3.3 Solvent extraction (SX)

Solvent Extraction (SX) is a method for separating a substance from others components by using a solvent and chelating reagent. It relies on variations in the solubility of different compounds in different substances. [15] In most cases, the substance to be extracted, which may be a solid, a liquid or a gas, is dissolved in a liquid, along with other substances, and a liquid solvent is used for the extraction — this is sometimes called liquid-liquid extraction.[26, 27]

Solvent extraction has been investigated to extract selenium and determine selenium concentration at ppm level with the chelating agent/solvent system of diethylammonium N,N-diethyldithiocarbamate (DDTC or DDDC)/chloroform,[28] ammonium pyrrolidinedithiocarbamate (APDC)/chloroform[29]. In case of APDC/chloroform system, for example, the selenium extraction ration could reach ~ 100 % from pH ~ 2 to pH ~ 5, and drop dramatically starting from pH 5. At pH ~ 6.5, the extraction ratio is only ~ 5 %. The results were encouraging but further test work should be conducted on the feasibility, cost evaluation and organic solvent after treatment problem of this method.

1.3.4 Reverse Osmosis (RO)

Reverse Osmosis (RO) is a membrane-technology filtration method that is extensively used for removing inorganic contaminants from drinking and groundwater by applying pressure to the solution when it is on one side of a selective membrane. The result is that the solute is retained on the pressurized side of the membrane and the pure solvent/water is allowed to pass to the other side. To be "selective", this membrane should not allow large molecules or ions through the pores but should allow smaller components of the solution (such as the solvent or water) to pass freely.[30]

RO has been applied to the treatment of multicomponent electrolyte solutions, which is pretreated agriculture drainage water containing small amount of nitrate and selenate, and large amount of sulfate, chloride, magnesium, and sodium ions.[31] The RO membrane shows efficient (> 99.94 %) removal for selenate and concludes that the potential membrane performance affecting parameters include the feed pressure, feed solution composition and concentration, concentration polarization, membrane compaction, and the density of charged chemical groups.[31]

Although the selenium removal efficiency seems promising, RO has its own restrictions, such as the fact that RO may require extensive pretreatment of mine water to remove solids and to lower the concentration of total dissolved solids (TDS). Otherwise extensive membrane fouling may occur. It is doubtful that RO will ever be applied to mine water.[14, 15, 24]

1.3.5 Nanofiltration

Nanofiltration is a relatively new membrane filtration process, which is driven by pressure and target for small sized particles and ions. It has two main features: the removal capacity for different organic components in aqueous solutions; and the removal capacity for low molecular weight ions (anions) of different valences.[32] Nanofiltration applications have be commercially arranged in mainly two groups: partial water desalination (such as the removal of high TDS) and separation of salts with monovalent anions from organics (such as sulfate removal from seawater, sulfate removal from concentrated brines, organic compound removal from paper plant effluents and for organic compound removal from ground water).[33]

In selenium removal, nanofiltration appears to be a technology for treating some low metal containing selenium bearing mine water. In previous report, nanofiltration has never been applied to mine water but has been successfully applied (on a laboratory scale) to agricultural waters from San Joaquin Valley drainage (pH 6.3 - 8.5), which is containing 24 - 308 ppb selenate, 2,080 - 26,100 ppb sulfate, and 780 - 38,800 ppb TDS. As the result, > 95 % removal of selenium removal percentage and other multivalent anions can be achieved for contamination waters.[34]

The technology is similar in concept to reverse osmosis (RO), which is going to be discussed later. The nanofiltration system is operated at pressure that are about one-third of that required for reverse osmosis, which is a significant energy saving. [14, 15, 24] Moreover, less pretreatment is required for nanofiltration, thus plant installations with nanofiltration membranes could be much smaller and significantly less expensive than the large demonstration plant built. The use of organic additives to prevent membrane fouling by metal compound precipitation may allow this technology to be applied to mine water. [34]

Nanofiltration technology shows a good potential for application to mine water but requires further test work to answer questions concerning the presence of multiple anionic species, presence of suspended solids, high total dissolved solids, and the stability of the membranes in acidic multicomponent solutions.

1.3.6 Emulsion Liquid Membranes

Emulsion liquid membranes method is developed from the traditional solvent extraction method. Basically, emulsion liquid membranes are prepared by dispersing a primary emulsion (normally the water-in-oil type) in a second aqueous phase. The organic emulsion phase separates the two aqueous phases and acts as a liquid membrane. The emulsion liquid membrane basically consists of a low viscosity diluent, a surfactant to stabilize the primary emulsion and sometimes an extractant. The emulsified aqueous phase is usually the receiving phase and the continuous aqueous phase the feed phase. [35, 36]

The emulsion liquid membranes method is able to achieve a much higher concentration of metals with a simple process of only few steps, while maintaining the high selectivity of solvent extraction. Another advantage of applying this emulsion liquid membranes technique is that it can be used to treat the dilute solutions as well. This may be a promising solution for treating industrial wastewater, which contains valuable metals in low concentrations. Traditional solvent extraction has been applied for treating wastewater but the extraction rate is very slow and a large amount of extractant along with large interfacial area is required to bring down the contaminants to the acceptable level. With environmental protection laws becoming more and more stringent and also with the depletion of natural sources, recovery of these valuable metals is of prime importance.[37]

Pilot studies have shown that selenate is extracted rapidly even in the presence of sulfate at pH values > 2. Selenite extraction is influenced by the presence of sulfate, i.e., the rate of extraction is decreased with increasing sulfate. Sulfate is extracted in preference to selenite unless the pH is > 9.5. Extraction of selenite in the presence of up to 1000 ppb sulfate at pH 9.5 was very effective (extraction to ~ 10 ppb in 20 minutes; to 1 - 2 ppb in 30 minutes.) [15]

This technology shows a good potential for application to mine water but requires further test work to answer questions concerning the presence of multiple anionic species, presence of suspended solids, the presence of high total dissolved solids, and the stability of the emulsion in acidic, multicomponent solutions.

1.3.7 Oxidation

Oxidation of selenite to selenate is important for some of the subsequent removal technologies (such as ion exchange and biological treatment).[12] Effective oxidation has been demonstrated but the oxidizing reagents are expensive. Effects to find low cost treatment technologies and lower cost oxidizing reagents (for use at ambient temperatures) needs to be continued.[15] However, since relatively low oxidation state selenium (such as selenite, elemental selenium and selenide) is easier to be removed in most of the cases, such as adsorption and precipitation, oxidation method is rarely used. On the contrary, the previously discussed reduction method is more feasible.

1.3.8 Reduction Process

Reduction of selenate to selenite (for adsorption technologies) or to elemental selenium (for precipitation) or to selenide (for metal selenide compound formation) as a pretreatment method is important for some of the subsequent removal technologies. Conditions for successful reduction are known and are well characterized in the literature. Ferrous hydroxide,[13, 16-18] zero-valent iron (ZVI),[15, 38-40] bacteria,[41-44] ferrous sulfate,[41] zinc,[45] sulfur dioxide,[46] and hydrazine[47] have been used as reductants. The first three reductants are going to be discussed in details as the most effective methods.

1.3.8.1 Reduction with Ferrous Hydroxide

As discussed in precipitation method, reduction process with ferrous hydroxide has been developed for treating selenium surface and agricultural waters.[13, 16-18]

Briefly, the precipitation with ferrous hydroxides under alkaline conditions and produce magnetic iron oxide and sodium hydroxide.[16] During this process, ferrous hydroxides reduce selenite and selenate to elemental selenium and produce magnetite or maghemite. These elemental selenium particles remain within iron oxide and can be separate by magnetic separation or adding a strong acid thereto.[16]

The reduction reaction with ferrous hydroxides for selenite is:[16]

$$Na_2SeO_3 + Fe(OH)_2 \rightarrow Se^0 + Fe_2O_3 \text{ (or } Fe_3O_4) + NaOH + H_2O \qquad (7)$$

The reduction reaction with ferrous hydroxides for selenate is:[16]

$$Na_2SeO_4 + Fe(OH)_2 \rightarrow Se^0 + Fe_2O_3 \text{ (or } Fe_3O_4\text{)} + NaOH + H_2O \qquad (8)$$

These reactions rates reach a maximum criticality at the pH about 9, and drop sharply at pH greater than 10 or less than 8.[16] It is possibly because at high pH, the reaction will tend to be reversed, as indicated from the reaction mechanism; while at low pH, the ferrous hydroxides will be dissolved and can not effectively precipitate. It is also conducted from previous study[17] that selenite adsorption with different ferrous hydroxides and concluded that the adsorption capacity followed the order of β-FeOOH < α-FeOOH < γ-FeOOH < δ-FeOOH < amorphous ferrihydrite, which was more or less the similar trends of surface area, surface hydroxyl functional group, and total exchange capacity.

Amorphous ferrous hydroxides precipitation has been extensively investigated[13, 17, 18] and has been identified by the US-EPA as one of the best available technology for selenium removal in mining wastes.[9]

However, the generation of relatively large volumes of iron sludge and the relatively high cost of reagents makes its application to mine water questionable. Also, the product could not be stored outdoors without potential re-release of selenium. This technology does not appear to be applicable (at a reasonable cost) to mine water.[15]

1.3.8.2 Reduction with Zero-Valent Iron (ZVI)

Zero-valent iron (ZVI) was reported to successfully applied for selenate removal in the presence of various concentrations of Cl^-, SO_4^{2-}, NO_3^-, HCO_3^-, and PO_3^{4-}.[38] The results indicate that under the adsorption time of 16h, ~ 100 % selenate can be removed from the Cl^- solution, while 56 % selenate can be removed from the SO_4^{2-} solution under a closed containing system. The results also show the interfering effects with the presence of SO_4^{2-}, HCO_3^-, and PO_3^{4-}. Two possible mechanisms are proposed: one is that zero-valent iron reduce selenate to selenite, followed by the rapid adsorption of selenite on the ferrous hydroxide, which is the oxidation production of zero-valent iron; the other one is that selenate directly adsorb on the corrosion ferrous hydroxide and produce selenite.

Zero-valent iron is also reported as a reductant is based on the reduction of selenium in the presence of copper ions.[15] The elemental iron reduces both selenium and copper to produce a copper selenide on the iron surface. Further test work is required to determine what the final achievable copper content would be in the application pH range. This technology shows promise for application to mine water.

Zero-valent iron can be applied with selenate reducing bacteria[39] or redox mediator[40] and significantly enhance the selenium removal percentage.

In the study of Zhang et al.,[39] a selenate-reducing bacterium, Citrobacter braakii, was applied to reduce selenate from natural river and drainage waters. During an 8-day experiment, 87-97% of the added selenate in New River water and White River water, California, was reduced to elemental selenium or transformed to organic selenium. It is also concluded that addition of zero-valent iron (ZVI) into these waters along with C. braakii inoculation significantly enhanced the removal (up to ~ 100 %) of selenate and reduced the formation of organic selenium.

It is also assessed in report from Zhang et al.[40] that the zero-valent iron and a redox mediator (anthraquinone-2, 6-disulfonate (AQDS)) for the ability to enhance the removal of selenate and selenite in synthetic drainage water by Enterobacter taylorae, a reducing bacteria. The results showed that selenate was almost entirely reduced to elemental selenium and transformed to organic selenium in the drainage water during a 7-day experiment with a high selenium removal percentage of 94.5 – 96.5 %.

1.3.8.3 Biological Reduction

Bacterial reduction of selenium aqueous species to elemental selenium has been shown a potential candidate for treating mine water. The bacteria that appears promising is P. Stutzeri which can reduce both selenite and selenate species. A P. Stutzeri isolate that was acclimated to mining process waters was capable of removing 33 ppm selenate from the water containing 285 ppm sulfate in a bioreactor in a residence time as short as six hours.[15]

Test work was conducted on mine water using two different bioprocessing approaches. Pseudomonas bacteria were grown on carbon surfaces by pretreating the surfaces with nutrients and biopolymers, i.e., a biofilm was formed on the carbon surfaces. A second approach was to extract enzymes from the Pseudomonas bacteria which was then coated onto carbon surfaces or impregnated in gel beads. A mine water containing 620 ppb selenate was treated in a single-stage aerobic bioreactor (at ambient temperature) for a residence time of 18 hours. The live biofilms produced effluent waters containing < 10 ppb selenium for about nine months without breakthrough. The enzyme preparations also produced effluents containing < 10 ppb selenium with breakthrough occurring after four months of continuous operation.

Further test work was conducted to investigate the possibility of simultaneously removing cyanide (by oxidation) and selenium (by reduction to elemental selenium) from mining process solutions. Live microbes could not be used because of the toxicity of cyanide toward the bacteria. Therefore, enzymes extracted from cyanide oxidizing bacteria and from selenium reducing bacteria were immobilized in gel beads. The results showed that simultaneous destruction of cyanide (initial concentration: 102 ppm) and reduction of selenium (initial concentration: 31.1 ppm) could be successfully accomplished.

The above described bioprocessing technologies were also successful in removing nitrate from mine water from 53 ppm to < 0.1 ppm at a rate of > 3.3 ppm/hour.[15]

In summary, biologic reduction is effective, especially with the further enhancement of zero-valent iron. However, the whole treatment process takes a very long time, which limits its application in a degree.

1.3.9 Biological Treatment

Apart from the biological reduction method mentioned above, biofilm reactors have been demonstrated to be an effective and economical means for treating selenium as well as other metals and pollutants in wastewaters.[48]

Bioreactors for this application are typically anaerobic processes that are designed using specialized microbes and are controlled by the metered addition of nutrients to sustain the biomass. The biofilm is formed on a substrate within the reactor vessels where a stable biomass is then established. The nutrient supplements added to the process consist of organics like ethanol, acetic acid or biosolids.[49]

Due to the variables nature of feed waters, site specific selections of microbes, nutrient cocktail supplements and biomass arrangements are required to optimize a treatment system.

Since the microbes are typically selected to target specific pollutants, the treatment systems usually consist of two or more reactors per targeted pollutant. A wastewater containing selenium may, therefore, consist of a reactor train for selenium, with the train containing two or more vessels. All trains and vessels would be arranged in series.[50]

Biofilm reactors have been demonstrated to be effective for removing selenium to below detection limits on a consistent basis using pollutant targeted and controlled systems. The reactor is able to remove selenium in the respective, common oxidation states.[14]

1.3.10 Adsorption

Adsorption is now recognized as an effective and economic method for waste water treatment. The adsorption process offers flexibility in design and operation and in many cases will produce high-quality treated effluent. In addition, because adsorption is sometimes reversible, adsorbents can be regenerated by suitable desorption process.[51]

The adsorption process is based on the adsorption of soluble contaminants onto solid adsorbents. Various materials, including fly ash,[52-55] and other surface reactivate adsorbents (such as activated carbon,[56-63] molecular sieves[64, 65] silica gel,[66-68] activated aluminum oxide,[69-71] and meso-porous materials[72-76]) have been widely used in wastewater treatment. Significant progresses have been developed in the past two decades. The adsorption process is capable of removing most contaminant species like heavy metal and organic compound from solution. The commonly used selenium adsorbents are discussed below.

1.3.10.1 Adsorption with Ferric-chloride

Adsorption of selenium ions with ferric-chloride mainly effects through precipitation process, as is discussed in previous section. Briefly, adsorption with ferric-chloride works well for selenite (within the pH range of 5 - 8), but ineffective for selenate.[12]

As discussed in the precipitation section, the chemical reaction for selenite precipitation with ferric-chloride is as follows:[12, 14] (the ferric-chloride does not adsorb selenate, unless it is reduced to selenite)

$$Fe^{3+} + 3H_2O \rightarrow Fe(OH)_3 \text{ (solid)} + 3H^+ \tag{1}$$

$$SeO_4^{2-} + Fe(OH)_3 \text{ (solid)} + 4H_2O \rightarrow Fe(OH)_3\text{-}SeO_4^{2-} + 8H^+ \tag{2}$$

The presence of other aqueous species in the solution to be treated may influence the removal of selenite, i.e., the order of adsorption (at pH 7) has been shown to be phosphate > silicate = arsenic (V) ≥ bicarbonate/carbonate ≥ citrate = selenite ≥ molybdate ≥ oxalate > fluoride = selenate ≥ sulfate.[14, 15]

1.3.10.2 Adsorption with Activated Alumina (AA)

Selenium adsorption with activated alumina (AA) has been evaluated in previous report[77] with the conclusion that the selenite can be adsorbed effectively (nearly complete within pH 3 - 8) on activated alumina while selenate adsorption by alumina is poor. Selenate adsorption drops rapidly with increasing pH and is less than 50 % at pH 7. Sulfate and carbonate adsorption significantly interferes with selenate adsorption but has only a minor influence on selenite adsorption.

The possible adsorption mechanism is also proposed, suggesting that the adsorption of selenium ions can be accomplished in a three step process:

1) Acidification:

$$\text{Alumina-HOH} + HCl \rightarrow \text{Alumina-HCl} + H_2O \tag{9}$$

2) Preferential adsorption:

$$\text{Alumina-HCl} + SeO_4^{2-}/SeO_3^{2-} \rightarrow \text{Alumina-H-}SeO_4^{2-}/SeO_3^{2-} + Cl^- \tag{10}$$

3) Regeneration:

$$\text{Alumina-H-}SeO_4^{2-}/SeO_3^{2-} + 2\ NaOH \rightarrow$$

$$\text{Alumina-NaOH} + Na_2SeO_4^{2-} / Na_2SeO_3^{2-} + H_2O \qquad (11)$$

The regenerated alumina can be acidified and the adsorption process repeated:

$$\text{Alumina-NaOH} + 2\ HCl \rightarrow \text{Alumina-HCl} + NaOH + H_2O \qquad (12)$$

1.3.10.3 Adsorption with Activated Carbon (AC)

Activated carbon adsorption is widely used in the treatment of ground water and drinking water for organic pollution and heavy metal ions adsorption. The relatively high adsorption percentage of activated carbon derives mainly from its large micropore and mesopore volumes and the resulting high surface area. However, it is not very effective (21.3 % for selenite and 30.7 % for selenite) for adsorbing selenium ion in our preliminary experiment (Table 1-3).

1.3.10.4 Challenging with Adsorption Method and Commonly-used Adsorbents

Among all the selenium treatment methods, adsorption method holds the advantages of simple process and economy. However, most of the commercial adsorbents, including activated carbon, silica gel, clay, molecular sieve, ferric oxyhydroxide, and activated aluminum oxide, only have certain adsorption capacity of selenite but show very poor performance in selenate removal.[15] Comparison of selenite/selenate removal percentage between different adsorbents is listed in Table 1-3.

Adsorbent	For Se (IV)	For Se (VI)
Fe_3O_4 (diameter 400 nm)	18.6 %	0
Fe_3O_4 (diameter 10 - 20 nm)	93.03 %	5.18 %
Activated Carbon	21.3 %	30.7 %
Magnetic Activated Carbon	3.4 %	0
Ferric-chloride[14]	Effectively at pH < 8	Not effective
Alumina[77]	Effective at pH 3 - 8	< 50 % at pH 7
Ferric Oxyhydroxide/Peat/Resins[15]	Promising	Not effective

Table 1-3 Comparison between other adsorbents (the uncited data are obtained in this work with initial selenium concentration: 10 ppm).

It is proposed in previous literatures that the strong bonding species such as selenite form an inner-sphere complex with hydroxyl groups on ferric oxy-hydroxides surface, while the weaker bonding specious selenate is normally absorbed through the formation of an outer-sphere complex with one water molecular in between selenate and surface hydroxyl groups. Compared with inner-sphere complex, outer-sphere complex is much unstable.[8, 78-82] Thus, there is an urgent need to develop a novel adsorbent that could favor the water-borne selenium removal.

1.3.11 Summary of Advantages and Disadvantages of Different Selenium Treatment Technologies

The advantages and disadvantages between different selenium treatment methods are listed in Table 1-4.

Technology for Se treatment	Advantages and disadvantages
Precipitation	Effective for selenite within certain pH range, ineffective for selenate, unless reduced to selenate. Problem with residual treatment.
Ion Exchange (IX)	Lab study only. Interfering with sulfate. Resin fouling, scaling, and regeneration problems.
Solvent Extraction (SX)	Lab study only. Problem with organic solvent after treatment.
Reverse Osmosis (RO)	Require extensive pretreatment of mine water and is doubtful to be applied due to the possible extensive membrane fouling.
Emulsion Liquid Membranes	The presence of sulfate influences very much.
Nanofiltration	Operate at pressures, with combination of RO.
Reduction	Incomplete reduction. High cost of reagents.
Biological Reduction	Complicated process. Takes long time.
Oxidation	Oxidizing reagents are expensive. Not feasible.
Adsorption	Fast, require minimal pretreatment. Ineffective for selenate, highly interfered by other ions.

Table 1-4 Selenium treatment methods and their advantages and disadvantages.

The process and operating parameters that were preferential included the following attributes:

- High removal efficiency;
- Low capital and operating costs;
- Minimum residual volume and concentrations of pollutants;
- Process residuals categorized as non-hazadous, non-toxic wastes;
- Simple process;
- Simple operation;
- Simple controls and instrumentation;
- Minimum pre- and post-treatment requirements;
- Low maintenance;
- High reliability.

In most of the cases, several treatment methods are combined to obtain a better selenium removal efficiency. For example, reduction method is frequently combined with the precipitation of adsorption to make the removal of selenate more efficient. However, this combination sacrifices the ideal situation of simple process and operation.

Considering all the parameters, adsorption method holds the advantages of simple process and economy among all the selenium treatment methods. In this thesis, adsorption method has been discussed, since it is more feasible, more effective and economic in selenium removal.

1.4 Graphene/Graphene Oxide (GO) Based Adsorbents

1.4.1 Advantages of Graphene/Graphene Oxide (GO) Based Adsorbents

Following the intensive study of C_{60}[83] and carbon nanotubes,[84] graphene,[85] a novel quasi-two-dimensional carbon material, has attracted greater interest from scientists in various fields for its unique properties. The generalized definition of graphene is graphite with the layer number below ten, while the narrow definition of graphene is graphite monolayer.[85, 86] As illustrated in Figure 1-2, the 2 D graphene can be visualized as a building block for different forms of graphitic materials depicted below. The left figure is the 0 D Bucky ball (also known as fullerenes or C_{60}, molecule of carbon with 60 atoms, arranged similar to a soccer ball), when graphene is wrapped to a rounded form; the center figure is the 1 D carbon nanotubes (CNT, cylindrical wire-like structure with dimensions of a nanometer, can be single wall or multi-walls), when graphene is rolled; the right figure is the 3 D stacked graphene layers, known as graphite when > ten layers.

It possesses a high theoretical specific surface area of 2600 m^2 g^{-1},[87] outstanding thermal conductivity (3000 W $(m\cdot K)^{-1}$), mechanical property (1060 GPa),[88] and distinguished characters such as the prominent electron mobility (15000 cm $(V\cdot s)^{-1}$)[89] at room temperature, perfect quantum-tunnel effect, and the half-integer quantum hall effect.[90-93]

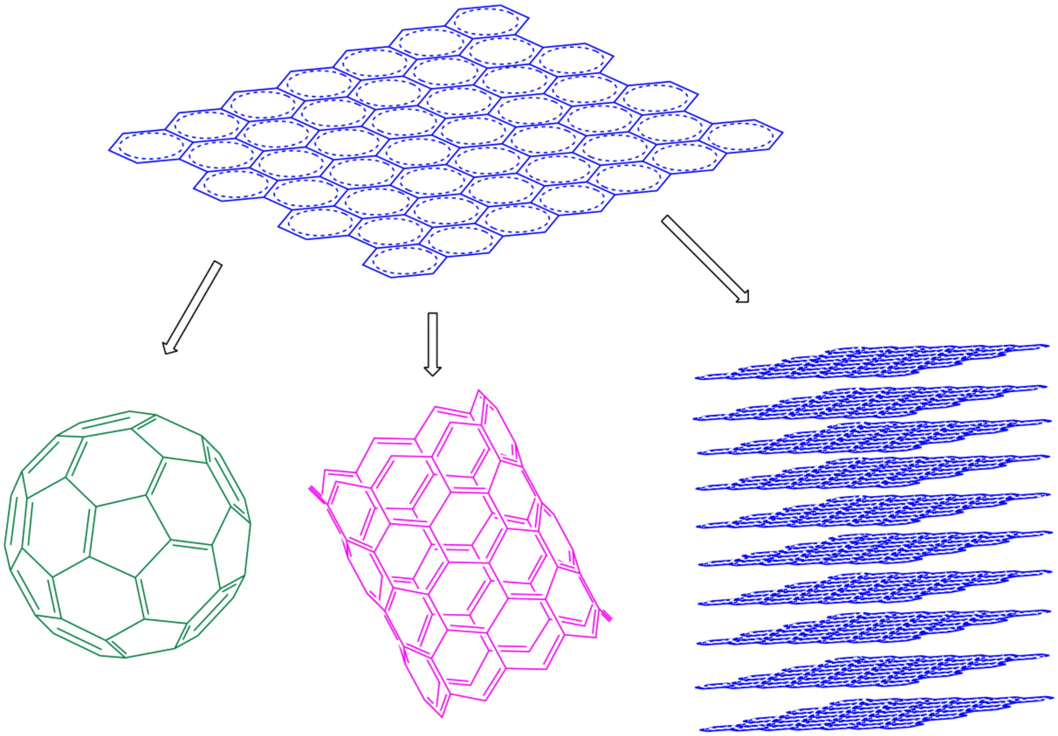

Figure 1-2 Buckyballs (bottom left), carbon nanotubes (bottom center) and ten layers graphite (bottom right) all share the same honeycomb polycyclic molecular structure of graphene (top). Figure adapted from literature.[94]

The chemical process to make graphene is to reduce graphene oxide. This process starts from oxidation of graphite to make graphite oxide. After ultrasonic, graphite oxide could be dispersed to graphene oxide (GO) nano-platelets with only one or few layers. After reduction treatment, graphene oxide could be converted to graphene. During this process, the interesting intermediate graphene oxide attracts a lot of attention. Compared with the hydrophobic nature of graphite, graphene oxide is a better candidate as an adsorbent because graphene oxide has hydrophilic monolayers with a large quantity of surface hydroxyl and carboxyl groups. Graphene oxide (GO)/graphene based adsorbents demonstrate promising removal ability in heavy metal ions,[95] anions,[96] radionuclide,[97] organic contaminations,[98, 99] oil spill-ups,[100] and microbial community[101]. Although there is no study available on the application of GO based adsorbents in selenium removal, GO still can be considered as an adsorbent candidate for selenium oxyanions removal because of its high surface area, mechanical strength, atomic thickness, ability to support subnanometer pores,[102] abundant surface hydroxyl and carboxyl functional groups, and easy modification. Surface hydroxyl groups are crucial for affinity with high valence selenium oxyanions and formation of conjugate acids (i.e., the inner/outer-sphere complex, which is going to be discussed in the following chapters).[103]

1.4.2 Challenges in Graphene/Graphene Oxide (GO) Based Adsorbents

Preliminary selenium adsorption results manifest that GO has certain degree of adsorption ability for both selenite and selenate. However, due to the super hydrophilicity, it is very difficult to separate GO-Se compound from water after adsorption. The difficulty in adsorbent separation cause the residue in selenium containing slurry, making it impossible to reuse the adsorbent.

1.5 Nano Iron Oxide Adsorbent

1.5.1 Magnetic Carrier Technology (MCT)

Magnetic Carrier Technology (MCT) refers to a carrier system using magnetic particles to carry non-magnetic materials (a number of particles or molecular species) on its surface, or entrapped within the carrier particles, to make them separable by magnetic separation.[104, 105] This technology makes the efficient, fast, high capacity and well-developed magnetic separation applicable to non-magnetic materials separation. MCT is now developed to be applied in organic impurities removal, biological cell separation, drug delivery, effluent treatment, mineral separation, and food processing. [105]

The magnetic support materials should fulfill two functions: [104, 105] firstly, they provide highly selective attachment to the target species through appropriate surface properties; secondly, they contain magnetic materials which confer magnetic properties to the ensembles formed with the species to be separated.

Figure 1-3 illustrates the principle of magnetic carrier separation. Magnetic carriers are added to the feed water containing target species (selenium). The magnetic carriers selectively bind to the targeted selenium, and magnetic separation allows the separation of the targets from the treated clean water. Further magnetic carrier stripping and reuse could be realized after the magnetic separation. This method can be used either to recover valuable species, or to remove undesired ones from a stream.

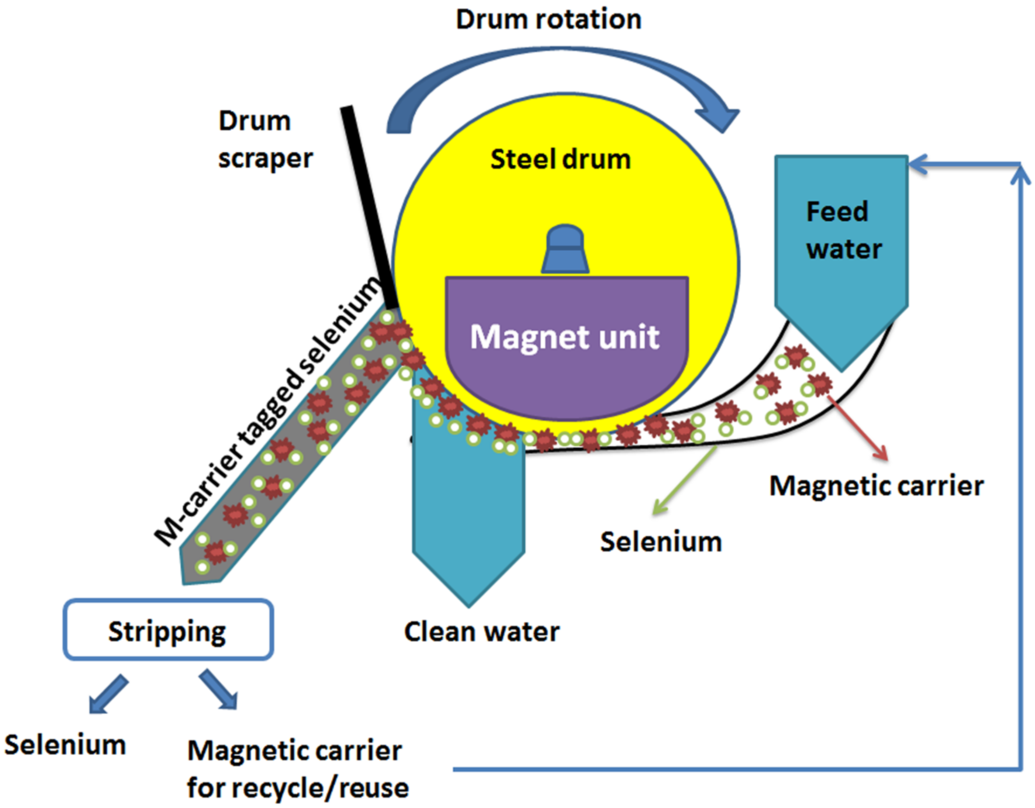

Figure 1-3 Diagram of magnetic separation in water treatment process.

1.5.2 Iron Oxides: Affinity with High Valence Selenium Oxyanions

Iron oxide ores, such as magnetite,[106] goethite,[78] and hematite[107] were reported in selenite removal. The selenium removal abilities for these iron oxides are listed in Table 1-5. When dissolved in water, iron oxide hydrolyses and generate hydroxyl group, which is also the chelating agent in high valence selenium oxyanions adsorption. However, these iron oxides show limited adsorption for selenate.

Type of iron oxides	Selenium oxidation state	Selenium removal ability
Magnetite	Selenite	~ 55% removal at pH ~ 2; removal percentage decrease with pH and reach ~ 0 at pH ~ 12;
	Selenate	~ 12 % removal at pH ~ 2; removal percentage decrease with pH and reach ~ 0 at pH ~ 12;
Goethite	Selenite	~ 100 % removal at pH ~ 2; removal percentage decrease from pH ~ 7 to 0 at pH ~ 12;
	Selenate	~ 40 % at pH ~ 2; removal percentage drop to 0 at pH ~ 7;
Hematite	Selenite	selenite removal percentage ~ 100 % within pH < ~ 10;
	Selenate	not effective for selenate removal.

Table 1-5 Selenium removal ability of different types of iron oxides.

The mechanism for selenium adsorption onto iron oxides has been studied by previous researchers. Hayes et al.[80] conducted in situ Extended X-ray Absorption Fine Structure (EXAFS) measurements on adsorption of selenium at α-FeOOH (goethite)-water interface and indicated that selenite would form a strongly bonded, inner-sphere bidentate complex, while selenate would form a weakly bonded, outer-sphere monodentate hydrated complex. Zhang and Sparks[8] studied kinetics and mechanisms of selenium adsorption at goethite and water interface using pressure-jump (p-jump) relaxation with conductivity detection and concluded that the first step of selenium adsorption mechanism is the formation of outer-sphere complexes through electrostatic attraction, followed by the second step, transformed into inner-sphere complexes. Chao et al.[79] used Triple Layer surface complexation Model (TLM) to provide a quantitative description of selenium adsorption onto amorphous iron oxy-hydroxide and manganese dioxide and assess the importance of surface site heterogeneity on anion adsorption. The original TLM formation [108, 109] contains three planes: surface (or *o*-plane), β-plane, and diffuse layer (or *d*-plane) on the adsorbent surface. Later on, Hayes et al.[81, 110] modified the model and proposed that inner-sphere surface complexes are formed by placing the adsorbing ion in the *o*-plane, while outer-sphere complexes β-plane.

Previous infrared spectroscopy and kinetic studies[111-114] have indicated that strongly binding anions, such as selenite, adsorb on iron oxides by ligand exchange mechanism. An inner-sphere complex is formed from an aqueous ligand exchanging for the hydroxyl group on iron oxides surface (marked as ≡S), involving coulumbic interactions and surface coordination.

For selenite (inner-sphere complex),

$$\equiv S\text{-}OH + SeO_3^{2-} + H^+ \rightarrow \equiv S\text{-}SeO_3^- + H_2O \qquad (13)$$

Compared with selenite, selenate is a weaker binding anion, which could only be adsorbed through electrostatic attraction to iron oxides surface forming an outer-sphere complex with one water molecule between iron oxides surface site and selenate ligand.[80, 114] The outer-sphere is less stable, which makes it harder to form. That is the reason why most adsorbents are ineffective to selenate.

For Se selenate (outer-sphere complex),

$$\equiv\text{S-OH} + \text{SeO}_4^{2-} + \text{H}^+ \rightarrow \equiv\text{S-OH}_2^+\text{-SeO}_4^{2-} \tag{14}$$

In this work, nano-Fe_3O_4 is chosen to be the magnetic carrier because of its excellent magnetic properties and its affinity with selenium oxyanions, which fulfills the two functions mentioned above.

1.6 Design and Scope

This work combines the advantages of graphene oxide with nano iron oxide to make two kinds of Magnetic particle-Graphene Oxide composites (MGOs). The hydrophilic graphene oxide mono layer has large surface area, abundant surface functional groups (mainly hydroxyl, carboxyl, and carbonyl groups) and affinity to high valence selenium oxyanions and formation of conjugate acids. Magnetic nano iron oxide could effectively extend graphene oxide to the magnetic separation process, and strengthen the whole adsorption capacity by its affinity with high valence selenium oxyanions.

Figure 1-4 shows the scheme of MGOs synthesis, application, stripping and reuse. In this thesis, magnetic iron oxide particles were in-situ grown on GO mono sheet to synthesis MGOs with two different methods. The adsorption ability of MGOs are enhanced by the two components GO and magnetic iron oxide. After adding MGOs into the selenium containing slurry, the adsorption process could be completed in a short time (about 10 seconds). MGOs could then be recycled under an external magnetic field and reuse. Furthermore, the combination of iron oxide with large and stable GO nano-sheets could help avoid the problem of high susceptibility to oxidation and agglomeration of small magnetic particles with high surface free energy, when exposed to practical continuous flow systems.[96]

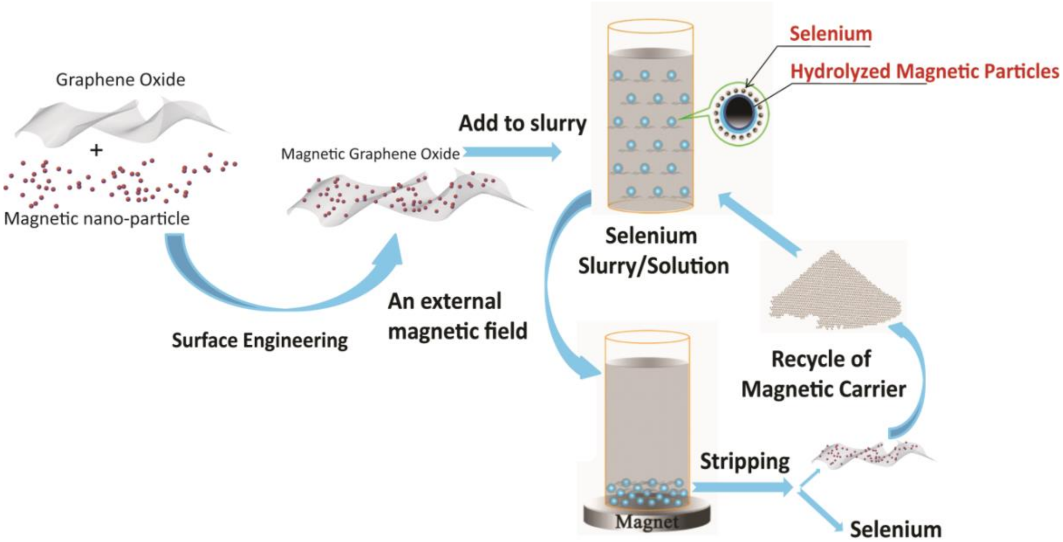

Figure 1-4 Scheme of MGO synthesis, application stripping and reuse.

1.7 Outline of This Thesis

Background of selenium pollution, water chemistry of selenium, selenium management methods, graphene/graphene oxide (GO) and iron oxide based adsorbents are introduced in the first chapter.

Chapter two describes the synthesis details of GO and two kinds of magnetic iron oxide-GO composites: Magnetic particle-Graphene Oxide composites (MGO) and Magnetic particle-Graphene Oxide composites reduced by ethylene glycol (MGO-EG). Selenium adsorption tests and all the characterization methods (principles and application in this work) are also discussed in this chapter.

MGO characterization results and selenium removal with different conditions have been discussed in chapter three. Briefly, MGO achieves > 99.9 % removal of selenite and ~ 80 % removal of selenate under neutral pH (~ 6) only within ten seconds. Acidic condition can increase the selenate removal percentage to ~ 95 % by MGO.

Modification of initial MGO was conducted with different reaction conditions, solutions and reagents. One of the efficient ways so far is to add ethylene glycol (EG) as both the reducing agent and stabilizer. The according characterization and selenium adsorption results of this as-synthesized Magnetic particle-Graphene Oxide composites reduced by ethylene glycol (MGO-EG) have been discussed in chapter four. Basically, with the addition of EG, the magnetic properties and selenium removal ability have been improved. The saturation magnetization increases from 13.47 emu g^{-1} (for MGO) to 49.7 emu g^{-1} (for

MGO-EG). The selenium removal percentage increases to > 99.9 % for selenite and ~ 95 % for selenate under neutral pH (~ 6) only within ten seconds. In acidic condition, the removals of both selenite and selenate are nearly complete (both > 99.9 %).

Chapter five summarizes the main findings and results, indicating MGOs are promising for selenium removal from waste water. Finally, suggested future work is proposed, including the selenium mechanism study, graphene oxide surface property study, interfering ions control, and the potential adsorption for other heavy metal ions with MGOs.

1.8 References

[1] L. Schomburg, U. Schweizer, J. Köhrle, Selenium and selenoproteins in mammals: extraordinary, essential, enigmatic. *Cellular and Molecular Life Sciences CMLS*. **2004**, *61*, 1988.

[2] W. H. Organization, Guidelines for Drinking-water Quality. **2011**.

[3] M. Rovira, J. Giménez, M. Martínez, X. Martínez-Lladó, J. de Pablo, V. Marti, L. Duro, Sorption of selenium (IV) and selenium (VI) onto natural iron oxides: goethite and hematite. *Journal of hazardous materials*. **2008**, *150*, 279.

[4] F. M. Fordyce, *Selenium deficiency and toxicity in the environment*, Springer, **2013**.

[5] P. M. Haygarth, Global importance and global cycling of selenium. *Selenium in the Environment*. **1994**, 1.

[6] H. Mayland, *Selenium in plant and animal nutrition*, Marcel-Dekker, New York, **1994**.

[7] L. Jacobs, Selenium in Agriculture and the Environment. *Soil Science*. **1990**, *149*, 121.

[8] P. Zhang, D. L. Sparks, Kinetics of selenate and selenite adsorption/desorption at the goethite/water interface. *Environmental science & technology*. **1990**, *24*, 1848.

[9] US-EPA, National Primary Drinking Water Regulations. **2009**.

[10] N. Takeno, Atlas of Eh-pH diagrams. Intercomparison of Thermodynamic Databases. Geological Survey of Japan Open File Report No. 419. National Institute of Advanced Industrial Science and Technology. *Research Center for Deep Geological Environments*. **2005**.

[11] A. O. L. Kyle Smith, Fredrick W. Vance, Evaluation of Treatment Techniques for Selenium Removal. *IWC 09-05*.

[12] EPRI, in *Technical Report 1005365*, (Ed: E. P. M. P. Chu), **2004**.

[13] D. T. Merrill, M. A. Manzione, D. S. Parker, J. J. Petersen, W. Chow, A. O. Hobbs, Field evaluation of arsenic and selenium removal by iron coprecipitation. *Environmental progress*. **1987**, *6*, 82.

[14] F. Fu, Q. Wang, Removal of heavy metal ions from wastewaters: A review. *Journal of Environmental Management*. **2011**, *92*, 407.

[15] L. Twidwell, "The Removal of Arsenic, Selenium and Metals from Aqueous Solution by Iron Precipitation and Reduction Techniques", presented at *TMS2011 Annual Meeting, San Diego, CA*, 2011.

[16] A. P. Murphy, Method of selectively removing selenium ions from an aqueous solution. *United States Patent 4,806,264*, 1989.

[17] K. Parida, B. Gorai, N. Das, S. Rao, Studies on Ferric Oxide Hydroxides: III. Adsorption of Selenite (SeO2− 3) on Different Forms of Iron Oxyhydroxides. *Journal of colloid and interface science*. **1997**, *185*, 355.

[18] S.-c. Tam, A. Chow, D. Hadley, Effects of organic component on the immobilization of selenium on iron oxyhydroxide. *Science of the total environment*. **1995**, *164*, 1.

[19] J. W. Mellor, Intermediate Inorganic Chemistry. *Longmans, Green & Co, London*. **1941**.

[20] E. E. Baruth, "Water treatment plant design", 2004.

[21] K. A. Fields, A. S. Chen, L. Wang, *Arsenic removal from drinking water by coagulation/filtration and lime softening plants*, National Risk Management Research Laboratory, Office of Research and Development, US Environmental Protection Agency, **2000**.

[22] R. A. Bergman, Membrane softening versus lime softening in Florida: A cost comparison update. *Desalination*. **1995**, *102*, 11.

[23] M. Y. Liao, S. J. Randtke, Predicting the removal of soluble organic contaminants by lime softening. *Water Research*. **1986**, *20*, 27.

[24] EPRI, Palo Alto **2004**.

[25] W. H. Goodman, United State Patent, **1996**.

[26] C. H. Yun, R. Prasad, A. K. Guha, K. K. Sirkar, Hollow fiber solvent extraction removal of toxic heavy metals from aqueous waste streams. *Industrial & engineering chemistry research*. **1993**, *32*, 1186.

[27] A. K. De, S. M. Khopkar, R. A. Chalmers, SOLVENT EXTRACTION OF METALS. **1970**.

[28] P. Hocquellet, M.-P. Candillier, Evaluation of microwave digestion and solvent extraction for the determination of trace amounts of selenium in feeds and plant and animal tissues by electrothermal atomic absorption spectrometry. *Analyst*. **1991**, *116*, 505.

[29] J. Chambers, B. McClellan, Enhancement of atomic absorption sensitivity for copper, cadmium, antimony, arsenic, and selenium by means of solvent extraction. *Analytical Chemistry*. **1976**, *48*, 2061.

[30] C. Slater, R. Ahlert, C. Uchrin, Applications of reverse osmosis to complex industrial wastewater treatment. *Desalination*. **1983**, *48*, 171.

[31] B. J. Mariñas, R. E. Selleck, Reverse osmosis treatment of multicomponent electrolyte solutions. *Journal of Membrane Science*. **1992**, *72*, 211.

[32] R. Rautenbach, A. Gröschl, Separation potential of nanofiltration membranes. *Desalination*. **1990**, *77*, 73.

[33] P. Eriksson, Nanofiltration extends the range of membrane filtration. *Environmental Progress*. **1988**, *7*, 58.

[34] Y. K. Kharaka, G. Ambats, T. S. Presser, R. A. Davis, Removal of selenium from contaminated agricultural drainage water by nanofiltration membranes. *Applied geochemistry*. **1996**, *11*, 797.

[35] J. Draxler, W. Fürst, R. Marr, Separation of metal species by emulsion liquid membranes. *Journal of membrane science*. **1988**, *38*, 281.

[36] J. Draxler, R. Marr, Emulsion liquid membranes part I: phenomenon and industrial application. *Chemical Engineering and Processing: Process Intensification*. **1986**, *20*, 319.

[37] S. MOHANTY, Emulsion liquid membranes. *Chemical engineering world*. **2004**, *39*, 35.

[38] Y. Zhang, J. Wang, C. Amrhein, W. T. Frankenberger, Removal of selenate from water by zerovalent iron. *Journal of environmental quality*. **2005**, *34*, 487.

[39] Y. Zhang, W. T. Frankenberger, Removal of selenate in river and drainage waters by Citrobacter braakii enhanced with zero-valent iron. *Journal of agricultural and food chemistry*. **2006**, *54*, 152.

[40] Y. Zhang, C. Amrhein, A. Chang, W. T. Frankenberger, Effect of zero-valent iron and a redox mediator on removal of selenium in agricultural drainage water. *Science of the Total Environment*. **2008**, *407*, 89.

[41] R. S. Oremland, J. T. Hollibaugh, A. S. Maest, T. S. Presser, L. G. Miller, C. W. Culbertson, Selenate reduction to elemental selenium by anaerobic bacteria in sediments and culture: biogeochemical significance of a novel, sulfate-

independent respiration. *Applied and Environmental Microbiology*. **1989**, *55*, 2333.

[42] M. Losi, W. Frankenberger, Reduction of selenium oxyanions by Enterobacter cloacae SLD1a-1: isolation and growth of the bacterium and its expulsion of selenium particles. *Applied and environmental microbiology*. **1997**, *63*, 3079.

[43] C. Garbisu, T. Ishii, T. Leighton, B. B. Buchanan, Bacterial reduction of selenite to elemental selenium. *Chemical geology*. **1996**, *132*, 199.

[44] D. Maiers, P. Wichlacz, D. Thompson, D. Bruhn, Selenate reduction by bacteria from a selenium-rich environment. *Applied and environmental microbiology*. **1988**, *54*, 2591.

[45] F. J. Schmidt, J. L. Royer, Sub microgram determination of arsenic, selenium, antimony and bismuth by atomic absorption utilizing sodium borohydride reduction. *Analytical Letters*. **1973**, *6*, 17.

[46] R. Bye, Critical examination of some common reagents for reducing selenium species in chemical analysis. *Talanta*. **1983**, *30*, 993.

[47] A. Afkhami, A. Safavi, A. Massoumi, Spectrophotometric determination of trace amounts of selenium with catalytic reduction of bromate by hydrazine in hydrochloric acid media. *Talanta*. **1992**, *39*, 993.

[48] E. van Hullenbusch, F. Farges, M. Lenz, P. Lens, G. E. Brown Jr, "Selenium speciation in biofilms from granular sludge bed reactors used for wastewater treatment", presented at *AIP Conference Proceedings,* 2007.

[49] S. L. Hockin, G. M. Gadd, Linked redox precipitation of sulfur and selenium under anaerobic conditions by sulfate-reducing bacterial biofilms. *Applied and environmental microbiology*. **2003**, *69*, 7063.

[50] D. J. Adams, T. M. Pickett, Google Patents, **2001**.

[51] D. M. Ruthven, Principles of adsorption and adsorption processes. **1984**.

[52] K. Panday, G. Prasad, V. Singh, Copper (II) removal from aqueous solutions by fly ash. *Water Research*. **1985**, *19*, 869.

[53] S. Wang, Y. Boyjoo, A. Choueib, Z. Zhu, Removal of dyes from aqueous solution using fly ash and red mud. *Water Research*. **2005**, *39*, 129.

[54] V. K. Gupta, I. Ali, Removal of lead and chromium from wastewater using bagasse fly ash—a sugar industry waste. *Journal of Colloid and Interface Science*. **2004**, *271*, 321.

[55] M. Rao, A. Parwate, A. Bhole, Removal of Cr 6+ and Ni 2+ from aqueous solution using bagasse and fly ash. *Waste Management*. **2002**, *22*, 821.

[56] K. Kadirvelu, K. Thamaraiselvi, C. Namasivayam, Removal of heavy metals from industrial wastewaters by adsorption onto activated carbon prepared from an agricultural solid waste. *Bioresource Technology*. **2001**, *76*, 63.

[57] K. Kadirvelu, M. Kavipriya, C. Karthika, M. Radhika, N. Vennilamani, S. Pattabhi, Utilization of various agricultural wastes for activated carbon preparation and application for the removal of dyes and metal ions from aqueous solutions. *Bioresource technology*. **2003**, *87*, 129.

[58] L. Monser, N. Adhoum, Modified activated carbon for the removal of copper, zinc, chromium and cyanide from wastewater. *Separation and Purification Technology*. **2002**, *26*, 137.

[59] M. Kobya, E. Demirbas, E. Senturk, M. Ince, Adsorption of heavy metal ions from aqueous solutions by activated carbon prepared from apricot stone. *Bioresource Technology*. **2005**, *96*, 1518.

[60] K. Kadirvelu, C. Namasivayam, Activated carbon from coconut coirpith as metal adsorbent: adsorption of Cd (II) from aqueous solution. *Advances in Environmental Research*. **2003**, *7*, 471.

[61] M. Corapcioglu, C. Huang, The adsorption of heavy metals onto hydrous activated carbon. *Water Research*. **1987**, *21*, 1031.

[62] K. Kadirvelu, C. Faur-Brasquet, P. L. Cloirec, Removal of Cu (II), Pb (II), and Ni (II) by adsorption onto activated carbon cloths. *Langmuir*. **2000**, *16*, 8404.

[63] A. Netzer, D. Hughes, Adsorption of copper, lead and cobalt by activated carbon. *Water Research*. **1984**, *18*, 927.

[64] E. Erdem, N. Karapinar, R. Donat, The removal of heavy metal cations by natural zeolites. *Journal of Colloid and Interface Science*. **2004**, *280*, 309.

[65] U. Wingenfelder, C. Hansen, G. Furrer, R. Schulin, Removal of heavy metals from mine waters by natural zeolites. *Environmental science & technology*. **2005**, *39*, 4606.

[66] R. M. Izatt, R. L. Bruening, M. L. Bruening, B. J. Tarbet, K. E. Krakowiak, J. S. Bradshaw, J. J. Christensen, Removal and separation of metal

ions from aqueous solutions using a silica-gel-bonded macrocycle system. *Analytical Chemistry*. **1988**, *60*, 1825.

[67] R. A. Jacques, R. Bernardi, M. Caovila, E. C. Lima, F. A. Pavan, J. C. Vaghetti, C. Airoldi, Removal of Cu (II), Fe (III), and Cr (III) from aqueous solution by aniline grafted silica gel. *Separation Science and Technology*. **2007**, *42*, 591.

[68] A. Sarkar, P. Datta, M. Sarkar, Sorption recovery of metal ions using silica gel modified with salicylaldoxime. *Talanta*. **1996**, *43*, 1857.

[69] A. Genz, A. Kornmüller, M. Jekel, Advanced phosphorus removal from membrane filtrates by adsorption on activated aluminium oxide and granulated ferric hydroxide. *Water Research*. **2004**, *38*, 3523.

[70] Y. Kim, C. Kim, I. Choi, S. Rengaraj, J. Yi, Arsenic removal using mesoporous alumina prepared via a templating method. *Environmental science & technology*. **2004**, *38*, 924.

[71] S. M. Maliyekkal, S. Shukla, L. Philip, I. M. Nambi, Enhanced fluoride removal from drinking water by magnesia-amended activated alumina granules. *Chemical Engineering Journal*. **2008**, *140*, 183.

[72] H. Yang, R. Xu, X. Xue, F. Li, G. Li, Hybrid surfactant-templated mesoporous silica formed in ethanol and its application for heavy metal removal. *Journal of Hazardous Materials*. **2008**, *152*, 690.

[73] J. Aguado, J. M. Arsuaga, A. Arencibia, M. Lindo, V. Gascón, Aqueous heavy metals removal by adsorption on amine-functionalized mesoporous silica. *Journal of Hazardous Materials*. **2009**, *163*, 213.

[74] A. Sayari, S. Hamoudi, Y. Yang, Applications of pore-expanded mesoporous silica. 1. Removal of heavy metal cations and organic pollutants from wastewater. *Chemistry of materials*. **2005**, *17*, 212.

[75] L. Mercier, T. J. Pinnavaia, Access in mesoporous materials: Advantages of a uniform pore structure in the design of a heavy metal ion adsorbent for environmental remediation. *Advanced Materials*. **1997**, *9*, 500.

[76] A. Liu, K. Hidajat, S. Kawi, D. Zhao, A new class of hybrid mesoporous materials with functionalized organic monolayers for selective adsorption of heavy metal ions. *Chemical Communications*. **2000**, 1145.

[77] M. M. Ghosh, C. D. Cox, J. R. Yuan‐Pan, Adsorption of selenium on hydrous alumina. *Environmental progress*. **1994**, *13*, 79.

[78] L. S. Balistrieri, T. Chao, Selenium adsorption by goethite. *Soil Science Society of America Journal*. **1987**, *51*, 1145.

[79] L. S. Balistrieri, T. Chao, Adsorption of selenium by amorphous iron oxyhydroxide and manganese dioxide. *Geochimica et Cosmochimica Acta*. **1990**, *54*, 739.

[80] K. F. Hayes, A. L. Roe, G. E. BROWN JR, K. O. Hodgson, J. O. Leckie, G. A. Parks, In situ X-ray absorption study of surface complexes: Selenium oxyanions on α-FeOOH. *Science*. **1987**, *238*, 783.

[81] K. F. Hayes, C. Papelis, J. O. Leckie, Modeling ionic strength effects on anion adsorption at hydrous oxide/solution interfaces. *Journal of Colloid and Interface Science*. **1988**, *125*, 717.

[82] S.-L. Lo, T.-Y. Chen, Adsorption of Se (IV) and Se (VI) on an iron-coated sand from water. *Chemosphere*. **1997**, *35*, 919.

[83] H. W. Kroto, A. W. Allaf, S. P. Balm, C60: Buckminsterfullerene. *Chemical Reviews*. **1991**, *91*, 1213.

[84] S. Iijima, Helical microtubules of graphitic carbon. *nature*. **1991**, *354*, 56.

[85] K. Novoselov, A. Geim, S. Morozov, D. Jiang, Y. Zhang, S. Dubonos, I. Grigorieva, A. Firsov, Electric field effect in atomically thin carbon films. *Science*. **2004**, *306*, 666.

[86] A. K. Geim, K. S. Novoselov, The rise of graphene. *Nature materials*. **2007**, *6*, 183.

[87] H. K. Chae, D. Y. Siberio-Pérez, J. Kim, Y. B. Go, M. Eddaoudi, A. J. Matzger, M. O'Keeffe, O. M. Yaghi, A route to high surface area, porosity and inclusion of large molecules in crystals. *Nature*. **2004**, *427*, 523.

[88] L. S. Schadler, S. C. Giannaris, P. M. Ajayan, Load transfer in carbon nanotube epoxy composites. *Applied Physics Letters*. **1998**, *73*, 3842.

[89] Y. Zhang, Y. W. Tan, H. L. Stormer, P. Kim, Experimental observation of the quantum Hall effect and Berry's phase in graphene. *Nature*. **2005**, *438*, 201.

[90] K. S. Novoselov, A. K. Geim, S. V. Morozov, D. Jiang, M. I. Katsnelson, I. V. Grigorieva, S. V. Dubonos, A. A. Firsov, Two-dimensional gas of massless Dirac fermions in graphene. *Nature*. **2005**, *438*, 197.

[91] K. S. Novoselov, E. McCann, S. V. Morozov, V. I. Fal’ko, M. I. Katsnelson, U. Zeitler, D. Jiang, F. Schedin, A. K. Geim, Unconventional

quantum Hall effect and Berry's phase of 2π in bilayer graphene. *Nature Physics*. **2006**, *2*, 177.

[92] M. I. Katsnelson, K. S. Novoselov, A. K. Geim, Chiral tunnelling and the Klein paradox in graphene. *Nature Physics*. **2006**, *2*, 620.

[93] M. I. Katsnelson, K. Novoselov, Graphene: New bridge between condensed matter physics and quantum electrodynamics. *Solid State Communications*. **2007**, *143*, 3.

[94] W. Stevenson, in *BREAKING NEWS* Enago, **2010**.

[95] K. C. Kemp, H. Seema, M. Saleh, K. Mahesh, V. Chandra, K. S. Kim, Environmental applications using graphene composites: water remediation and gas adsorption. *Nanoscale*. **2013**.

[96] V. Chandra, J. Park, Y. Chun, J. W. Lee, I.-C. Hwang, K. S. Kim, Water-dispersible magnetite-reduced graphene oxide composites for arsenic removal. *ACS nano*. **2010**, *4*, 3979.

[97] A. Y. Romanchuk, A. S. Slesarev, S. N. Kalmykov, D. V. Kosynkin, J. M. Tour, Graphene oxide for effective radionuclide removal. *Physical Chemistry Chemical Physics*. **2013**, *15*, 2321.

[98] F. Liu, S. Chung, G. Oh, T. S. Seo, Three-dimensional graphene oxide nanostructure for fast and efficient water-soluble dye removal. *ACS Applied Materials & Interfaces*. **2012**, *4*, 922.

[99] Z. Niu, J. Chen, H. H. Hng, J. Ma, X. Chen, A leavening strategy to prepare reduced graphene oxide foams. *Advanced Materials*. **2012**, *24*, 4144.

[100] M. Z. Iqbal, A. A. Abdala, Oil spill cleanup using graphene. *Environmental Science and Pollution Research*. **2012**, 1.

[101] F. Ahme, D. F. Rodrigues, Investigation of acute effects of graphene oxide on wastewater microbial community: A case study. *Journal of hazardous materials*. **2013**.

[102] E. N. Wang, R. Karnik, Water desalination: Graphene cleans up water. *Nature Nanotechnology*. **2012**, *7*, 552.

[103] T. M. Suzuki, D. A. P. Tanaka, M. A. L. Tanco, M. Kanesato, T. Yokoyama, Adsorption and removal of oxo-anions of arsenic and selenium on the zirconium (IV) loaded polymer resin functionalized with diethylenetriamine-N, N, N′, N′ -polyacetic acid. *J. Environ. Monit.* **2000**, *2*, 550.

[104] G. Moffat, R. Williams, C. Webb, R. Stirling, Selective separations in environmental and industrial processes using magnetic carrier technology. *Minerals Engineering*. **1994**, *7*, 1039.

[105] Z. Xu, Review of magnetic carrier technologies for metal ion removal. *Physical Separation in Science and Engineering*. **1999**, *9*, 169.

[106] M. Martinez, J. Gimenez, J. De Pablo, M. Rovira, L. Duro, Sorption of selenium (IV) and selenium (VI) onto magnetite. *Applied surface science*. **2006**, *252*, 3767.

[107] M. Duc, G. Lefevre, M. Fédoroff, Sorption of selenite ions on hematite. *Journal of colloid and interface science*. **2006**, *298*, 556.

[108] J. A. Davis, J. O. Leckie, Surface ionization and complexation at the oxide/water interface II. Surface properties of amorphous iron oxyhydroxide and adsorption of metal ions. *Journal of Colloid and Interface Science*. **1978**, *67*, 90.

[109] R. O. James, G. A. Parks, in *Surface and colloid science*, Springer, 1982, 119.

[110] K. Hayes, J. Leckie, Modeling ionic strength effects on cation adsorption at hydrous oxide/solution interfaces. *Journal of Colloid and Interface Science*. **1987**, *115*, 564.

[111] D. Yates, T. Healy, Mechanism of anion adsorption at the ferric and chromic oxide/water interfaces. *Journal of Colloid and Interface Science*. **1975**, *52*, 222.

[112] R. Cornell, P. Schindler, Infrared study of the adsorption of hydroxycarboxylic acids onα-FeOOH and amorphous Fe (III) hydroxide. *Colloid and Polymer Science*. **1980**, *258*, 1171.

[113] R. Parfitt, J. Russell, Adsorption on hydrous oxides. IV. Mechanisms of adsorption of various ions on goethite. *Journal of Soil Science*. **1977**, *28*, 297.

[114] J. B. Harrison, V. E. Berkheiser, Anion interactions with freshly prepared hydrous iron oxides. *Clays Clay Miner*. **1982**, *30*, 97.

Chapter 2 Experimental Section

2.1 Chemicals

Natural graphite (7 - 10 micro), potassium permanganate ($KMnO_4$), sodium nitrate ($NaNO_3$), H_2O_2 (30 %), 1-methyl-2-pyrrolidone (NMP), Ferric acetylacetonate ($Fe(acac)_3$), H_2SO_4 (98 %) were purchased from Alfa Aesar. 0.001 N HCl, 0.1 N NaOH and acetone were purchased from Fisher Scientific Company. Milli-Q water was used in all aqueous solution and lavations.

2.1 Adsorbents Synthesis

2.1.1 Preparation of GO

GO was prepared by a modified Hummers method.[1] Firstly, natural graphite flake (7 - 10 micron, 2 g) and $NaNO_3$ (1.5 g) were mixed in a three necked flask. Then H_2SO_4 (98 %, 150 mL) was added to the mixture in an ice-bath while a mechanical agitation was maintained. After $KMnO_4$ (9 g) was slowly added, the stirring was kept in ice bath for 2 h. Then the ice bath was taken away and the agitation continued for another 5 days at room temperature. Then, a portion of H_2O_2 (6 mL) was added into the mixture to neutralize unreacted $KMnO_4$, and the generated O_2 helped with the exfoliation of GO layers. After another 2 hours of agitation, the resulting bright yellow suspension was diluted and washed with a mixed solution (250 mL) with H_2SO_4 (98 %, 7.5 mL), H_2O_2 (30 %, 4.17 mL) and Milli-Q water. Then sediment was washed repeatedly using Milli-Q until pH neutral. The sediment would be dialyzed for another 5 days to clean out remnant dissolved ions. After an ultrasonic dispersion, fluffy golden flocci GO was attained using freeze dryer.

2.1.2 Preparation of MGO

A modified method according to Shen's was applied.[2] GO (100 mg) was dispersed in of 1-methyl-2-pyrrolidone (NMP, 30mL) by ultrasonication at room temperature. Then the mixture was heated to 190 ℃ under the nitrogen atmosphere. $Fe(acac)_3$ (1.413 g, 4 mmol) was dissolved in NMP (20 mL) and added dropwise for about 1hour to the GO/NMP solution under vigorous stirring. Different from Shen's method, the stirring continued for another 4 hours after the dropping was finished. This modified procedure could increase the magnetism of the composite. After cooling down to room temperature, the mixture was washed several times by acetone and water alternatively. The precipitate was collected by magnetic separation and was then dispersed in water using sonication. The resulting black powder was collected using freeze drying.

2.1.3 Preparation of MGO-EG

A high temperature organic solvent reflux method was applied. GO (500 mg) was dispersed in of 1-methyl-2-pyrrolidone (NMP, 150 mL) by ultrasonication at room temperature, and the mixture was heated to 220 ℃ under a nitrogen atmosphere. Precursor $Fe(acac)_3$ (7.065 g, 20 mmol) was dissolved in NMP (100mL)/EG (50 mL) mixture and added dropwise for about 1h to GO/NMP solution under vigorous stirring. The stirring continued for another 5h after the dropping was finished. After cooling down to room temperature, the mixture was washed several times by acetone and water alternatively. The precipitate was collected by magnetic separation. The resulting black powder was collected using freeze dryer.

2.2 Selenium Adsorption Experiments

Adsorption experiments were conducted to study the effects of the initial selenium concentration, adsorption time, systema pH, temperature and with the existence of interfering ions (NO_3^-, SO_4^{2-}, PO_4^{3-}, Ca^{2+}, and Mg^{2+}). Adsorbent MGO-EG (20 mg, the dosage of absorbents was 1 g L^{-1}) was added to Selenite and Selenate standard liquid solution (20 mL, prepared from diluting 1000 ppm Na_2SeO_3 and Na_2SeO_4 stock water solutions), mixing uniformly. While controlled temperature was remained, samples were placed in the shaker chamber and oscillated for given hours at 300 rpm. NaOH and HCl were used to adjust system pH. MGO-EG was separated from solutions for reproducibility by applying a hand magnet. Then the supernatant was collected for further ICP-MS and IC analysis for ion concentrations. After washing with diluted NaOH (0.001 N, pH ~ 10) to desorb selenium; and the adsorbent was reactivated with diluted HCl (0.001 N, pH ~ 3). MGO-EG was reused to repeat the exact experiments with the same initial selenium concentration and oscillation time for reusability.

2.3 Characterization Methods

2.3.1 AFM

Atomic Force Microscope (AFM) is a high resolution scanning probe microscopy technique, which is widely applied for the materials surface properties study of from the atomic to the micron levels.

AFM has been used to solve the processing and materials problems in wide range of technologies fields including the electronics, telecommunications, biological, chemical, automotive, aerospace, and energy industries.[3] The investigated materials sample can be thin and thick film coatings, ceramics, composites, glasses, synthetic and biological membranes, metals, polymers, and semiconductors.[4] The main AFM applications include study of the abrasion, adhesion, cleaning, corrosion, etching, friction, lubrication, plating, and polishing.[5] By applying AFM, imaging of the surface in atomic resolution and measure the force at nano-newton scale can be achieved. The publications related to the AFM are growing rapidly after its birth.[6] Recently, chemical bond between atoms are observed in graphene by AFM, which reveals the complex surface reaction mechanisms.[7]

Figure 2-1 show the principles of AFM force measurement. The AFM detection system does not directly measure the force between the tip and the sample surface or the height profile for imaging; instead, it senses the deflection of the microcantilever. The laser beam source can be reflected by a cantilever, which is displaced via its interaction with the surface. The changes of cantilever deflection can be sensed and the signal will be transferred by the photodiode. The detector receives the signal and provides electronics feedback for the cantilever to move along the surface accordingly. The electric-piezo can facilitate tiny but accurate movements on electronic command and enable the very precise scanning. Knowing the stiffness of the cantilever, the force could thus be calculated by Hook's law:

$$F = -kz \tag{1}$$

where F is the force, k is the stiffness of the lever, and z is the distance the lever is bent.

The AFM imaging modes include tapping mode (the non-contact mode) and contact mode. Tapping mode was applied in this thesis to avoid the potential damage for the sample surface. In tapping mode, the tip of the cantilever does not contact the sample surface directly. The cantilever is instead oscillated at either its resonant frequency (frequency modulation) or just above (amplitude modulation), where the amplitude of oscillation is typically a few nanometers (< 10 nm) down to a few Pico-meters. When the tip is close enough to the sample, the van der Waals forces (normally the strongest force that is from 1 nm to 10 nm above the surface) or other long range forces will act to decrease the resonance frequency of the cantilever. This decrease in resonant frequency can be sensed. The controller will smoothly adjust the average tip-to-sample distance by maintain a constant oscillation amplitude or frequency, which is combined with the feedback loop system. Measuring the tip-to-sample distance at each (x, y) data point allows the scanning software to construct a topographic image of the sample surface.[4, 6]

In this work, the AFM was conducted using an Asylum MFP-3D system with the tapping mode. GO samples for AFM imaging were prepared by dropping GO water solution onto a fresh prepared mica surface and dried overnight. AFM images of GO nanosheets were obtained thereafter. The layer number of GO could be determined by the height profile from the section.[8]

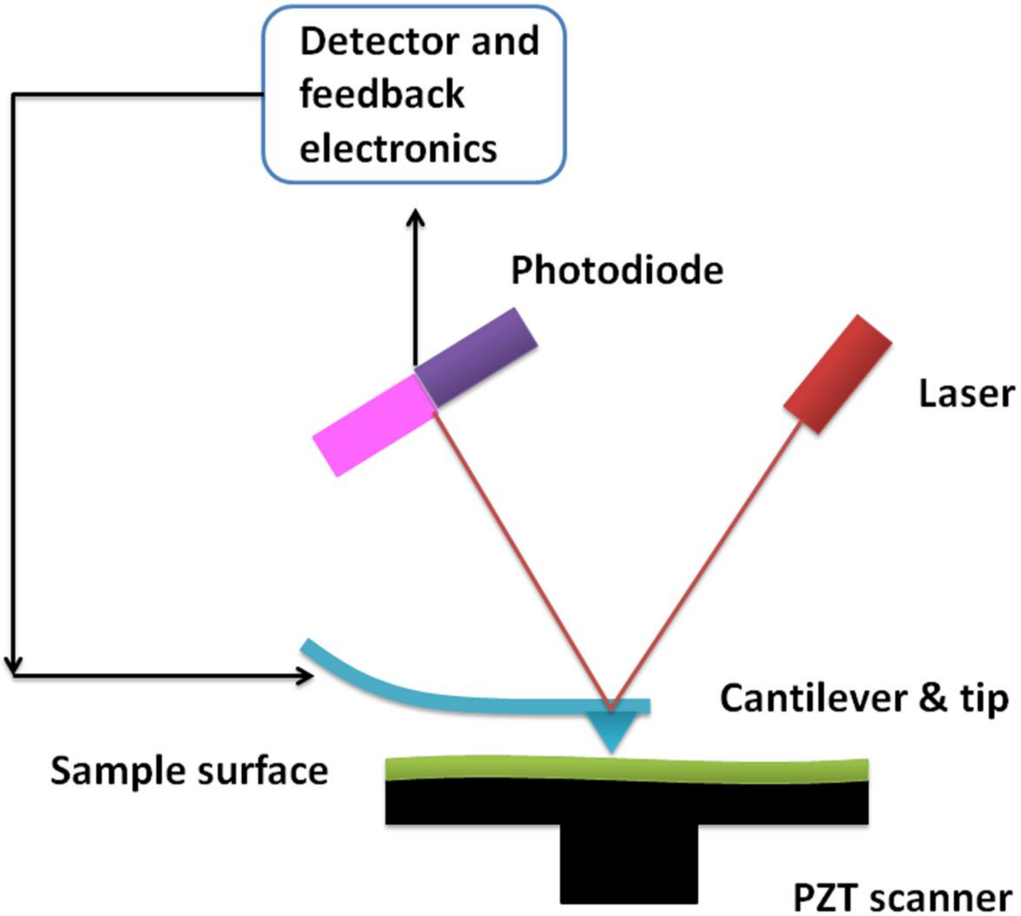

Figure 2-1 Block diagram of AFM using beam deflection detection.[1]

---

[1] Figure 2-1 is adapted from Wikipedia (http://en.wikipedia.org/wiki/Atomic_force_microscopy).

2.3.2 XRD

X-Ray Diffraction (XRD) is a rapid analytical technique primarily used for phase identification of a crystalline material and can provide other information on the crystallinity and particle size in this thesis. The analyzed material is typically finely ground, homogenized, thus the average bulk composition can be determined accurately.[9]

A crystal structure, being considered as being build up by stacking of layers or planes, can be treated as a semi-transparent mirror. X-rays that have a wavelength similar to the distances between these layers or planes can be reflected. Thus the angle of reflection is equal to the angle of incidence. This behavior is defined as diffraction, and it is described by Bragg’s Law:[10]

$$2dsin\theta = n\lambda \tag{2}$$

One the Bragg’s Law is satisfied, constructive interference of diffracted X-ray beams will occur and a Bragg reflection will be picked up by a detector scanning at this certain angle. These reflection angles indicate the inter-layer spacing (or known as d-spacing) of atoms in the crystal structure, according to the Bragg’s Law. Peak intensities provide information about how much X-ray scattering is contributing to that reflection, which mean the specific location of particular atoms in the crystal structure, and the specific phase ratio in the sample. By comparing the special peak locations (the inflection angles), one can identify the phases in the crystal structure.

As is shown in Figure 2-2, A powder X-ray diffraction meter consists of an X-ray source (usually an X-ray tube), a sample stage, a detector and the way to vary angle θ. When the X-ray is focused on the sample at a certain angle θ, the detector opposite to the source can obtain the intensity of the X-ray by reading the 2θ value that detected away from the source path. In this way, the X-ray intensity can be obtained more accurately.[10, 11]

Analysis of the diffraction pattern allows the identification of phases, the quantity of each phase, the crystallinity, the relative lattice parameters, crystallite size and strain within the provided sample. The analysis of XRD results normally is the first step on characterization and quality control of the targeting materials.

In this work, X-Ray Diffraction was taken on a RIGAKU Rotating anode XRD system with a copper anode, 40 kv, 2 degs minute^{-1}. XRD would identify the substance of GO and iron oxide. Calculation with Scherrer's equation could indicate the particle size of iron oxide.[12]

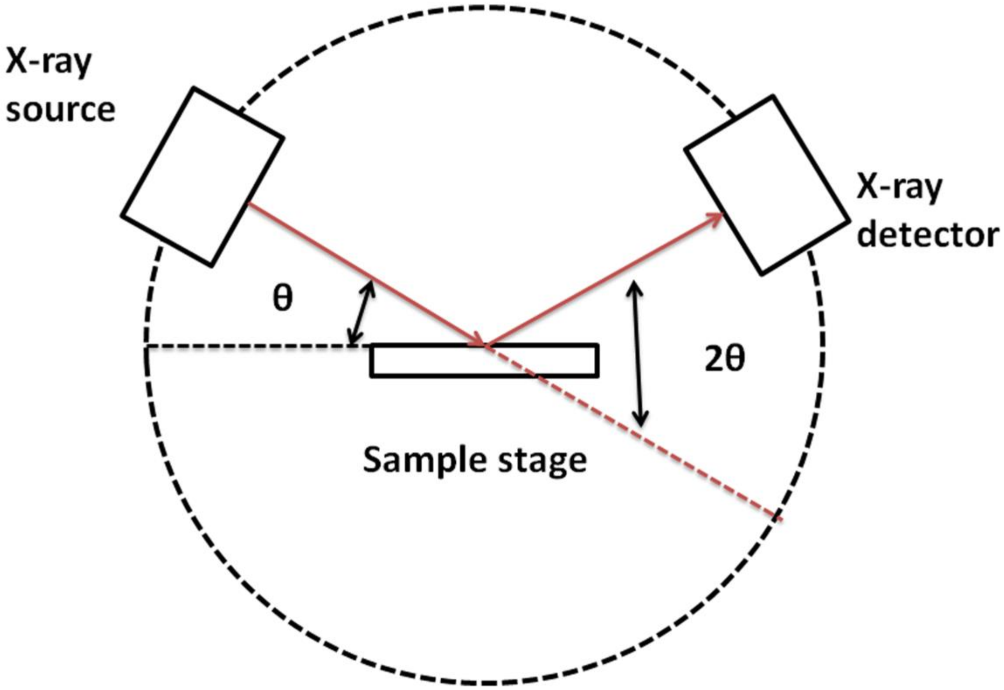

Figure 2-2 Diagram of the powder X-ray diffract meter.[2]

2.3.3 FTIR

FTIR spectrometers (Fourier Transform Infrared Spectrometer) are widely used in characterization of organic synthesis, polymer science, petrochemical engineering, pharmaceutical industry and food analysis. In addition, since FTIR spectrometers can be connected to chromatography, the mechanism of chemical reactions and the detection of unstable substances can be investigated with the combination instruments. [13]

---

[2] Figure 2-2 is adapted from ChemWiki-UC Davis (http://chemwiki.ucdavis.edu/Analytical_Chemistry/Instrumental_Analysis/Diffraction/Powder_X-ray_Diffraction).

The range of infrared region is 12800 ~ 10 cm^{-1}, which can be divided into near-infrared region (12800 ~ 4000 cm^{-1}), mid-infrared region (4000 ~ 200 cm^{-1}) and far-infrared region (50 ~ 1000 cm^{-1}).[14] Infrared spectrum is a molecular vibrational spectrum. The dipole moment of sample molecules changes after exposed to infrared radiation. As a result, the vibration energy level of the sample molecules transfers from ground state to excited state. It should be noted that the sample molecules only selectively adsorb radiation with specific wavelength. The frequency of the adsorption peak is determined by the vibration energy gap. Therefore, the structure information (such as the functional group types) of the sample molecule can be obtained by analyzing the infrared spectrum. The commonly used region for infrared absorption spectroscopy is 4000 ~ 400 cm^{-1}, where located the absorption radiation of most organic compounds and inorganic ions.[15, 16]

The FTIR spectrometers are the third generation infrared spectrometer, with the advantages of: (1) The signal-to-noise ratio of spectrum is significantly higher than the previous generation infrared spectrometers. (2) The accuracy of wavenumber is high, with the error range within ± 0.01 cm^{-1}. (3) The scan time of all frequencies is short (approximately 1 s). (4) The resolution is extremely high (0.1 ~ 0.005 cm^{-1}). (5) The scan range is wide (1000 ~ 10 cm^{-1}). (6) The interference from stray light is reduced. Due to these advantages, FTIR Spectrometers have replaced dispersive IR spectrometers.[13]

A common FTIR spectrometer consists of a coherent light source, beam splitter, sample compartment, a stationary mirror, a moving mirrow, detector, amplifier, A/D convertor, and a computer. The light source goes through a beam splitter and the light recombined by two mirrors and passes the sample, and then reaches the detector. Then the signal is amplified and converted to digital signal for Fourier transform analysis, carried out by a computer. Figure 2-3 is a block diagram of an FTIR spectrometer.[14]

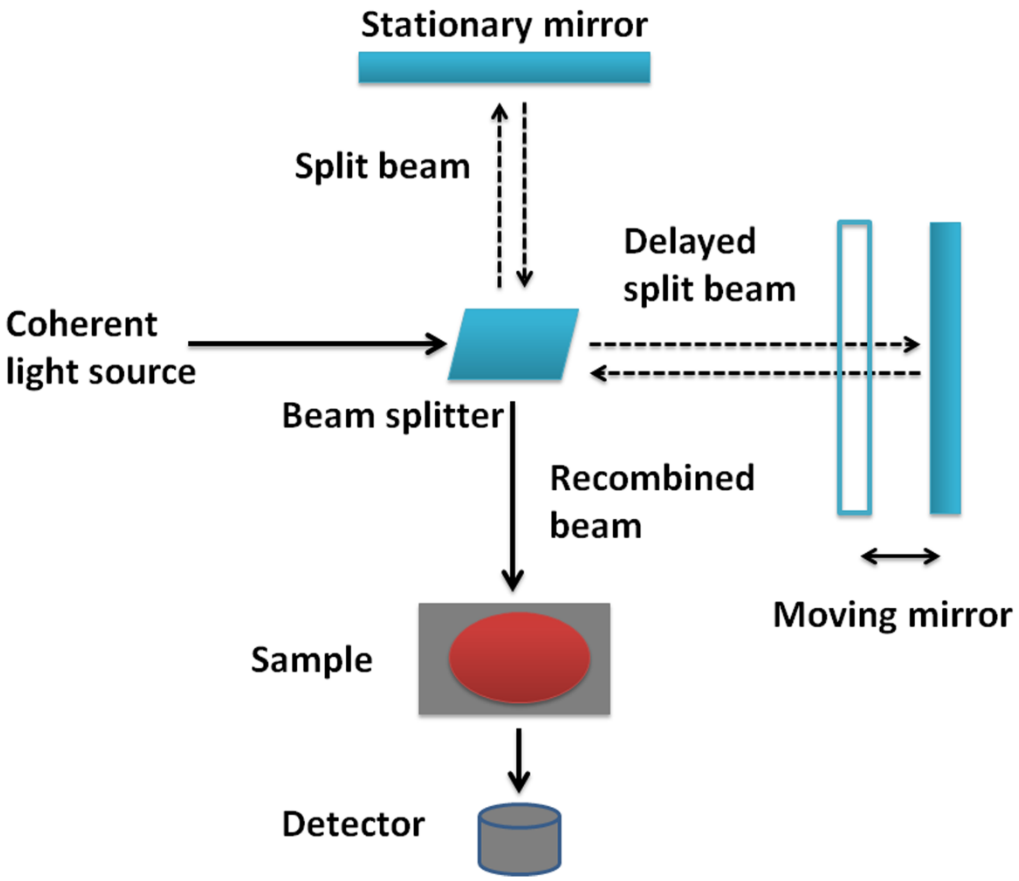

Figure 2-3 Schematic diagram of a Michelson interferometer, configured for FTIR.[3]

---

[3] Figure 2-3 is adapted from Wikipedia (http://en.wikipedia.org/wiki/Fourier_transform_infrared_spectroscopy).

In this thesis, FTIR spectra were recorded on Nicolet iS50 FT-IR Imaging System, and is mainly used for the determination of functional groups on GO and MGO/MGO-EG.[17]

2.3.4 XPS

X-ray Photoelectron Spectroscopy (XPS) is a widely used technique to investigate the chemical composition of sample surfaces. Information that could be obtained by XPS analysis including: the identification of elements near the surface and surface composition; the local chemical environments; the oxidation states of transition metals; the valence band electronic structure and the morphology of thin films.[18]

XPS works by irradiating a sample with mono energetic soft x-rays and causing electrons (1s, 2s, 2p, etc.) to be ejected (see Figure 2-4).[19] The ejected photoelectron has kinetic energy:[20]

$$KE = hv - BE - \varphi_{spec} \tag{3}$$

where,

KE = Electron Kinetic Energy;

BE = Electron Binding Energy;

φ_{spec} = Spectrometer Work Function.

Sample elements can be identified directly from the kinetic energies of these ejected photoelectrons. The photoelectron intensities indicate the relative concentrations of elements. Another important advantage of XPS is its ability to obtain information on chemical states from the variations in binding energies, or chemical shifts, of the photoelectron lines.[21]

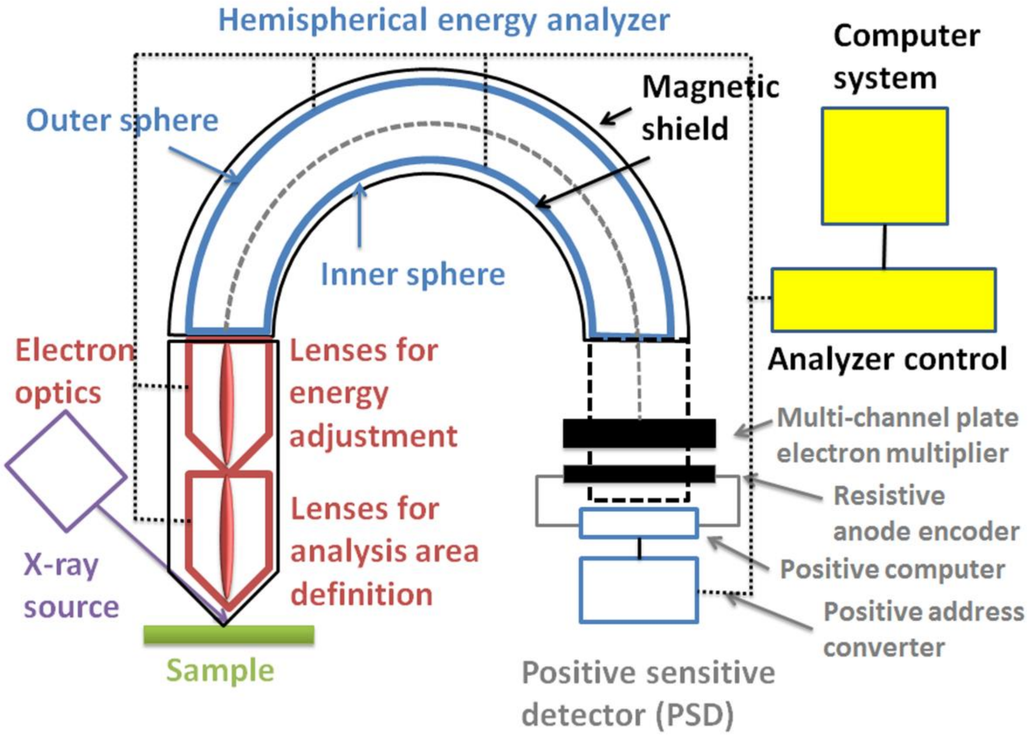

Figure 2-4 Principle of XPS (figure adapted from literature[22]).

In this thesis, XPS was conducted using AXIS 165 XPS Spectrometer. All the bonding energies have been corrected by referring to the C 1s photoelectron peak at 284.8 eV.[20] In this work, XPS was used to determine the type and relative amount of chemical bondings between carbon, oxygen and iron.[23]

2.3.5 TGA

Thermogravimetric Analysis (TGA) measures weight changes in the sample as a function of temperature (or time) under a precisely controlled atmosphere (shown in Figure 2-5). Its major applications include the measurement of thermal stability and composition of the sample. Inorganic materials, metals, polymers and plastics, ceramics, glasses, and composite materials can be analyzed.[24] In recent decades, TGA has been applied increasingly for the quality control of raw materials and incoming goods as well as for failure analysis of finished parts, especially in the polymer processing industry. [25]

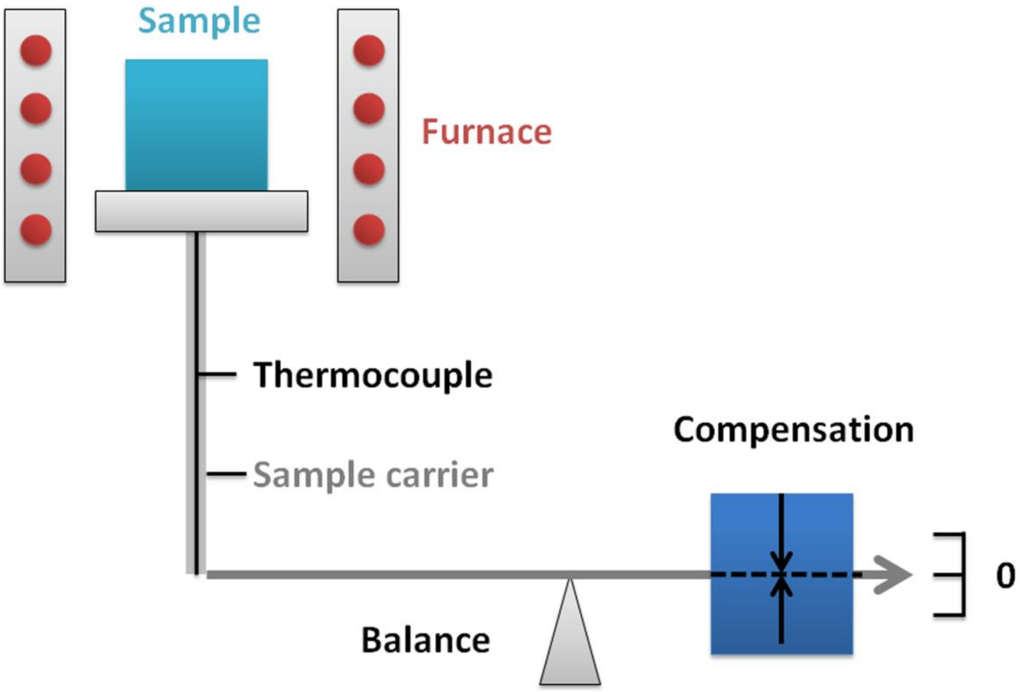

Figure 2-5 Principle of TGA measurement (figure adapted from literature[26]).

TGA was conducted in this thesis with TA Instrument Q-500 equipment, with a heating rate of 10°C min^{-1} and nitrogen as the purge gas. Before the tests, all the samples were carefully ground to powders to ensure sufficient diffusion of heat. The measurements were conducted using ~ 20 mg samples, and weight retention/temperature curves were recorded. TGA analyses of graphite, GO, and MGO/MGO-EG samples could indicate the thermo stability as well as the relative content of iron oxide, carbon and oxygen containing groups.[2]

2.3.6 TEM

The Transmission Electron Microscope (TEM) is a widely used and powerful microscope that utilizes energetic electrons to provide high-resolution morphologic, compositional and crystallographic information on samples[27] at a maximum potential magnification of 1 nanometer.

A TEM produces a high-resolution, black and white image by the interaction between the prepared samples and energetic electrons, which is taken place in a vacuum chamber. The vacuum chamber allows free movement of electrons with pumped air. The electrons then pass through multiple electromagnetic lenses to the screen, where the electrons are converted to light and form an image (shown in Figure 2-6). The imaging quality of certain sample can be manipulated by adjusting the speed of electrons through the electron gun voltage modification. During the transmission, the speed of electrons directly correlates to electron wavelength: the faster the electrons movement, the shorter wavelength and the greater the quality and more details of the image. In the images, the lighter areas represent the places where more electrons pass through, while the darker areas reflect the dense areas of the object. These differences provide information on the structure, texture, shape and size of the sample.[28, 29]

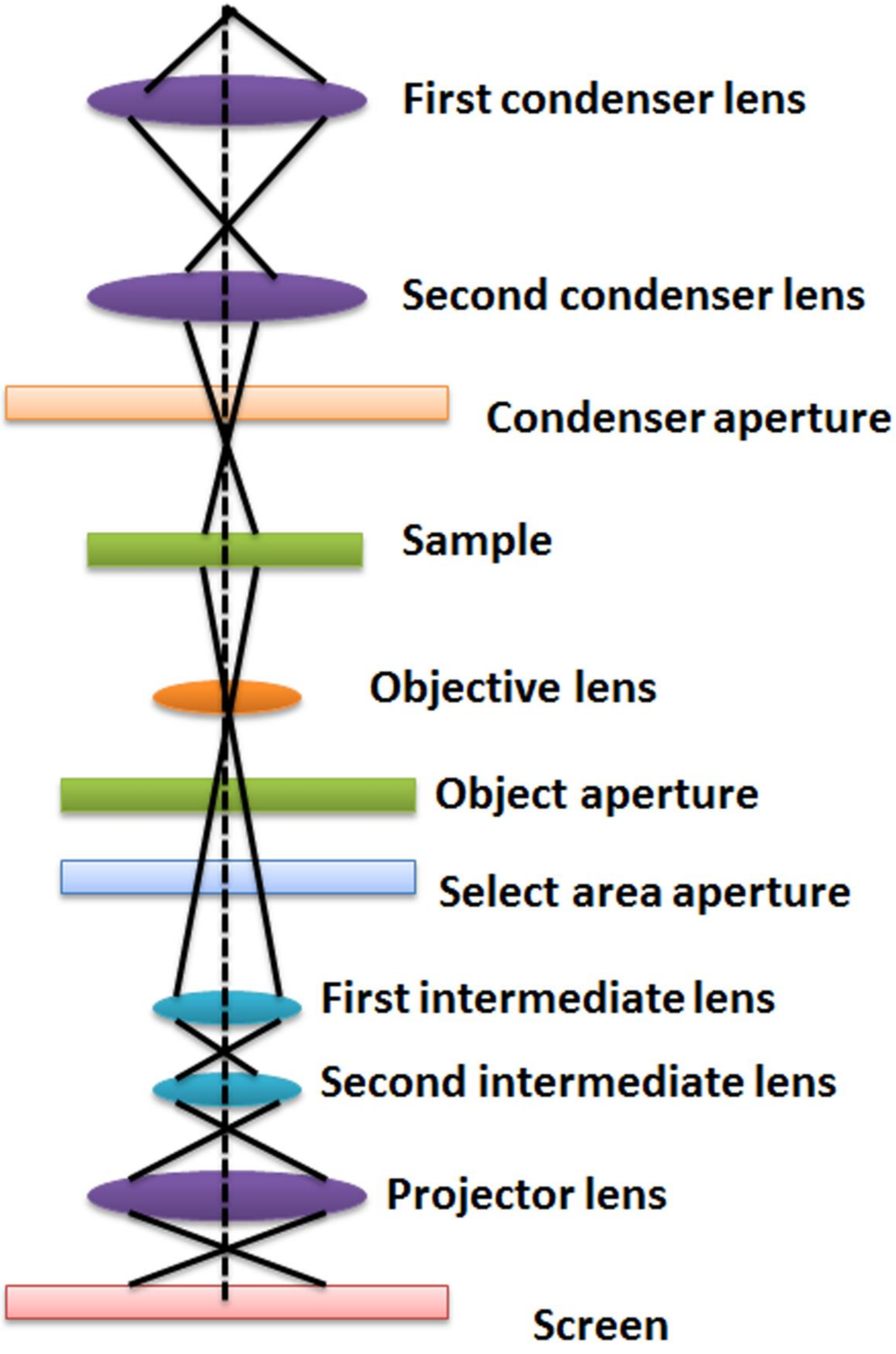

Figure 2-6 Instrument of Transmission Electron Microscope (figure adapted from literature[30]).

In this work, investigation of morphology was performed by TEM using a Hitachi HF 3300 Mode. TEM samples were prepared by pipetting several microliters of GO and MGO-EG dispersion on to lacey carbon coated copper grids and dried. In this work, TEM is mainly used to observe the morphology of GO, and MGO/MGO-EG, as well as determine the crystallinity and d-spacing of iron oxide with HR-TEM.[31]

2.3.7 SEM

The Scanning Electron Microscope (SEM) uses a focused beam of high-energy electrons to generate a variety of signals at the surface of solid specimens to obtain the high resolution image.[32]

Figure 2-7 shows how the SEM works. A beam of electrons is generated at the top of the microscope by an electron gun. The electron beam follows a vertical path through the microscope, which is held within a vacuum chamber. After travelling through the electromagnetic fields and lenses, the electron beam hits the prepared sample, ejecting backscattered electrons and X-rays. Detectors will collect and convert the electron and X-rays information to a signal that is sent to a screen and produces the final image.[33]

The signals that derive from electron-sample interactions reveal the information about the sample including texture, chemical composition, crystalline structure and orientation of materials making up the sample.[34]

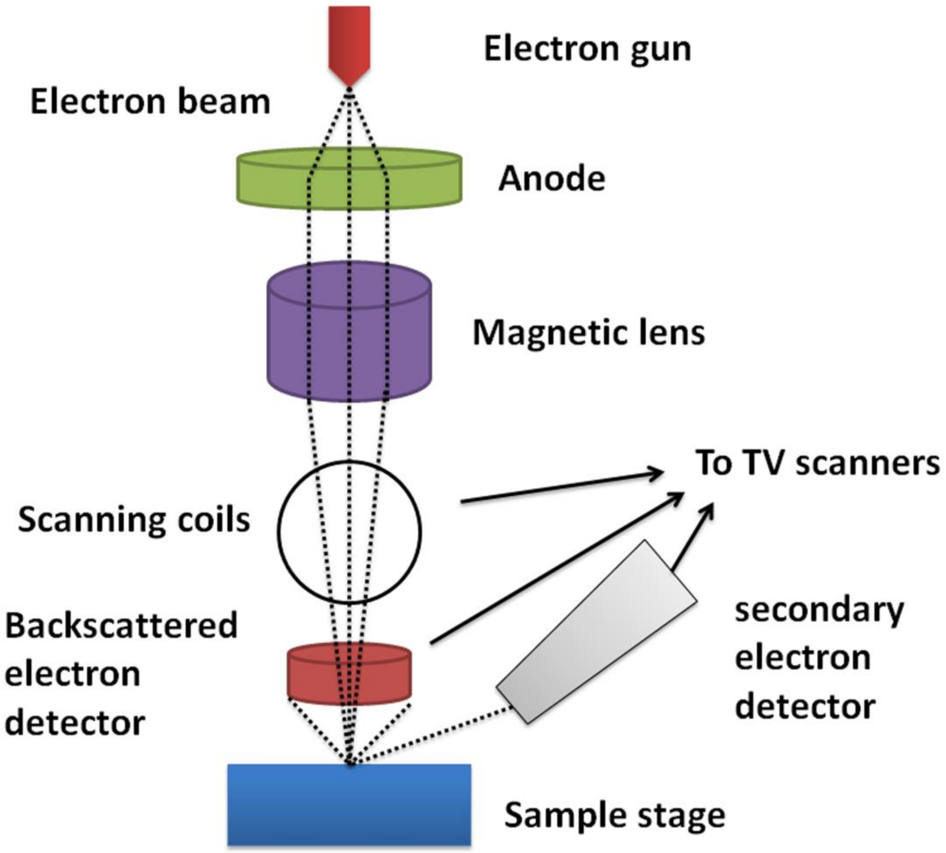

Figure 2-7 Diagram of SEM imaging.[4]

In this work, SEM Vega-3 (Tescan) was used in this thesis for imaging and EDS elements analyse of GO, MGO and MGO-EG.

2.3.8 Magnetic properties measurement

When a ferromagnetic material is magnetized in one specific direction, it will not relax back to zero magnetization when the external magnetizing field is removed. At zero magnetic field strength, the magnetization is offset from the origin (zero) by an amount called the remanence. An additional magnetic field

---

[4] Figure 2-7 is adapted from University of Virginia, Environmental, Health, and Safety. (http://ehs.virginia.edu/ehs/ehs.rs/rs.rpeelectronmicroscope.html).

must be applied in the opposite direction. The intensity of the applied magnetic field is called coercivity. If an alternating magnetic field is applied to the material, its magnetization will trace out a loop, known as the hysteresis loop. The lack of retraceability of the magnetization curve is the property called hysteresis and it is related to the existence of magnetic domains in the material. [35, 36]

Quantum Design 9T-PPMS magnetometer was used in this work to obtain the magnetic hysteresis curve.

2.3.9 Zeta potential measurement

Zeta potential (as is illustrated in Figure 2-8) is the electric potential in the interfacial double layer (DL) at the location of the slipping plane versus a point in the bulk fluid away from the interface. In other words, zeta potential is the potential difference between the dispersion medium and the stationary layer of fluid attached to the dispersed particle.[37]

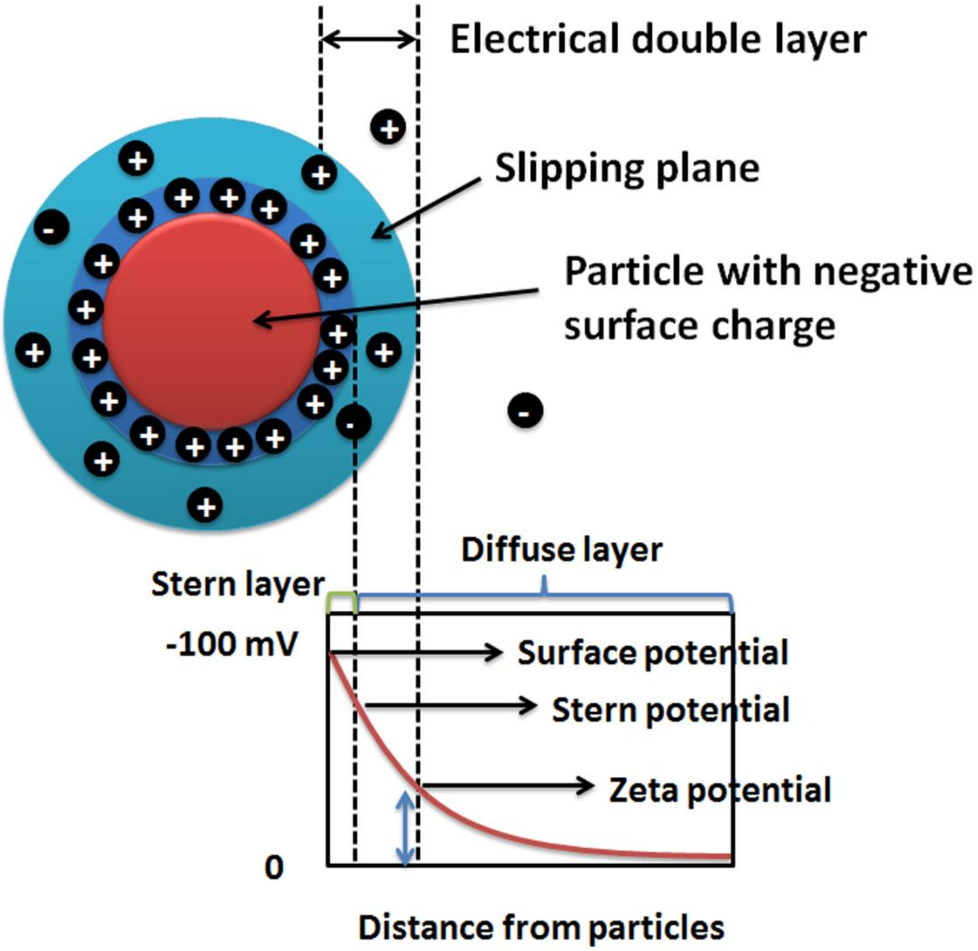

Figure 2-8 Schematic representation of zeta potential.[5]

The main applications of zeta potential measurement include: relative comparison of various systems with regard to their surface properties to predict or monitor stability of colloidal systems; identification of the isoelectric point (or point of zero zeta potential) of colloids; particle surface adsorption and morphology identification.[38]

---

[5] Figure 2-8 is adapted from Malvin, Zeta potential measurement using laser Doppler electrophoresis (LDE) (http://www.malvern.com.br/labeng/technology/zeta_potential/zeta_potential_LDE.htm).

Zeta potential was measured in this thesis with a ZetaPALS Zeta potential analyser. All samples for zeta potential measurements were carefully dispersed in water solution with ultrasonic for 10 min. In this work, zeta potential for GO and MGO/MGO-EG were used to determine their surface charge properties and stability.[39, 40]

2.3.10 ICP-MS

The Inductively Coupled Plasma Mass Spectrometry (ICP-MS) is a very sensitive analytical technique that can determine the elemental content of samples. The element content or the ion concentration is determined by detecting and counting the number of ions of the specific element of a certain element mass. It is capable of analyzing all elements from Li to U and can be applied to solutions, solids and gasses. The ICP-MS detects only elemental ions and can determine the individual isotopes of each element.[41]

The ICP-MS samples are transferred by an argon flow (solutions are vaporized using a nebulizer; solids should be sampled using laser ablation; gasses can be sampled directly) into a high-energy argon plasma that consists of positively charged argon ions and electrons. In this plasma, the sample can be atomization and ionization under an effective temperature of 7000 K. Then the produced elemental ions in the inductively coupled plasma (ICP) are transferred from 7000 K to room temperature and from atmospheric pressure to high vacuum and enable the element identification in the sample.

It should be noted that besides ions, photons are also produced in the plasma and passing through the apertures, potentially affect the result accuracy. Since these photons cannot be removed by vacuum, they produce high background signal when they reach the detector. To minimize this background noise, the photon-stop (shown in Figure 2-9), which is a small metal plate placed in the center of the aperture, is present. The photon-stop reflects the photons away from the detector.

Subsequently, the ion beam enters the quadrupole mass analyzer, where the ions are separated and identified based on their mass-to-charge ratio. Each element has its own characteristic isotopes and masses and therefore will produce its own mass spectrum. After passing the quadrupole the ions hit a special detector, which contains two stages to allow simultaneous measurements of high and low signals. This special detector allows simultaneous detection of main components and ultra-trace elements in a single run, which makes the ICP-MS a perfect tool for survey analysis of totally unknown samples.[41-44]

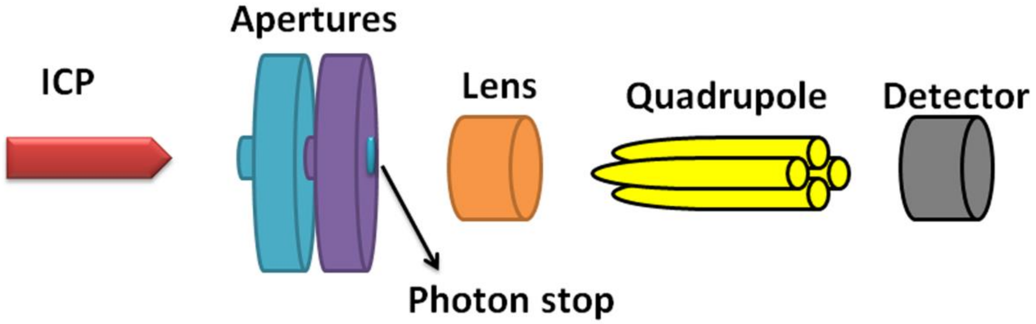

Figure 2-9 Layout of ICP-MS (figure adapted from literature[45]).

Perkin Elmer's Elan 6000 Inductively Coupled Plasma-Mass Spectrometry (ICP-MS) was applied in this work for concentration detection of ions (selenite, selenate, Ca^{2+}, Mg^{2+}) at ppb level.

2.3.11 IC

Ion Chromatography (IC) is a form of liquid chromatography, using ion-exchange resins to separate atomic and molecular ions for ionic species concentrations analysis. Ion chromatographs are widely used for water chemistry analysis to measure the concentrations of major anions, such as fluoride, chloride, nitrate, nitrite, and sulfate.[46, 47]

According to ion species type and size, ionic species can be separate differently. Sample solutions pass through a pressurized chromatographic column where ions are absorbed by column constituents. While an ion extraction liquid (known as eluent) runs through the column, the absorbed ions begin separating from the column. The retention time of different species determines the ionic concentrations in the sample.[48, 49]

Ion Chromatography (IC) DX-600 by Dionexwas was used in this work to test the concentration of anoins (NO_3^-, SO_4^{2-}, PO_4^{3-}) at ppm level.

2.4 References

[1] W. Lv, D.-M. Tang, Y.-B. He, C.-H. You, Z.-Q. Shi, X.-C. Chen, C.-M. Chen, P.-X. Hou, C. Liu, Q.-H. Yang, Low-temperature exfoliated graphenes:

vacuum-promoted exfoliation and electrochemical energy storage. *Acs Nano*. **2009**, *3*, 3730.

[2] J. Shen, Y. Hu, M. Shi, N. Li, H. Ma, M. Ye, One Step Synthesis of Graphene Oxide− Magnetic Nanoparticle Composite. *The Journal of Physical Chemistry C*. **2010**, *114*, 1498.

[3] P. Hansma, V. Elings, O. Marti, C. Bracker, Scanning tunneling microscopy and atomic force microscopy: application to biology and technology. *Science*. **1988**, *242*, 209.

[4] G. Binnig, C. F. Quate, C. Gerber, Atomic force microscope. *Physical review letters*. **1986**, *56*, 930.

[5] H.-J. Butt, B. Cappella, M. Kappl, Force measurements with the atomic force microscope: Technique, interpretation and applications. *Surface science reports*. **2005**, *59*, 1.

[6] A. Trache, G. A. Meininger, Atomic force microscopy (AFM). *Current Protocols in Microbiology*. **2008**, 2C. 2.1.

[7] D. G. de Oteyza, P. Gorman, Y.-C. Chen, S. Wickenburg, A. Riss, D. J. Mowbray, G. Etkin, Z. Pedramrazi, H.-Z. Tsai, A. Rubio, Direct Imaging of Covalent Bond Structure in Single-Molecule Chemical Reactions. *Science*. **2013**, *340*, 1434.

[8] S. Stankovich, D. A. Dikin, R. D. Piner, K. A. Kohlhaas, A. Kleinhammes, Y. Jia, Y. Wu, S. T. Nguyen, R. S. Ruoff, Synthesis of graphene-based nanosheets via chemical reduction of exfoliated graphite oxide. *Carbon*. **2007**, *45*, 1558.

[9] P.-O. Renault, X-Ray Diffraction (XRD). **2010**.

[10] H. P. Klug, L. E. Alexander, X-ray diffraction procedures: for polycrystalline and amorphous materials. *X-Ray Diffraction Procedures: For Polycrystalline and Amorphous Materials, 2nd Edition, by Harold P. Klug, Leroy E. Alexander, pp. 992. ISBN 0-471-49369-4. Wiley-VCH, May 1974.* **1974**, *1*.

[11] I. A. Courtney, J. Dahn, Electrochemical and in situ X‐ray diffraction studies of the reaction of lithium with tin oxide composites. *Journal of The Electrochemical Society*. **1997**, *144*, 2045.

[12] G. Wang, J. Yang, J. Park, X. Gou, B. Wang, H. Liu, J. Yao, Facile synthesis and characterization of graphene nanosheets. *The Journal of Physical Chemistry C*. **2008**, *112*, 8192.

[13] P. Griffiths, J. A. De Haseth, *Fourier transform infrared spectrometry*, Vol. 171, John Wiley & Sons, **2007**.

[14] M. VAN DE WEERT, Fourier Transform Infrared. *Methods for Structural Analysis of Protein Pharmaceuticals*. **2005**, *3*, 131.

[15] B. C. Smith, *Fundamentals of Fourier transform infrared spectroscopy*, CRC press, **2011**.

[16] O. Faix, in *Methods in lignin chemistry*, Springer, 1992, 83.

[17] X. Zhang, Y. Huang, Y. Wang, Y. Ma, Z. Liu, Y. Chen, Synthesis and characterization of a graphene–C60 hybrid material. *Carbon*. **2009**, *47*, 334.

[18] M.-F. Bouvy, X-ray photoelectron spectroscopy (XPS). **2008**.

[19] J. D. Andrade, in *Surface and interfacial aspects of biomedical polymers*, Springer, 1985, 105.

[20] J. F. Moulder, J. Chastain, R. C. King, *Handbook of X-ray photoelectron spectroscopy: a reference book of standard spectra for identification and interpretation of XPS data*, Physical Electronics Eden Prairie, MN, **1995**.

[21] N. McIntyre, D. Zetaruk, X-ray photoelectron spectroscopic studies of iron oxides. *Analytical Chemistry*. **1977**, *49*, 1521.

[22] F. Owner, in *Fisitech*, **2011**.

[23] D. Yang, A. Velamakanni, G. Bozoklu, S. Park, M. Stoller, R. D. Piner, S. Stankovich, I. Jung, D. A. Field, C. A. Ventrice Jr, Chemical analysis of graphene oxide films after heat and chemical treatments by X-ray photoelectron and micro-Raman spectroscopy. *Carbon*. **2009**, *47*, 145.

[24] J. D. Menczel, R. B. Prime, *Thermal analysis of polymers, fundamentals and applications*, Wiley. com, **2009**.

[25] R. B. Prime, H. E. Bair, S. Vyazovkin, P. K. Gallagher, A. Riga, Thermogravimetric analysis (TGA). *Thermal Analysis of Polymers, Fundamentals and Applications, Wiley, Hoboken, NJ*. **2009**, 241.

[26] *Thermogravimetric Analysis – TGA Method, Technique, Applications*, NETZSCH.

[27] S. Bajt, A. Barty, K. Nugent, M. McCartney, M. Wall, D. Paganin, Quantitative phase-sensitive imaging in a transmission electron microscope. *Ultramicroscopy*. **2000**, *83*, 67.

[28] L. Reimer, H. Kohl, *Transmission electron microscopy: physics of image formation*, Vol. 36, Springer, **2008**.

[29] D. B. Williams, C. B. Carter, *The Transmission Electron Microscope*, Springer, **1996**.

[30] Y. Ding, Fundamental Theory of Transmission Electronic Microscopy.

[31] V. Chandra, J. Park, Y. Chun, J. W. Lee, I.-C. Hwang, K. S. Kim, Water-dispersible magnetite-reduced graphene oxide composites for arsenic removal. *ACS nano*. **2010**, *4*, 3979.

[32] M. Razeghi, DTIC Document, **1996**.

[33] J. Venables, C. Harland, Electron back-scattering patterns—A new technique for obtaining crystallographic information in the scanning electron microscope. *Philosophical Magazine*. **1973**, *27*, 1193.

[34] J. Goldstein, D. E. Newbury, D. C. Joy, C. E. Lyman, P. Echlin, E. Lifshin, L. Sawyer, J. R. Michael, *Scanning electron microscopy and X-ray microanalysis,* Springer, **2003**.

[35] E. C. Stoner, E. Wohlfarth, A mechanism of magnetic hysteresis in heterogeneous alloys. *Philosophical Transactions of the Royal Society of London. Series A. Mathematical and Physical Sciences*. **1948**, 599.

[36] E. Della Torre, E. Della Torre, *Magnetic hysteresis*, IEEE press New York, **1999**.

[37] R. J. Hunter, *Zeta potential in colloid science: principles and applications*, Vol. 125, Academic press London, **1981**.

[38] A. Revil, P. Pezard, P. Glover, Streaming potential in porous media: 1. Theory of the zeta potential. *Journal of Geophysical Research: Solid Earth (1978–2012)*. **1999**, *104*, 20021.

[39] Y. Si, E. T. Samulski, Synthesis of water soluble graphene. *Nano Letters*. **2008**, *8*, 1679.

[40] D. Li, M. B. Mueller, S. Gilje, R. B. Kaner, G. G. Wallace, Processable aqueous dispersions of graphene nanosheets. *Nature nanotechnology*. **2008**, *3*, 101.

[41] A. Montaser, *Inductively coupled plasma mass spectrometry*, Vol. 515, Wiley-vch New York, **1998**.

[42] K. E. Jarvis, A. L. Gray, R. S. Houk, *Handbook of inductively coupled plasma mass spectrom etry*, Blackie. Chapman and Hall, **1992**.

[43] P. W. J. M. Boumans, Inductively coupled plasma emission spectroscopy. Part II: applications and fundamentals. Volume 2. **1987**.

[44] M. Thompson, J. N. Walsh, *A handbook of inductively coupled plasma spectrometry*, Blackie & Son Ltd., **1983**.

[45] *nductively Coupled Plasma-Mass Spectrometry (ICP-MS)*, Koninklijke Philips Electronics N.V., **2008**.

[46] R. D. Rocklin, E. L. Johnson, Determination of cyanide, sulfide, iodide, and bromide by ion chromatography with electrochemical detection. *Analytical Chemistry*. **1983**, *55*, 4.

[47] J. Mulik, R. Puckett, D. Williams, E. Sawicki, Ion chromatographic analysis of sulfate and nitrate in ambient aerosols. *Analytical Letters*. **1976**, *9*, 653.

[48] P. R. Haddad, P. E. Jackson, *Ion chromatography: principles and applications*, Elsevier Amsterdam, **1990**.

[49] J. G. Tarter, Ion chromatography. **1987**.

Chapter 3 Water-Dispersible Magnetic Nanoparticle−Graphene Oxide Composites for Selenium Removal[6]

3.1 Introduction

Selenium is an essential nutrient element for life in trace amount, but extremely toxic at higher concentrations.[1] It has the narrowest ranges between dietary deficiency (< 40 μg day^{-1}) and toxic levels (> 400 μg day^{-1}).[2] The World Health Organization (WHO) currently set 40 ppb (40 μg L^{-1}) as the Maximum Acceptable Concentration (MAC) in drinking water.[2] Selenium compounds can be released to the environment during the combustion of coal and petroleum fuels, mining and extraction processes of coal and metals (e.g. copper, lead, zinc, uranium). It has been estimated that 76,000–88,000 tons per year[3] of selenium are released globally from anthropogenic activity, which are released to soil and water and then can be transferred to plants, animal organisms and life cycles, resulting in serious health and environmental issues. The short term health effect that selenium potentially causes includes: hair and fingernail changes, damage to the peripheral nervous system, and fatigue and irritability; while in long term, selenium can cause hair and fingernail loss, damage to kidney and liver tissue as well as the nervous and circulatory systems.[4] Selenium normally exists in four oxidation states: selenide (Se^{2-}), amorphous or polymeric elemental selenium (Se^0), selenite (SeO_3^{2-}), and selenate (SeO_4^{2-}), of which Se (VI) and Se (IV) are

---

[6] A version of this chapter has been submitted for publication. Y. Fu, J. Wang, Q. Liu, H. Zeng 2013. Carbon (under review).

more mobile and toxic. Se (VI) is the major concerned selenium specie in water due to its high solubility and bioavailability. Removal of the water-borne selenium has attracted much rapidly increasing attention over the last decade, which can help reduce the bioaccumulation of selenium and protect aquatic ecosystems.

Different methods have been applied for selenium removal: adsorption, coagulation/filtration, lime softening, reverse osmosis, anion exchange, distillation, and electrodialysis,[4] among which the adsorption method holds the advantages of removal efficiency, simple process and economy. Adsorption method has been reported to be effective in removing many heavy metal cations and metalloid anions. However, most conventional adsorbents, such as silica gel, clay, activated carbon, molecular sieve, ferric oxyhydroxide, and activated aluminum oxide, have certain adsorption capacity of Se (IV) but show very poor performances (typically < 50 %) in Se (VI) removal.[5] It was proposed that Se (IV) forms an inner-sphere adsorption on ferric oxy-hydroxides, while Se (VI) is normally absorbed by the adsorbents in an outer-sphere adsorption manner which is much weaker than the inner-sphere adsorption,[6-11] which could be the reason of less effective Se (VI) removal using conventional adsorbents. Thus, there is an urgent need to develop efficient and reusable adsorbent materials for the removal of the water-borne selenium with high removal capacity.

Hydrophilic monolayer Graphene Oxide (GO) and graphene based adsorbents have attracted much attention recently and demonstrate promising performance in removal of heavy metal ions,[12] anions,[13] radionuclide[14], organic contaminations,[15, 16] oil spill-ups,[17] and microbial community[18]. Although there is no study available on the application of GO based adsorbents in selenium removal, GO still can be considered as an adsorbent candidate for selenium oxyanions removal because of its high surface area, abundant surface hydroxyl and carboxyl functional groups, and easy modification. In addition, iron oxides, such as magnetite,[19] goethite,[7, 11, 20-22] and hematite,[22, 23] have been reported to show certain degree of selenite removal. The interesting surface properties of GO and iron oxide have stimulated the development of a novel adsorbent materials for selenium removal by functionalizing the GO sheets with magnetic iron oxide nanoparticles, which can also expedite the separation of GO under an external magnetic field for the reuse of the adsorbents.

In this work, the synthesis of Magnetic particle-Graphene Oxide composites (MGO) nanocomposite adsorbents and their application in selenium removal were reported. The impacts of initial selenium concentration, adsorption time, and pH on the removal of selenium with two different selenium oxidation states (i.e., Se (VI) and Se (IV)) have also been explored.

3.2 Results and Discussion

To synthesize the water-dispersible Magnetic particle-Graphene Oxide composites for the removal of selenium, GO was first prepared from natural graphite using a modified Hummers Method.[24] MGO was synthesized using a high temperature solution reaction based on a modified Shen’s method.[25] GO and MGO were characterized for the substance identification, morphology, and surface binding modes.

3.2.1 Atomic Force Microscopy (AFM) imaging

The typical Atomic Force Microscopy (AFM) image and height profile of GO are shown in Figure 3-1. With the introduction of naturally hydrophilic oxygen-containing groups, GO tends to exfoliate in aqueous solution and form a stable suspension. The AFM height profile shows that the thickness of dispersed GO layer is ~ 1.03 nm, indicating a monolayer of GO sheet.[26] GO sheets are expected to be thicker than pristine graphene monolayer with a well-known van der Waals thickness of ~ 0.34 nm. This is due to the addition of covalently bounded oxygen and the displacement of the sp^3-hybridized carbon atoms slightly above and below the original graphene plane.

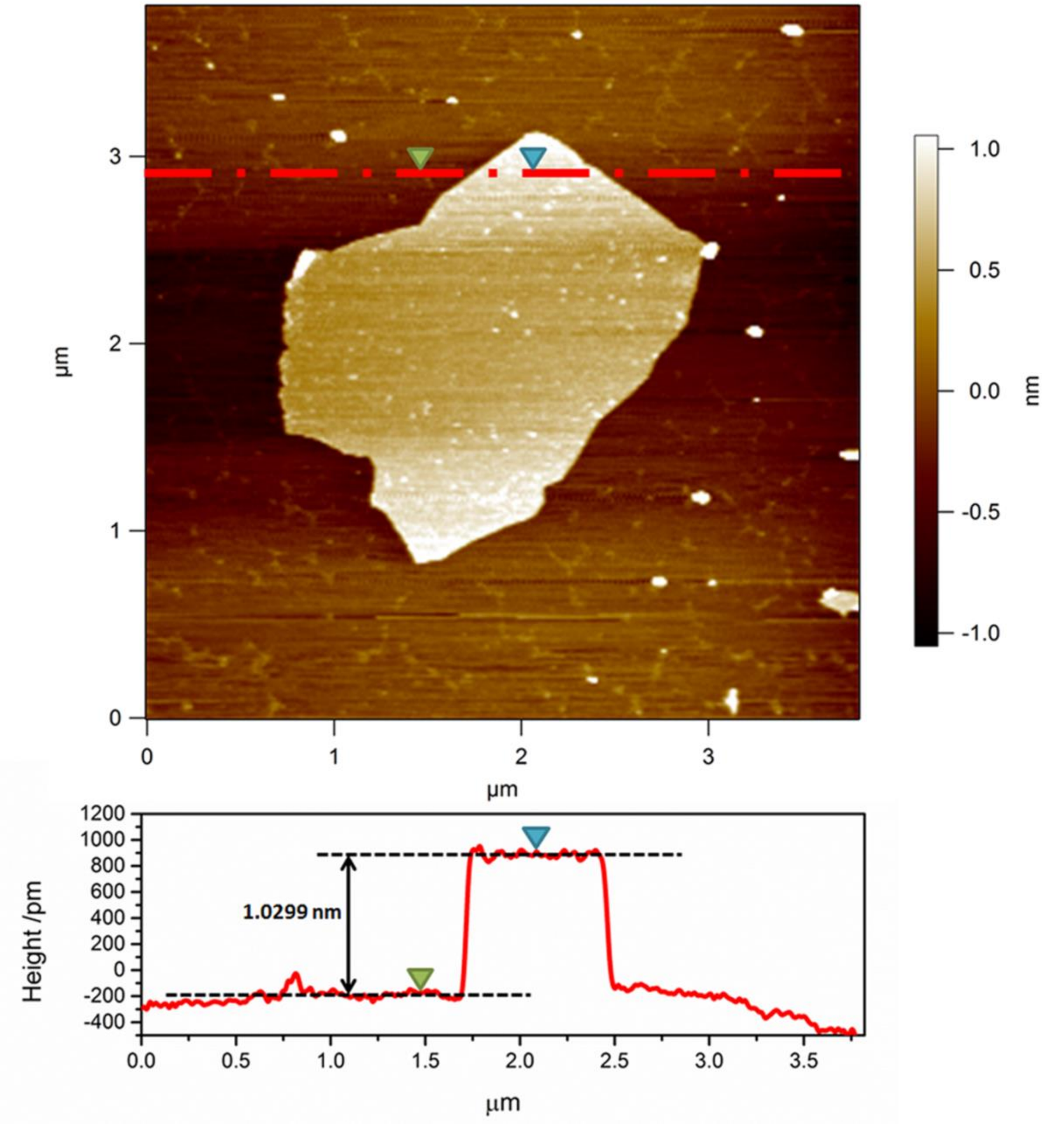

Figure 3-1 Tapping mode AFM image of GO sheets with height profile for mono layer GO (~ 1.03 nm).

3.2.2 X-ray diffraction (XRD) analysis

The powder X-ray diffraction (XRD) patterns of graphite, GO and MGO are shown in Figure 3-2. The XRD signal intensity values of the strongest peaks in each substance are set as 1, respectively; and the other peaks are normalized according to their relative intensity ratios to the strongest peak. As calculated from Bragg Equation ($2d\sin\theta = \lambda$), the interlayer spacing of GO is 0.85 nm (2θ = 10.4 °; λ is the wavelength of X-ray, ~ 1.54 Å), which is much larger than the *d*-spacing of graphite (0.34 nm). The spacing difference is mainly due to the addition of oxygen-containing functional groups on the GO planes.

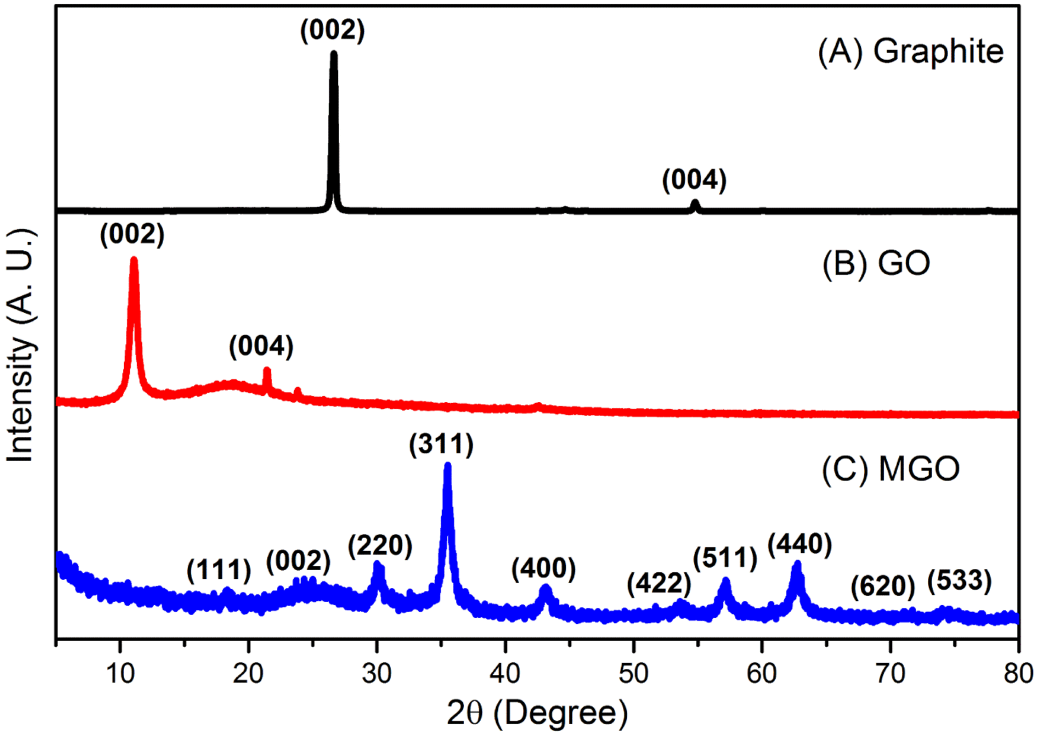

Figure 3-2 Powder X-ray diffraction patterns of (a) graphite, (b) GO and (c) MGO.

The XRD pattern of MGO indicates that the composite contains mostly Fe_3O_4 particles. The diffraction peaks at 2θ = 18.3 °, 30.2 °, 35.5 °, 43.1 °, 53.5 °, 57.0 °, 62.4 °, 70.9 °, and 73.9 ° match well with those from the JCPDS card (19-0629) for Fe_3O_4, and can be assigned to (111), (220), (311), (400), (422), (511), (440), (620) and (533) of crystal planes of Fe_3O_4. The broadening diffraction peaks with high intensity indicates that the particles are highly crystalline with a size of 16.09 nm according to the Sherrer's Equation, $D = K\lambda\ (\beta^*\cos(\theta))^{-1}$, where $K = 0.89$,[27] D represents the crystallite size, λ is the wavelength of Cu K_α (0.154 nm), and β is the full width at half maximum (radian) of the diffraction peak.

3.2.3 Fourier Transform Infrared Spectroscopy (FTIR) analysis

The Fourier Transform Infrared Spectroscopy (FTIR) spectra of natural graphite, GO, and MGO powders are shown in Figure 3-3. The overlapping intensity band at 2951 cm^{-1}, 2871 cm^{-1}, and 2835 cm^{-1} are attributed to the asymmetric or symmetric stretch of C-H bond in methyl or methylene groups respectively on graphite. Several similar peaks between 735 cm^{-1} to 1616 cm^{-1}, specifically around 735/860/783 cm^{-1}, 1221/1049 cm^{-1}, and 1572/1616 cm^{-1} can be observed on the spectra of graphite, GO and MGO, which are attribute to C-$(CH_2)_n$, C-O and C-C vibrations in the aromatic ring carbon structure. Sharp peaks appear at 1714 and 1749 cm^{-1} for both GO and MGO illustrating a characteristic frequency of C=O, which is either located in carboxyl and carbonyl groups or on the edge of GO.[28-31] In the FTIR spectra of GO, a peak observed at 3239 cm^{-1} attributing to O-H, which is located on the GO basal plane;[28-31] while in MGO, this peak significantly decreased, indicating a loss of hydroxyl group and the reduction of GO sheets, which suggests the breaking of O-H bond, caused by the formation of a new Fe-O bond, which is in accordance with the XRD results.

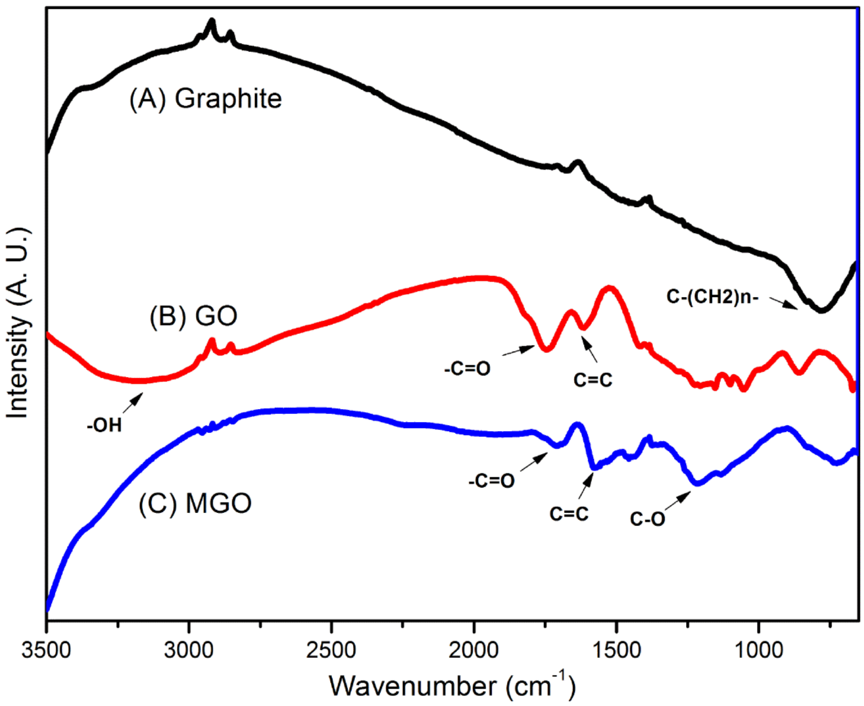

Figure 3-3 FTIR spectra of (a) graphite, (b) GO and (c) MGO.

3.2.4 X-ray Photoelectron Spectroscopy (XPS) analysis

The X-ray Photoelectron Spectroscopy (XPS) spectra of GO, MGO, and MGO with adsorbed selenium are shown in Figure 3-4 . Deconvolution of C1s peak (Figure 3-4 a) of GO indicates that there are four types of C species in graphene oxide, saturated C-C bonding in the graphene framework at 284.6 eV, the carbon linking hydroxyl (C-OH) or epoxy groups (C-O-C) at 286.8 eV, the carbonyl carbon (C=O) at 287.8 eV, and carboxyl carbon (O-C=O) at 288.9 eV. Four similar peaks appear on the C1s spectrum of MGO. The relative intensity of the C-O carbon decreases, mainly due to the breaking of C-O bond and formation of new Fe-O bond. The XPS result also provides evidence of oxygen-containing groups on the GO sheets. In the spectrum of O1s (Figure 3-4 b) in GO, a strong peak appears at 532.5 eV indicating a hydroxyl functional group, which dominates the oxygen containing groups and diminishes other peaks (such as C-O and C=O). Significant difference could be observed in the O1s spectrum of MGO as compared to that of GO show in Figure 3-4. The new peak at 529.9 eV is attributed to the Fe-O bond in iron oxide on MGO. Other new peaks at 533.3 eV and 534.1 eV are attributed to the oxygen in C-O and C=O, respectively. The peak for oxygen in hydroxyl shifts slightly from 532.5 eV to 531.2 eV due to formation of O-Fe bond. The spectra of Fe $2p_{1/2}$ and Fe $2p_{3/2}$ (Figure 3-4 c) demonstrate that there are both magnetic Fe_3O_4 and γ-Fe_2O_3 on MGO; the peaks at 725.4 eV and 712.0 eV belong to Fe_3O_4 while 723.7 eV, 718.8 eV and 710.4 eV belong to Fe_2O_3. Figure 3-4 d shows the Se 3d spectra of MGO after the adsorption of Se (IV) and Se (VI), the peaks of which could be assigned to Se-OH in Se (IV) (58.8 eV) and Se (VI) (59.7 eV), respectively. This result provided evidence that the oxidation state for each selenium species did not change after adsorption.

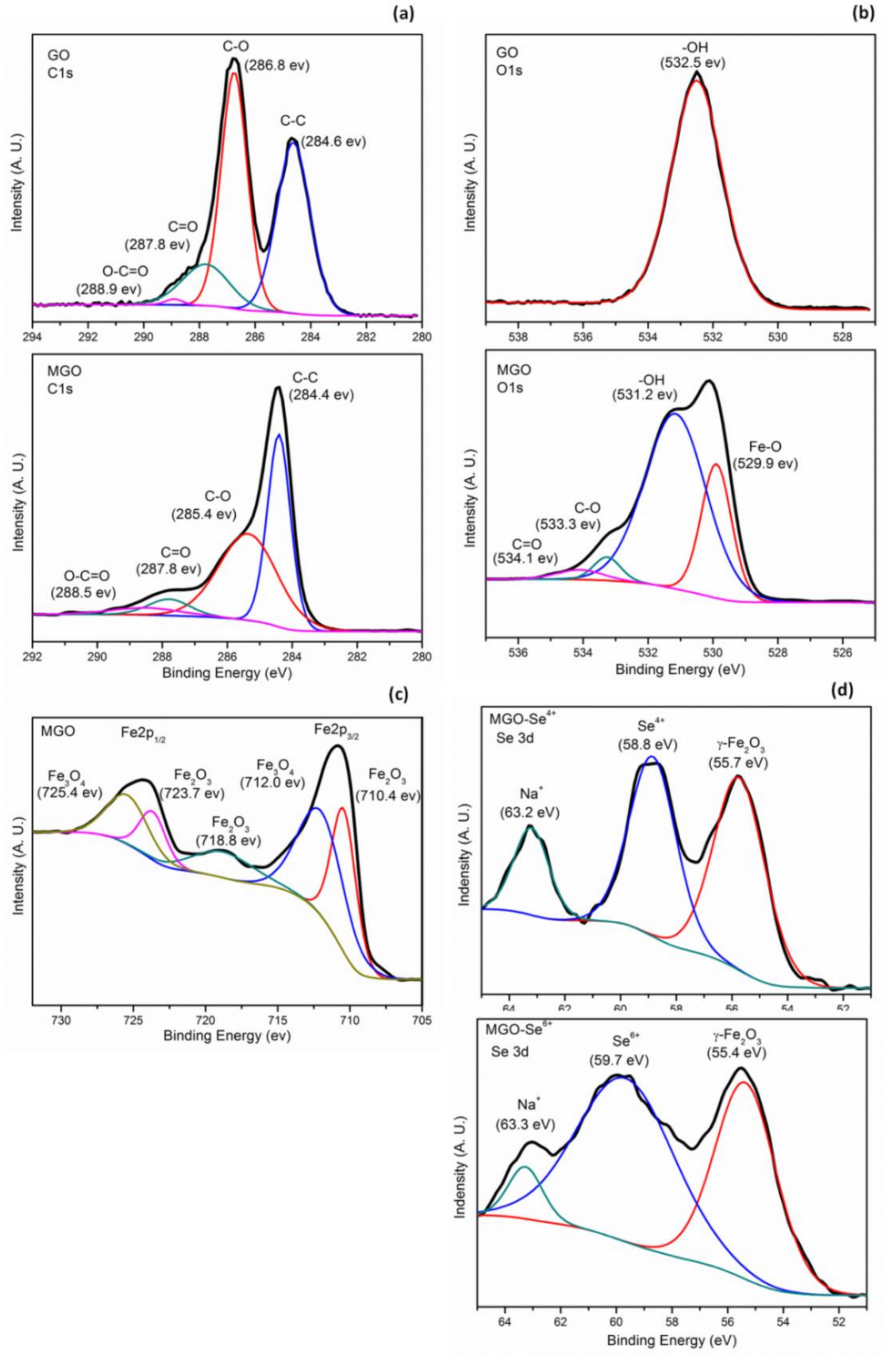

Figure 3-4 XPS patterns of (a) C1s spectra of GO (top) and MGO (bottom), (b) O1s spectra of GO (top) and MGO (bottom); (c) Fe 2p spectra of MGO; (d) Se 3d after Se (IV) (top) and Se (VI) (bottom) adsorption using MGO.

3.2.5 Thermo Gravimetric Analysis (TGA) analysis

The thermo gravimetric analysis (TGA) of graphite, GO and MGO is shown in Figure 3-5. It was found that pristine graphite is extremely stable with only a weight loss of 4.1 % at 1000 ^{o}C. However the thermal stability of GO and MGO decreases dramatically, which is mainly because that the introduction of oxygen-containing groups destroys the original multilayer stack structure of graphite and lower the van der Waals interactions between the different layers. Moreover, the introduced oxygen-containing groups or the carbon bonded to the oxygen-containing groups are easier to be decomposed at high temperature than the carbon in graphite.[25] On the TGA curve of GO, the initial weight loss from ~ 20 ^{o}C to 120 ^{o}C could be due to the loss of physically adsorbed water. The most significant weight loss of GO occurring from ~ 187 ^{o}C to 220 ^{o}C is due to the decomposition of labile hydroxyl, carboxyl and epoxy groups and yielding of CO, CO_2, or steam. The further mass loss of GO from ~ 600 ^{o}C could be due to the pyrolysis of the more stable oxygen containing groups and graphene oxide framework.[32] The total weight loss of GO at 1000 ^{o}C is ~ 84.5 %. The TGA analysis also shows that MGO has better thermal stability than pure GO. The possible reasons include (1) iron oxide could impose a restriction on mobilization of MGO, thus resulting in a more homogeneous heating and avoid the heat concentration;[33] (2) less oxygen-containing groups on MGO sheets; (3) the oxidation of Fe^{2+} would cause weight gain. The MGO loses weight gradually with increasing the temperature with the sharpest drop at around 500 °C, indicating the breakage of Fe-C, Fe-O, and C-C bonding.[25]

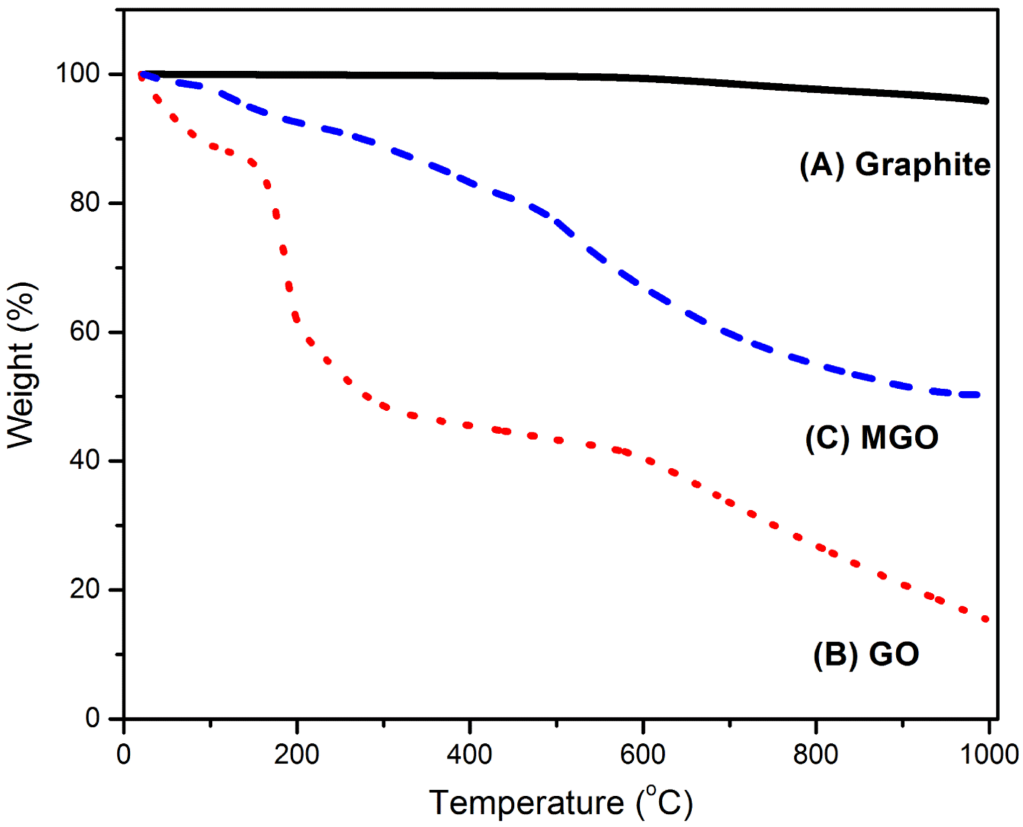

Figure 3-5 TGA curves of (a) Graphite, (b) GO, and (c) MGO.

3.2.6 Characterization by Transmission Electron Microscopy (TEM) and Scanning Electron Microscope (SEM)

The Transmission Electron Microscopy (TEM) image of GO (Figure 3-6 a) shows that the GO possesses a transparent sheet sturcture, consistent with the AFM imaging. The TEM image of the MGO composite (Figure 3-6 b) and the Scanning Electron Microscope (SEM) images of MGO (Figure 3-7) show that magnetic nanoparticles (with an average particle size of ~ 9 nm) are well dispersed on the GO sheets. The Fast Fourier Transformation (FFT) pattern of selected magnetic particle on the HRTEM image (Figure 3-6 c) reveals a structure with lattice spacing of 0.4804 nm (crystal plane (111)), 0.2942 nm (crystal plane (220)) and 0.2509 nm (crystal plane (311)). Indexation of the FFT pattern suggests that the magnetic particle composition corresponds to $Fe_{2.67}O_4$ (cubic, a=b=c=0.8320 nm). Electron Energy Loss Spectroscopy (EELS) (Figure 3-6 d) analysis of iron oxide nanoparticles in MGO reveals an atomic percentage of Fe (17.77 %) and O (82.23 %).

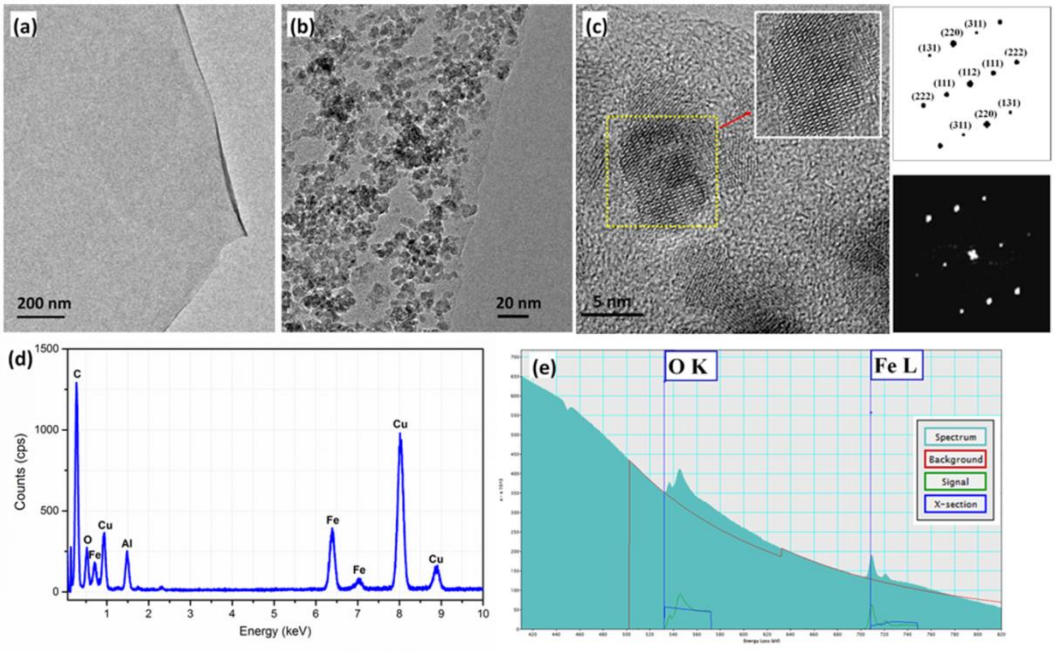

Figure 3-6 TEM images of (a) GO, (b) MGO and (c) HRTEM image and selected area diffraction pattern of single magnetic iron oxide particles, marked by yellow square. The up-right inset is the image of the same iron oxide particle after Wiener Filter processing. The diffractogram of the iron oxide is shown on the bottom right side of the image. Diffraction simulation (on top of the

diffractogram) using Desktop Microscopist suggests this single iron oxide is $Fe_{2.67}O_4$. The orientation of this particle is [-112].; (d) EDS spectrum indicates the presence of elements O, C, and Fe; (e) EELS spectrum of iron oxide nanoparticles in MGO.

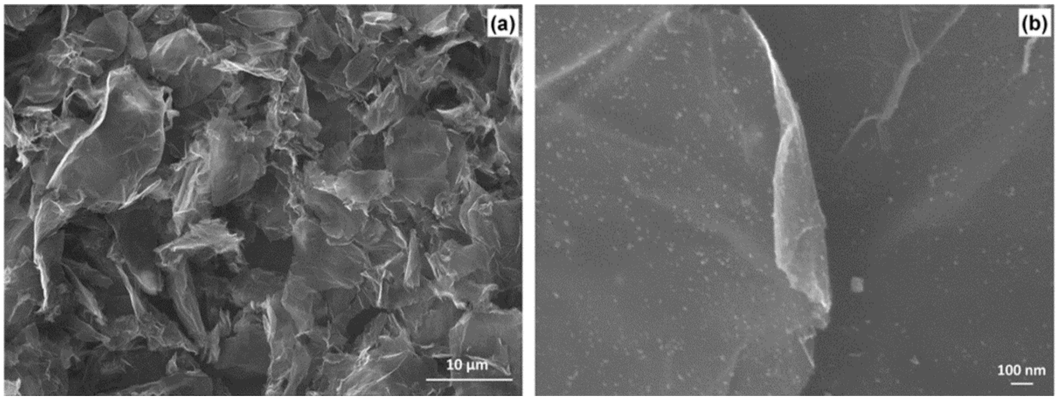

Figure 3-7 SEM images of MGO in (a) low magnification and (b) high magnification.

3.2.7 Magnetic properties of MGO

The magnetization curve of MGO measured at room temperature is shown in Figure 3-8 a, which indicates that the magnetic nanoparticles in MGO exhibit superparamagnetic behavior. The magnetic hysteresis curves show that the magnetic remanence of the MGO sample is 0.20 emu g^{-1} and the specific saturation magnetization (Ms) is 13.47 emu g^{-1} which is higher than the reported Ms values of MGO reported previously[34, 35] but lower than Ms = 92 emu g^{-1} of pure iron oxide nanocrystals[36]. The relatively lower Ms of MGO could be attributed to the rather smaller size and the presence of GO. The strong magnetism of the MGO enables the efficient magnetic separation of the adsorbent materials (within 10 seconds under a small external magnetic field of ~ 50 mT) after adsorption process. Figure 3-8 b shows selenium solution with MGO dispersed; Figure 3-8 c shows the same solution after ~ 10 seconds of magnetic separation.

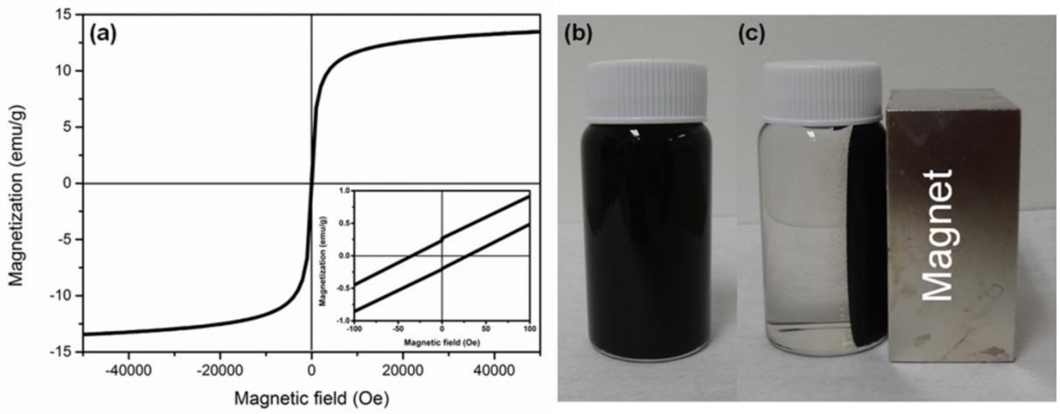

Figure 3-8 (a) Magnetic hysteresis loop of MGO with a bottom right inset of a close view of the hysteresis loop. (b) MGO dispersed in selenium containing solution before magnetic separation and (c) The effect of magnetic separation after about ten seconds.

3.2.8 Possible MGO synthesis and selenium adsorption mechanism

Possible reaction mechanism for MGO synthesis is proposed and shown in Figure 3-9 a, b and c. During the synthesis of MGO, positive Fe^{3+} ions would first attach to GO surfaces via electrostatic attraction and act as nucleation precursors. Fe^{3+} could be partly reduced to Fe^{2+} by the mild reducing agent and solvent

NMP.[37, 38] Similar synthetic route of magnetite nanocrystals were proposed with 2-pyrrolidone as the solvent and reducing agent.[39, 40]

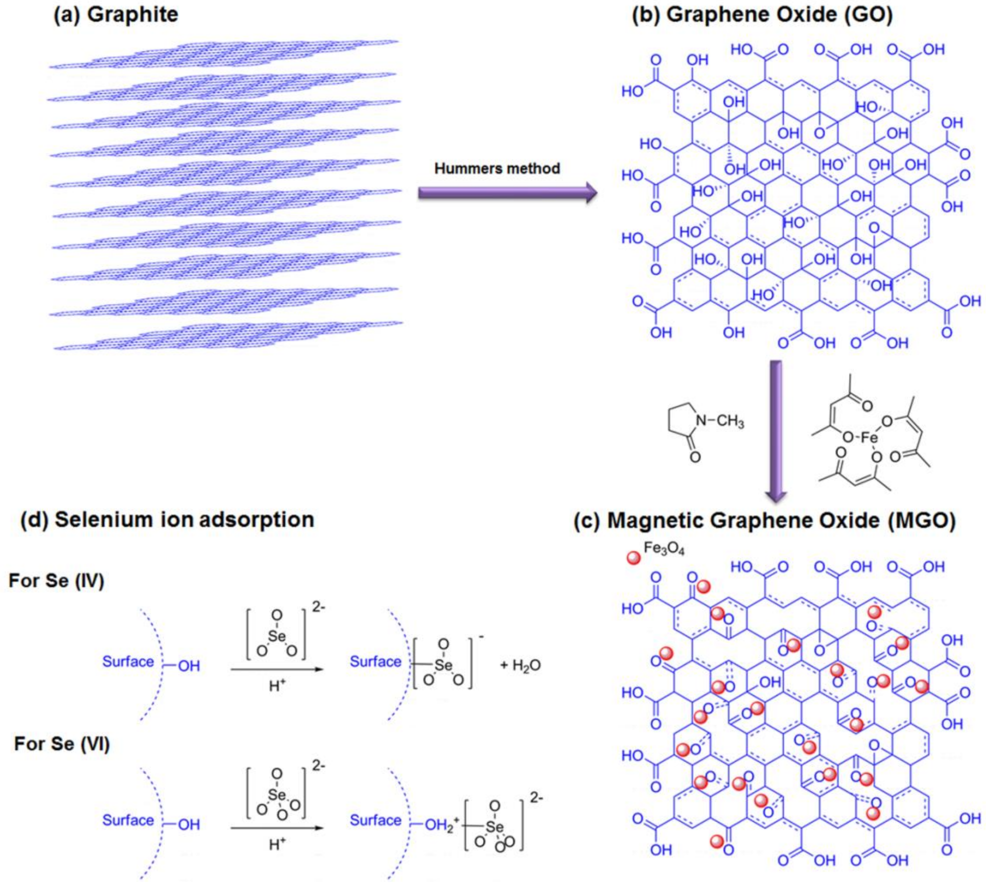

Figure 3-9 MGO synthesis process and possible selenium adsorption mechanism.

3.2.9 Definition of adsorption capacity Q (mg g^{-1}) and removal percentage q (%)

MGO was then applied to test the capability of selenium removal in aqueous solutions with different initial Se (IV) and Se (VI) concentrations (50 ppb to 500 ppm), pH (2 to 11), and adsorption times (10 s to 12 h). The adsorption capacity Q (mg g^{-1}) and removal percentage q (%) are defined in Equations 1 and 2, respectively, where C_0 (ppm) is the initial Se (IV) or Se (VI) concentration, C

(ppm) the equilibrium concentration of Se (IV) or Se (VI), *W* (g) the adsorbent weight, *V* (mL) the total solution volume.

$$Q = \frac{(C_0 - C) \times V}{W} \tag{1}$$

$$q = \frac{C_0 - C}{C_0} \times 100 \tag{2}$$

Figure 3-10 shows the Q-C_0 and q-C_0 curves for the adsorption of Se (IV) and Se (VI) using MGO with a dosage of 1 g L^{-1} under natural pH (~ 6), room temperature (25 ℃) and 300 rpm shaking rate for 24 hours. Figure 3-10 demonstrates that the higher initial concentration of Se (IV) and Se (VI), the stronger the final adsorption capacity is. The Q-C_0 and q-C_0 curves tend to reach a platform that indicates a saturated adsorption capacity.

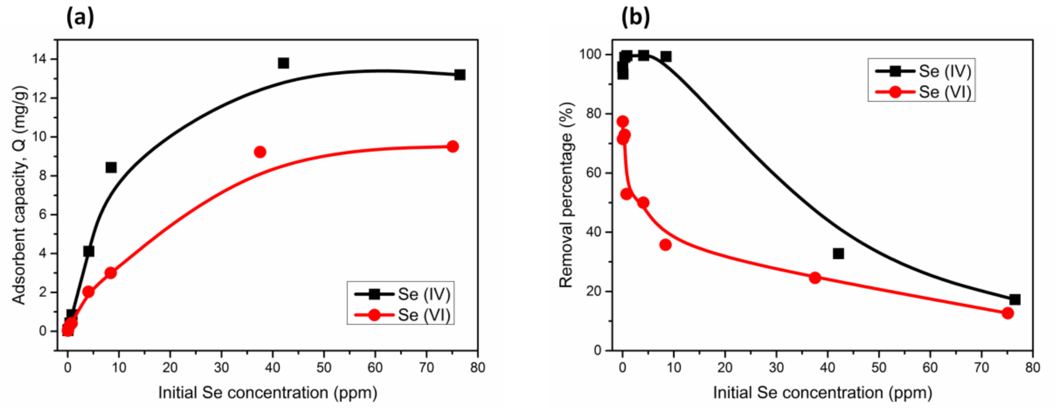

Figure 3-10 (a) Q-C_0 and (b) q-C_0 curves of Se (IV) and Se (VI) adsorption using MGO.

3.2.10 Adsorption curves fitting with Freundlich and Langmuir adsorption Models

Q-*C* curves of Se (IV) and Se (VI) were fitted using both Freundlich and Langmuir adsorption Models (Figure 3-11). At a constant temperature, Freundlich Adsorption Equation[41] is expressed as:

$$Q = K \times C^{n} \tag{3}$$

where K and n are Freundlich Constants. Generally, when n is between 0.1 and 1, the adsorption process is considered as optimal adsorption; while $n > 2$, the adsorption is significantly difficult to occur.[42, 43]

At a constant temperature, Langmuir Adsorption Equation[44] is represented as,

$$Q = \frac{a \times b \times C}{1 + b \times C} \tag{4}$$

where a and b are Langmuir Constants. a (mg g^{-1}) is the saturate adsorption capacity and b (L mg^{-1}) is the constant related to adsorption free energy.

The fitted values of the parameters in the two models are listed in Table 3-1**.** The n values in Freundlich Adsorption Equation for both Se (IV) and Se (VI) equations are less than 1, indicating optimal adsorption for both processes.[42, 43] The Fitting results that although both models could describe Se (IV) and Se (VI) adsorption by MGO reasonably well, the Langmuir Model seems to provide a better fitting for both Se (IV) and Se (VI) adsorption with higher R^2 values (coefficient of determination). Thus the adsorption process is most likely a monolayer adsorption through strong chemical bonding on special adsorbing sites, which are believed to be hydroxyl functional groups (discussed later).

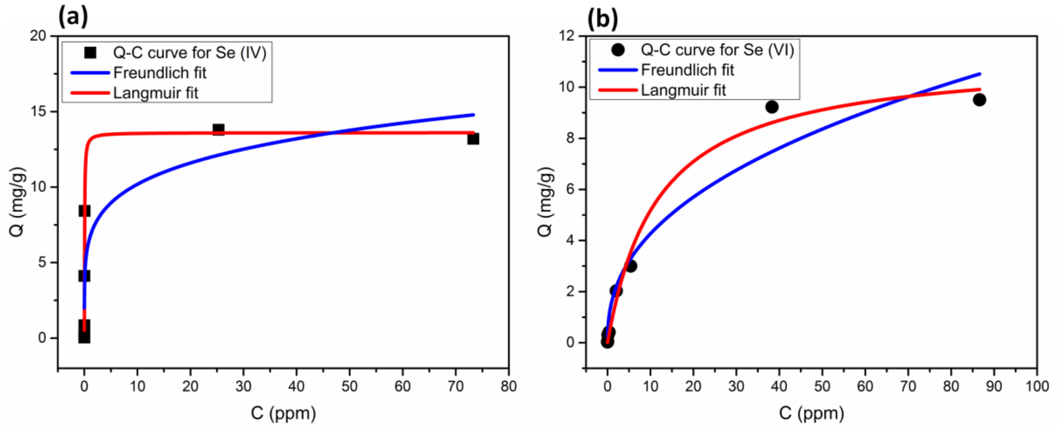

Figure 3-11 Fitting curves using Freundlich and Langmuir Models under different (a) Se (IV) and (b) Se (VI) equilibrium concentrations.

Isotherm type	Isotherm constants	Se (IV)	Se (VI)
Freundlich	K	6.632	1.632
	n	0.187	0.418
	R_F^2	0.794	0.950
Langmuir	a [mg g^{-1}]	13.611	11.253
	b [L mg^{-1}]	24.666	0.085
	R_L^2	0.978	0.990

Table 3-1 Freundlich and Langmuir adsorption isotherm parameters for adsorption of Se (IV) and Se (VI) ions on MGO.

3.2.11 Effect of pH value on selenium adsorption

The effects of pH and adsorption time on the adsorption of Se (IV) and Se (VI) were investigated at room temperature, with a fixed MGO dosage of 1 g L^{-1}

and a shaking rate of 300 rpm, as shown in Figure 3-12. The removal percentage of Se (IV) remains almost 100 % for pH < 10 and then drastically drops at pH = 11, while the removal percentage of Se (VI) gradually decreases with increasing pH, which indicates that lower pH facilitates the adsorption of both Se (IV) and Se (VI) on MGO. The more significant pH impact on the adsorption of Se (VI) than Se (IV) implies their different adsorption mechanisms on MGO.

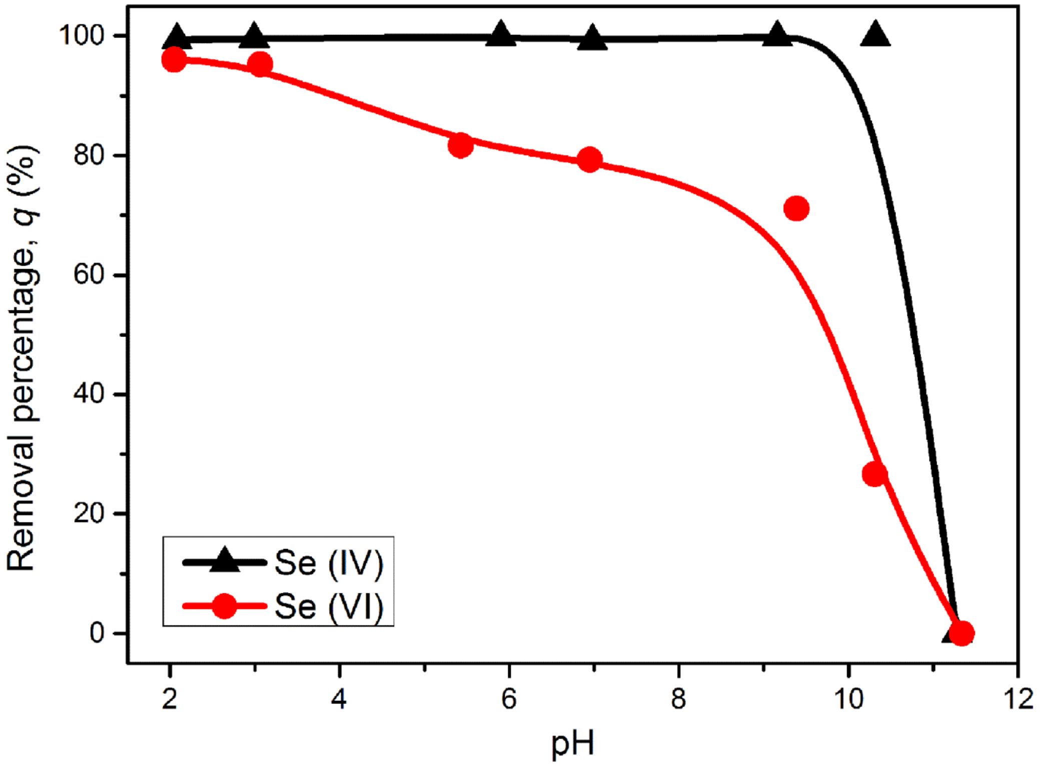

Figure 3-12 Effect of pH on selenium adsorption, at room temperature (25 ℃), with an adsorption time of 2 h, MGO dosage 1 g L^{-1}, and initial selenium concentration 300 ppb.

3.2.12 Kinetics of selenium adsorption on MGO

The effect of adsorption time is shown in Figure 3-13, indicating that the adsorption of Se (IV) and Se (VI) on MGO occurs almost instantaneously and can be completed in less than 10 seconds. Such a highly efficient adsorption percentage with MGO is much higher than the previous studies of Se (IV) and Se (VI) adsorption with hematite (~ 5 hours),[23] magnetite (~ 30 hours),[19] goethite (~ 50 hours),[22] Fe_3O_4 (10 min) and Fe/Fe_3C nanoparticles (30 min).[45]

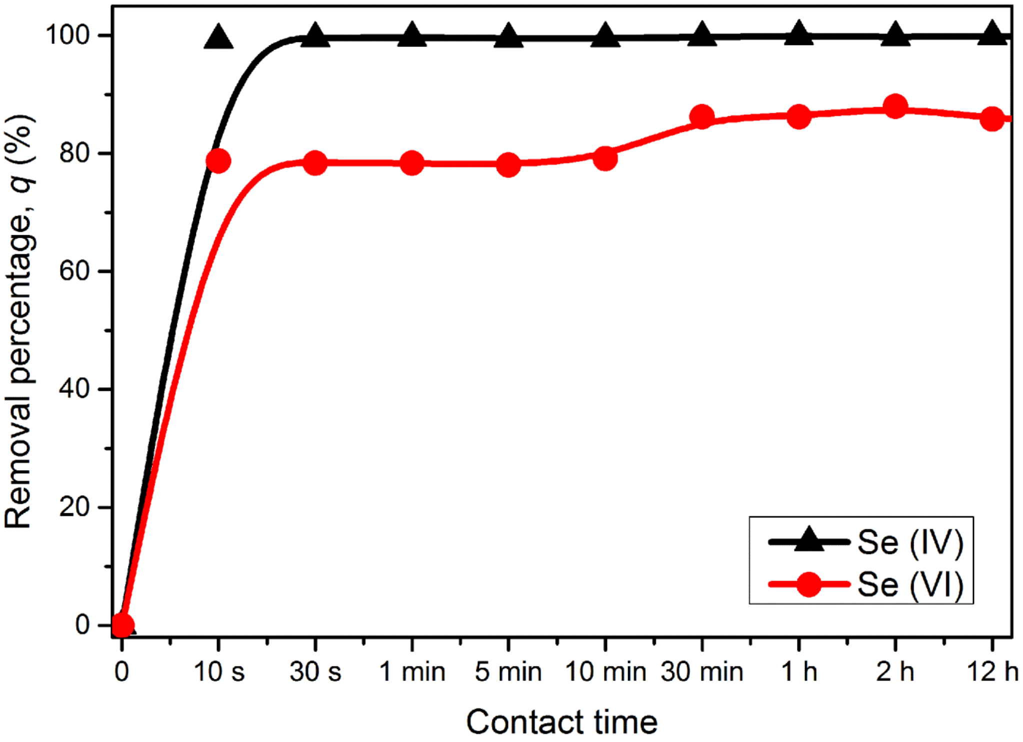

Figure 3-13 Effect of adsorption time on selenium adsorption, at room temperature (25 ℃), pH ~ 6, MGO dosage 1 g L^{-1}, and initial selenium concentration 300 ppb.

3.2.13 Discussion of possible selenium adsorption mechanism

It is evident from the above results that MGO has unique adsorption capability of both Se (IV) and Se (VI), which is attributed to its surface properties and functional groups. Iron oxide is believed to play an important role in the adsorption of Se, and its adsorption mechanism of Se (IV) and Se (VI) was proposed in previous studies.[6-9, 11, 19-23, 45-48] Hayes et al.[8] conducted in situ Extended X-ray Absorption Fine Structure (EXAFS) measurements on the adsorption of Se (IV) and Se (VI) at α-FeOOH (goethite)-water interface and suggested that Se (IV) would form a strongly bonded, inner-sphere bidentate complex, while Se (VI) would form a weakly bonded, outer-sphere monodentate hydrated complex.

MGO contains at least two types of hydroxyl binding sites located on iron oxide (≡Fe-OH) and on graphene oxide sheets (≡C-OH), respectively. Accordingly, these hydroxyl binding sites could interact with the adsorbed Se (IV) and Se (VI) on MGO as illustrated in Scheme 1d.

Se (IV), a strongly binding anion,[21, 47-49] can adsorb on iron oxides by a aqueous ligand exchanging for the surface hydroxyl group to form an inner-sphere complex, as shown in Equation 5.

$$\text{MGO-OH} + \text{SeO}_3^{2-} + \text{H}^+ \rightarrow \text{MGO-SeO}_3^{-} + \text{H}_2\text{O} \qquad (5)$$

Different from Se (IV), Se (VI) is a relatively weak binding anion and can only be adsorbed to MGO surface through electrostatic attraction to form an outer-sphere complex with one water molecule between MGO surface site and Se (VI) ligand,[8, 49] as shown in Equation 6.

$$\text{MGO-OH} + \text{SeO}_4^{2-} + \text{H}^+ \rightarrow \text{MGO-OH}_2^{+}\text{-SeO}_4^{2-} \qquad (6)$$

Although the outer-sphere complex itself is less stable than inner-sphere complex, it is speculated that the conjugated π bond of partially reduced graphene oxide can enhance the stability of outer-sphere complex.[50] Besides, the interaction between MGO and H_2O could be enhanced due to the hydrophilic nature of graphene oxide. The relatively stable outer-sphere complex on MGO thus leads to high adsorption percentage of Se (VI).

3.2.14 Comparison between MGO, GO and pure Fe_3O_4 particles (400 nm and 10 - 20 nm) for adsorption of selenite and selenate ions at different concentrations.

Figure 3-14 a and Figure 3-14 b depict the removal percentage of Se (IV) and Se (VI) of different initial concentrations, respectively, by using GO, MGO and pure Fe_3O_4 particles (two different sizes: 400 nm and 10 - 20 nm in diameter). In Figure 3-14 a, both MGO and Fe_3O_4 (10 - 20 nm) show strong adsorption capability of Se (IV) with a removal percentage higher than 90 % under the initial Se (IV) concentration range tested (C_0: 0 - 10 ppm). In contrast, Fe_3O_4 particles (400 nm) show much weaker adsorption ability of Se (IV) with a removal percentage of ~ 20 % at low Se (IV) concentration (e.g. 100 ppb) which drops to almost zero at $C_0 = 10$ ppm. The results in Figure 3-14 a indicate that the presence of magnetic nanoparticles on MGO play a critical role in its efficient removal of

Se (IV), which shows similar adsorption mechanism as that of Fe_3O_4 nanoparticles. The smaller the particle size, the higher the specific surface area, which could dramatically increase the number of adsorption sites to enhance its removal efficiency of Se (IV). GO shows around 20 % removal percentage for Se (IV).

In Figure 3-14 b, MGO shows the overall highest removal percentage for Se (VI). The removal percentage for Se (VI) using Fe_3O_4 (10 - 20 nm) decreases significantly with increasing Se (VI) concentration, and shows a much lower removal percentage (< 20 %) at $C_0 = 10$ ppm for Se (VI), as compared with the Se (IV) removal case. Fe_3O_4 (400 nm) shows negligible removal capability for Se (VI). The removal percentage for Se (VI) using GO increases with increasing Se (VI) concentration, and reaches ~ 30 % at $C_0 = 10$ ppm. The higher Se (VI) removal capability of MGO than that of pure Fe_3O_4 nanoparticles (10 - 20 nm) indicates that MGO has higher affinity to Se (VI) than Fe_3O_4 particles and graphene oxide plays a significant role. It is speculated that the hydroxyl groups located on GO could act as active adsorption sites and the conjugated π bond of partly reduced graphene oxide could enhance the stability of outer-sphere complex.[50]

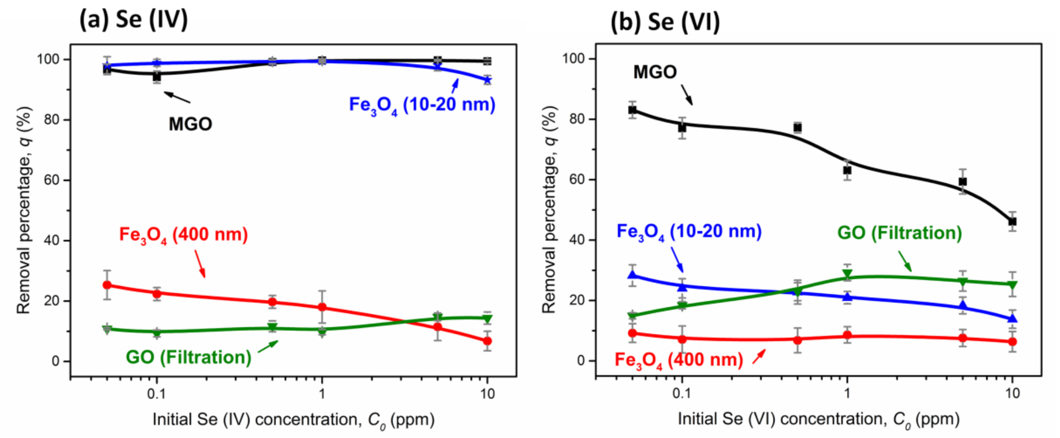

Figure 3-14 Comparison between MGO, GO and pure Fe_3O_4 particles (400 nm and 10 - 20 nm) for adsorption of (a) Se (IV) and (b) Se (VI) ions at different concentrations.

The proposed adsorption mechanism above shows that the formation of both inner-sphere and outer-sphere consumes H^+ during the adsorption of Se (IV) and Se (VI) on MGO. It is expected that lower pH could facilitate the adsorption process by MGO, in accordance with the pH effect results shown in Figure 3-12.

3.2.15 MGO recycling tests

One of the advantages of the MGO adsorbent materials is that it allows fast separation by an external magnetic field after the adsorption process, which can be recycled to desorb the Se (IV) and Se (VI) for reuse in water treatment. To evaluate the regeneration capability of the MGO sorbents, Se (IV) or Se (VI) was desorbed by washing MGO using NaOH (0.1 N, pH ~ 13), and the MGO was then reactivated in HCl (0.001 N, pH ~ 3). The recycled MGO was applied again for Se removal in 300 ppb Se (IV) or Se (VI) solution under room temperature, with constant shaking of 300 rpm for 24 hours. The normalized selenium removal percentage using recycled MGO remains almost 100 % after 10 cycles, as shown in Figure 3-15 (note the selenium removal percentage values of recycled MGO were normalized by the initial removal percentage).

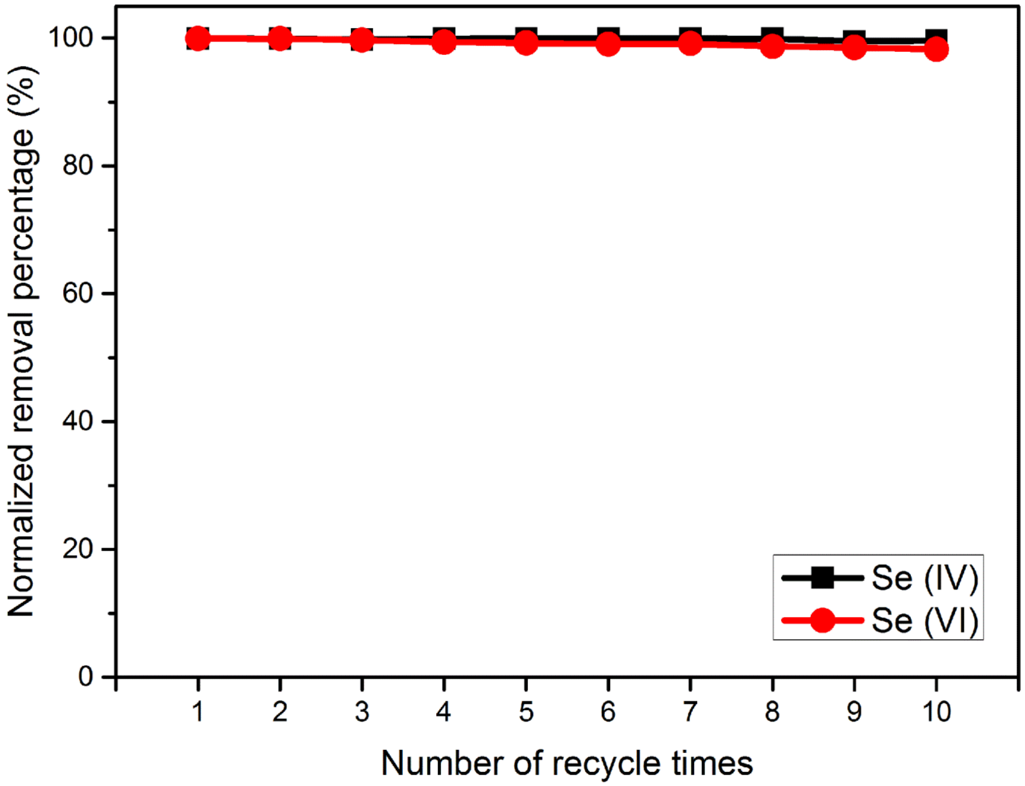

Figure 3-15 Normalized selenium removal percentage using MGO with different recycle times. Recycle was done using standard acid-base method. Tests were done at room temperature (25 ℃), pH ~ 6, with MGO dosage 1 g L^{-1}, and initial selenium concentration 300 ppb.

3.3 Conclusions

To remove the toxic Selenium ions in water, a water-soluble MGO composite adsorbent was synthesized by a two-step reaction: oxidation of graphite to graphene oxide based on the Hummer method and deposition of magnetic iron oxide nanoparticles on GO sheets through a high temperature solvent reaction. XRD, HR-TEM and FTIR characterizations confirm the chemical composition and structure of MGO and that magnetic nanoparticles (with an average particle size of ~ 9 nm) are well dispersed on the GO sheets. The MGO composites show efficient and high binding capacity for Se (IV) and Se (VI), with removal percentage for selenite (> 99.9 %) and selenate (~ 80 %) within a few seconds. Acidic pH enhances the adsorption of Selenium ions on MGO, and the removal percentage of Se (VI) increases to > 95 % at pH ~ 2. Our results show that MGO composites have excellent removal capability of selenite and selenate in aqueous solutions which can be used for practical applications in removal of selenium ions.

3.4 Experimental Section

3.4.1 Chemicals and Materials

Natural graphite (7 - 10 micron), potassium permanganate ($KMnO_4$), sodium nitrate ($NaNO_3$), H_2O_2 (30 wt%) were purchased from Alfa Aesar. 1-methyl-2-pyrrolidone (NMP), ferric acetylacetonate ($Fe(acac)_3$), H_2SO_4 (98 %), HCl (0.001N), NaOH (0.1 N) and acetone were purchased from Fisher Scientific

Company, Canada. Milli-Q water was used in all processes of aqueous solution preparation and lavation.

3.4.2 Synthesis of GO

Graphite oxide was prepared by a modified Hummers method.[51] Firstly, natural graphite flake (7 - 10 micron, 2g) and sodium nitrate (1.5 g) were mixed in a three necked flask in an ice-bath. Sulfuric acid (98 %, 150 mL) was then added to the mixture while a mechanical agitation and the ice-bath were maintained. Secondly, potassium permanganate (9 g) was slowly added into the mixture and the stirring was kept in ice-bath for another 2 hours before the ice-bath was taken away. After another 5 days stirring at room temperature, a portion of H_2O_2 (6 mL) was added into the mixture to neutralize the unreacted $KMnO_4$. A solution (250 mL) mixed with H_2SO_4 (98 %, 7.5 mL), H_2O_2 (30 wt%, 4.17 mL) and Milli-Q water was further added into the obtained bright yellow suspension while the mechanical stirring maintained. Then sediment was washed repeatedly using Milli-Q until neutral pH, followed by another 5 days of dialysis to remove the remnant soluble ions. The obtained sediment is graphite oxide. After the ultrasonic treatment, the as-synthesized graphite oxide could be further exfoliated to graphene oxide. Freeze-drying was applied to obtain fluffy golden flocci dried GO product.

3.4.3 Preparation of MGO

A modified synthesis method based on a reported approach by Shen was applied.[25] GO (100 mg) was dispersed in 1-methyl-2pyrrolidone (NMP, 30mL) by ultrasonication at room temperature. Then the mixture was heated to 190 ℃ under the nitrogen atmosphere. Fe(acac)$_3$ (1.413 g, 4 mmol) was dissolved in NMP (20mL) and added dropwise for about 1 hour to the GO/ NMP solution under vigorous stirring. The stirring was continued for another 4 hour after the dropping was finished. The above procedure could increase the magnetism of the composite as compared to the previous method reported.[25] After cooling down to room temperature, the mixture was washed several times by acetone and water alternatively. The precipitate was collected by magnetic separation and was then dispersed in water using sonication. The resulting black powder was collected by freeze-drying process.

3.4.4 Adsorption experiment

The adsorbent MGO (20 mg, dosage 1 g L^{-1}) was added into Se (IV) or Se (VI) solution (20 mL, prepared from diluting 1000 ppm Na_2SeO_3 or Na_2SeO_4 stock water solutions), and mixed uniformly by shaking at 300 rpm at room temperature (25 ℃). NaOH and HCl were used to adjust the pH. After, the adsorption process, MGO was separated from solutions by simply applying a hand magnet beside the sample bottle (Figure 3-8 b and c). The supernatant was then collected for further ICP-MS analysis to determine the selenium concentration after adsorption.

3.4.5 Characterization Methods

Atomic Force Microscope (AFM) imaging was conducted using an Asylum MFP-3D system in tapping mode. AFM samples were prepared by dropping ultrasonic treated GO water solution on the freshly cleaved mica surface, followed by overnight drying. X-Ray Diffraction (XRD) was conducted on a RIGAKU Rotating anode XRD system with a copper anode, 40 kv, 2 degs minute^{-1}. Fourier Transform Infrared Spectroscopy (FTIR) spectra were recorded on a Varian FTS 7000 FT-IR Imaging System. X-ray Photoelectron Spectroscopy analysis (XPS) was conducted using an AXIS 165, XPS Spectrometer. Thermo Gravimetric Analysis (TGA) was carried out with a TA Instrument Q-500 TGA instrument, with a heating rate of 10 ^{o}C min^{-1} and nitrogen as the purge gas. Before the tests, all the samples were carefully ground to powders to ensure sufficient diffusion of heat. The measurements were conducted using ~ 10 mg samples, and weight retention/temperature curves were recorded. Morphology of GO and MGO was characterized by Transmission Electron Microscopy (TEM) using a Hitachi HF 3300 Mode and a Vega-3 (Tescan) Scanning Electron Microscope (SEM). TEM samples were prepared by pipetting several microliters of GO and MGO dispersion onto lacey carbon coated copper grids and dried. A Quantum Design 9T-PPMS magnetometer was used to record the magnetic hysteresis curve. A Perkin Elmer's Elan 6000 Inductively Coupled Plasma-Mass Spectrometry (ICP-MS) was used to test the selenium concentration at ppb level.

3.5 Acknowledgements

This work was supported by the Natural Sciences and Engineering Research Council of Canada (NSERC) and Canada Foundation for Innovation (CFI).

3.6 References

[1] L. Schomburg, U. Schweizer, J. Köhrle, Selenium and selenoproteins in mammals: extraordinary, essential, enigmatic. *Cellular and Molecular Life Sciences CMLS*. **2004**, *61*, 1988.

[2] W. H. Organization, Guidelines for Drinking-water Quality. **2011**.

[3] F. M. Fordyce, *Selenium deficiency and toxicity in the environment*, Springer, **2013**.

[4] US-EPA, National Primary Drinking Water Regulations. **2009**.

[5] L. Twidwell, "The Removal of Arsenic, Selenium and Metals from Aqueous Solution by Iron Precipitation and Reduction Techniques", presented at *TMS2011 Annual Meeting, San Diego, CA*, 2011.

[6] L. S. Balistrieri, T. Chao, Adsorption of selenium by amorphous iron oxyhydroxide and manganese dioxide. *Geochimica et Cosmochimica Acta*. **1990**, *54*, 739.

[7] L. S. Balistrieri, T. Chao, Selenium adsorption by goethite. *Soil Science Society of America Journal*. **1987**, *51*, 1145.

[8] K. F. Hayes, A. L. Roe, G. E. BROWN JR, K. O. Hodgson, J. O. Leckie, G. A. Parks, In situ X-ray absorption study of surface complexes: Selenium oxyanions on α-FeOOH. *Science*. **1987**, *238*, 783.

[9] K. Hayes, J. Leckie, Modeling ionic strength effects on cation adsorption at hydrous oxide/solution interfaces. *Journal of Colloid and Interface Science*. **1987**, *115*, 564.

[10] S.-L. Lo, T.-Y. Chen, Adsorption of Se (IV) and Se (VI) on an iron-coated sand from water. *Chemosphere*. **1997**, *35*, 919.

[11] P. Zhang, D. L. Sparks, Kinetics of selenate and selenite adsorption/desorption at the goethite/water interface. *Environmental science & technology*. **1990**, *24*, 1848.

[12] K. C. Kemp, H. Seema, M. Saleh, K. Mahesh, V. Chandra, K. S. Kim, Environmental applications using graphene composites: water remediation and gas adsorption. *Nanoscale*. **2013**.

[13] V. Chandra, J. Park, Y. Chun, J. W. Lee, I.-C. Hwang, K. S. Kim, Water-dispersible magnetite-reduced graphene oxide composites for arsenic removal. *ACS nano*. **2010**, *4*, 3979.

[14] A. Y. Romanchuk, A. S. Slesarev, S. N. Kalmykov, D. V. Kosynkin, J. M. Tour, Graphene oxide for effective radionuclide removal. *Physical Chemistry Chemical Physics*. **2013**, *15*, 2321.

[15] Z. Niu, J. Chen, H. H. Hng, J. Ma, X. Chen, A leavening strategy to prepare reduced graphene oxide foams. *Advanced Materials*. **2012**, *24*, 4144.

[16] F. Liu, S. Chung, G. Oh, T. S. Seo, Three-dimensional graphene oxide nanostructure for fast and efficient water-soluble dye removal. *ACS Applied Materials & Interfaces*. **2012**, *4*, 922.

[17] M. Z. Iqbal, A. A. Abdala, Oil spill cleanup using graphene. *Environmental Science and Pollution Research*. **2012**, 1.

[18] F. Ahme, D. F. Rodrigues, Investigation of acute effects of graphene oxide on wastewater microbial community: A case study. *Journal of hazardous materials*. **2013**.

[19] M. Martinez, J. Gimenez, J. De Pablo, M. Rovira, L. Duro, Sorption of selenium (IV) and selenium (VI) onto magnetite. *Applied surface science*. **2006**, *252*, 3767.

[20] M. Duc, G. Lefevre, M. Fedoroff, J. Jeanjean, J. Rouchaud, F. Monteil-Rivera, J. Dumonceau, S. Milonjic, Sorption of selenium anionic species on apatites and iron oxides from aqueous solutions. *Journal of environmental radioactivity*. **2003**, *70*, 61.

[21] R. Parfitt, J. Russell, Adsorption on hydrous oxides. IV. Mechanisms of adsorption of various ions on goethite. *Journal of Soil Science*. **1977**, *28*, 297.

[22] M. Rovira, J. Giménez, M. Martínez, X. Martínez-Lladó, J. de Pablo, V. Marti, L. Duro, Sorption of selenium (IV) and selenium (VI) onto natural iron oxides: goethite and hematite. *Journal of hazardous materials*. **2008**, *150*, 279.

[23] M. Duc, G. Lefevre, M. Fédoroff, Sorption of selenite ions on hematite. *Journal of colloid and interface science*. **2006**, *298*, 556.

[24] S.-M. Paek, E. Yoo, I. Honma, Enhanced cyclic performance and lithium storage capacity of SnO2/graphene nanoporous electrodes with three-dimensionally delaminated flexible structure. *Nano Letters*. **2008**, *9*, 72.

[25] J. Shen, Y. Hu, M. Shi, N. Li, H. Ma, M. Ye, One Step Synthesis of Graphene Oxide− Magnetic Nanoparticle Composite. *The Journal of Physical Chemistry C*. **2010**, *114*, 1498.

[26] S. Stankovich, D. A. Dikin, R. D. Piner, K. A. Kohlhaas, A. Kleinhammes, Y. Jia, Y. Wu, S. T. Nguyen, R. S. Ruoff, Synthesis of graphene-based nanosheets via chemical reduction of exfoliated graphite oxide. *Carbon*. **2007**, *45*, 1558.

[27] R. Anthony, John Wiley & Sons, **1984**.

[28] C. Hontoria-Lucas, A. Lopez-Peinado, J. d. D. López-González, M. Rojas-Cervantes, R. Martin-Aranda, Study of oxygen-containing groups in a series of graphite oxides: physical and chemical characterization. *Carbon*. **1995**, *33*, 1585.

[29] H. He, T. Riedl, A. Lerf, J. Klinowski, Solid-state NMR studies of the structure of graphite oxide. *The Journal of Physical Chemistry*. **1996**, *100*, 19954.

[30] A. Lerf, H. He, M. Forster, J. Klinowski, Structure of graphite oxide revisited. *The Journal of Physical Chemistry B*. **1998**, *102*, 4477.

[31] H. He, J. Klinowski, M. Forster, A. Lerf, A new structural model for graphite oxide. *Chemical physics letters*. **1998**, *287*, 53.

[32] Y. Xue, H. Chen, D. Yu, S. Wang, M. Yardeni, Q. Dai, M. Guo, Y. Liu, F. Lu, J. Qu, Oxidizing metal ions with graphene oxide: the in situ formation of magnetic nanoparticles on self-reduced graphene sheets for multifunctional applications. *Chemical Communications*. **2011**, *47*, 11689.

[33] J. Shen, M. Shi, H. Ma, B. Yan, N. Li, M. Ye, Hydrothermal synthesis of magnetic reduced graphene oxide sheets. *Materials Research Bulletin*. **2011**, *46*, 2077.

[34] F. He, J. Fan, D. Ma, L. Zhang, C. Leung, H. L. Chan, The attachment of Fe3O4 nanoparticles to graphene oxide by covalent bonding. *Carbon*. **2010**, *48*, 3139.

[35] X. Yang, X. Zhang, Y. Ma, Y. Huang, Y. Wang, Y. Chen, Superparamagnetic graphene oxide–Fe3O4 nanoparticles hybrid for controlled targeted drug carriers. *Journal of Materials Chemistry*. **2009**, *19*, 2710.

[36] H. Deng, X. Li, Q. Peng, X. Wang, J. Chen, Y. Li, Monodisperse Magnetic Single ‐ Crystal Ferrite Microspheres. *Angewandte Chemie*. **2005**, *117*, 2842.

[37] A. Jouyban, M. A. A. Fakhree, A. Shayanfar, Review of pharmaceutical applications of N-methyl-2-pyrrolidone. *Journal of Pharmacy & Pharmaceutical Sciences*. **2010**, *13*, 524.

[38] S.-H. Jeon, P. Xu, N. H. Mack, L. Y. Chiang, L. Brown, H.-L. Wang, Understanding and controlled growth of silver nanoparticles using oxidized N-methyl-pyrrolidone as a reducing agent. *The Journal of Physical Chemistry C*. **2009**, *114*, 36.

[39] Z. Li, H. Chen, H. Bao, M. Gao, One-pot reaction to synthesize water-soluble magnetite nanocrystals. *Chemistry of materials*. **2004**, *16*, 1391.

[40] Z. Li, Q. Sun, M. Gao, Preparation of water ‐ soluble magnetite nanocrystals from hydrated ferric salts in 2 ‐ pyrrolidone: mechanism leading to Fe3O4. *Angewandte Chemie International Edition*. **2005**, *44*, 123.

[41] H. Freundlich, Über die adsorption in lösungen. *Engelmann, Leipzig*. **1906**.

[42] N. Ahalya, R. Kanamadi, T. Ramachandra, Biosorption of chromium (VI) from aqueous solutions by the husk of Bengal gram (Cicer arientinum). *Electronic Journal of Biotechnology*. **2005**, *8*, 0.

[43] K. a. N. KADIRVELU, C., Agricultural by-products as metal adsorbents: sorption of lead (II) from aqueous solutions onto coir-pith carbon. *Environmental Technology*. **2000**, *21*, 1091.

[44] I. Langmuir, THE CONSTITUTION AND FUNDAMENTAL PROPERTIES OF SOLIDS AND LIQUIDS. PART I. SOLIDS. *Journal of the American Chemical Society*. **1916**, *38*, 2221.

[45] R. López de Arroyabe Loyo, S. I. Nikitenko, A. C. Scheinost, M. Simonoff, Immobilization of selenite on Fe3O4 and Fe/Fe3C ultrasmall particles. *Environmental science & technology*. **2008**, *42*, 2451.

[46] D. Peak, D. Sparks, Mechanisms of selenate adsorption on iron oxides and hydroxides. *Environmental science & technology*. **2002**, *36*, 1460.

[47] D. Yates, T. Healy, Mechanism of anion adsorption at the ferric and chromic oxide/water interfaces. *Journal of Colloid and Interface Science*. **1975**, *52*, 222.

[48] R. Cornell, P. Schindler, Infrared study of the adsorption of hydroxycarboxylic acids onα-FeOOH and amorphous Fe (III) hydroxide. *Colloid and Polymer Science*. **1980**, *258*, 1171.

[49] J. B. Harrison, V. E. Berkheiser, Anion interactions with freshly prepared hydrous iron oxides. *Clays Clay Miner*. **1982**, *30*, 97.

[50] D. R. Eaton, Outer sphere complexes as intermediates in coordination chemistry. *Reviews of chemical intermediates*. **1988**, *9*, 201.

[51] W. Lv, D.-M. Tang, Y.-B. He, C.-H. You, Z.-Q. Shi, X.-C. Chen, C.-M. Chen, P.-X. Hou, C. Liu, Q.-H. Yang, Low-temperature exfoliated graphenes: vacuum-promoted exfoliation and electrochemical energy storage. *Acs Nano*. **2009**, *3*, 3730.

Chapter 4 Removal of High-Valence Selenium Ion with Water-Dispersible Magnetic Particle-Graphene Oxide Composites Reduced by Ethylene Glycol [7]

4.1 Introduction

Selenium is a metalloid element, which has the narrowest ranges between dietary deficiency (< 40 μg day^{-1}) and toxic levels (> 400 μg day^{-1}).[1] One of the isotopes, ^{79}Se is a long-lived radionuclide (half-life: 6.5×10^4 years), which could be released from nuclear fuel waste depositories through underground water and cause cumulative radioactivity within biosphere.[2] During mining and mineral processing, selenium can be released into waster and soils, and then further transfer to the plants, animal organism and life cycles, resulting in serious health and environmental issues. It has been estimated that 76,000–88,000 tons year^{-1} of selenium are released globally from anthropogenic activity.[3] Thus it is crucial to characterize selenium distribution in the environment and control selenium content in aqueous environment, soils and atmosphere. The World Health Organization (WHO) currently set 40 ppb (40 μg L^{-1}) selenium as the Maximum Acceptable Concentration (MAC) for drinking water.[1]

Selenium exists in the environment with chemical forms of: selenide (Se^{2-}), amorphous or polymeric elemental selenium (Se^0), selenite (SeO_3^{2-}), selenate (SeO_4^{2-}), and organic Se. Among all the oxidative states, selenate and selenite are

---

[7] A version of this chapter has been submitted for publication. Y. Fu, J. Wang, Q. Liu, H. Zeng 2013. Environmental & Energy Science (under review).

more mobile and toxic. Selenate is more water soluble than selenite and more bioavailable,[3] which makes selenate the major harmful selenium species in aqueous system. However, most of the commercial adsorbents, including activated carbon, silica gel, clay, molecular sieve, ferric oxyhydroxide, and activated aluminium oxide, only have certain adsorption capacity of selenite but show very poor performances in selenate removal.[4] Thus, there is an urgent need to develop an efficient adsorbent for the removal of water-borne high valence selenium (i. e. both selenite and selenate).

Graphene oxide (GO)/graphene based adsorbents demonstrate promising removal ability in heavy metal ions,[5] anions,[6] radionuclide,[7] organic contaminations,[8, 9] oil spill-ups,[10] and microbial community[11] because of their high specific surface area, easy surface functionalization, and abundant surface hydroxyl and carboxyl functional groups. Surface hydroxyl groups are considered to be crucial for the adsorption of high-valence selenium oxyanions and formation of inner/outer-sphere complex. There is no report on the removal of selenium ions using GO/graphene based adsorbents. Our preliminary selenium adsorption experiments with GO show its potential removal ability. However, it is very difficult to separate GO-Se compound from water after adsorption, due to the hydrophilicity nature of GO. To separate the adsorbent effectively, magnetic iron oxide particles could be deposited on GO platelets, which allows the adsorbent to be recycled under an external magnetic field. Additionally, it has been reported that iron oxides ores, such as magnetite,[12] goethite,[2, 13-16] and hematite[2, 17] could be used in the application of selenite removal. When dispersed in water, iron oxide hydrolyses which generates hydroxyl groups. In high valence selenium oxyanions adsorption, hydroxyl groups participate in the ligand exchange reaction and form complexes that link selenium ions onto iron oxide. Therefore, the introduction of iron oxide particles on GO is expected to strengthen its affinity with high-valence selenium oxyanions. Furthermore, the GO-iron oxide composite could avoid the problem of high susceptibility to oxidation and agglomeration of small magnetic iron oxide particles with high surface free energy, when exposed to practical continuous flow systems.[6]

In this work, the Magnetic Particle-Graphene Oxide Composites -reduced by ethylene glycol (MGO-EG) composite was synthesized, characterized and further applied in selenium oxyanion adsorption. Nearly complete removal (> 99.9 % for selenite and > 95 % for selenate) was achieved within 10 seconds. Acidic condition could increase the selenium removal percentage to > 99.9 % in both selenite and selenate removal. A variety of factors, including initial selenium concentration, contact time, pH, temperature, interfering ions (NO_3^-, SO_4^{2-}, PO_4^{3-}, Ca^{2+}, Mg^{2+}) were also evaluated to study how they could influence the selenite an selenate adsorption. MGO-EG is later tested to be reusable with ten times of recycles. Possible synthesis and adsorption mechanism was proposed based on experiment results.

4.2 Experimental Section

4.2.1 Chemicals

Natural graphite (7 - 10 micro), potassium permanganate ($KMnO_4$), sodium nitrate ($NaNO_3$), H_2O_2 (30 %), 1-methyl-2-pyrrolidone (NMP), ferric acetylacetonate ($Fe(acac)_3$), ethylene glycol (EG), H_2SO_4 (98 %) were purchased from Alfa Aesar. 0.001N HCl, 0.1N NaOH, and acetone were purchased from Fisher Scientific Company, Canada. Milli-Q water was used in all processes of aqueous solution preparations and lavations.

4.2.2 Synthesis for GO

GO was prepared by a modified Hummers method.[18] Firstly, natural graphite flake (7 – 10 micron, 2g) and $NaNO_3$ (1.5 g) were mixed in a three necked flask with H_2SO_4 (98 %, 150 mL) in the ice-bath while a mechanical agitation was maintained. $KMnO_4$ (9 g) was then slowly added in the mixture while the ice bath and stirring were kept for another 2 hours. Then the ice bath was taken away and the agitation continued for another 5 days at room temperature (~ 25 ℃). Then, a portion of H_2O_2 (6 mL) was added into the mixture to neutralize unreacted $KMnO_4$, and the generated O_2 helped with the exfoliation of GO layers. After another 2 hours of agitation, the resulting bright yellow suspension was diluted and washed with a water solution (250 mL) containing H_2SO_4 (98 %, 7.5 mL) and H_2O_2 (30 %, 4.17 mL). Then sediment was washed repeatedly using Milli-Q water until neutral pH value. The sediment was dialyzed for another 5 days to clean out remnant dissolved ions. After an ultrasonic dispersion, fluffy golden flocci GO was attained using a freeze dryer.

4.2.3 Preparation for MGO-EG

A high temperature organic solvent reflux reaction was applied to *in situ* grow magnetic iron oxide onto GO sheets. GO (500 mg) was dispersed in 1-methyl-2-pyrrolidone (NMP, 150mL) by ultrasonication at room temperature (~ 25 ℃). The obtained GO/NMP mixture was then heated to 220 ℃ under the protection atmosphere of argon. Meanwhile, precursor $Fe(acac)_3$ (7.065 g, 20 mmol) was dissolved in NMP (100 mL) and EG (50 mL) mixed solution. The as-prepared mixture was added dropwise to the GO/NMP solution under vigorous stirring. The stirring was continued for another 5 hours after the dropping was finished. After cooling down to room temperature (~ 25 ℃), the mixture was washed several times by acetone and water alternatively. The precipitate was collected by magnetic separation. The resulting black powder was collected using freeze dryer.

4.2.4 Adsorption experiment

Adsorption experiments were conducted to test the effects of the initial selenium concentration, adsorption time, systematic pH, temperature and with the existence of interfering ions (NO_3^-, SO_4^{2-}, PO_4^{3-}, Ca^{2+}, Mg^{2+}). Adsorbent MGO-EG (20 mg, the dosage of absorbents was 1 g L^{-1}) was added to selenite and selenate standard liquid (20 mL, prepared from diluting 1000 ppm Na_2SeO_3 and Na_2SeO_4 stock water solutions). While controlled temperature was remained, samples were placed in the shaker chamber and oscillated for given hours at 300 rpm. NaOH and HCl were used to adjust systematic pH. MGO-EG was separated from solutions for reproducibility test by applying a neodymium magnet with a magnetic field of ~ 0.5T. Then collect the supernatant for further ICP-MS and IC analysis of ion concentrations. After washing with diluted NaOH (0.1 N, pH ~ 13) to desorb selenium and reactivated with diluted HCl (0.001 N, pH ~ 3), MGO-EG was reused to repeat the exact test with the same initial selenium concentration and oscillation time for reusability test.

4.2.5 Characterization Methods

Atomic Force Microscope (AFM) was conducted using an Asylum MFP-3D system with tapping mode. AFM samples were prepared by dropping GO water solution onto a fresh mica surface and dried overnight. X-Ray Diffraction (XRD) was taken on a RIGAKU Rotating anode XRD system with a copper anode, 40 kv, 2 degs minute^{-1}. Fourier Transform Infrared Spectroscopy (FTIR) spectra were recorded on a Nicolet iS50 FT-IR Imaging System. X-ray Photoelectron Spectroscopy analysis (XPS) was conducted using an AXIS 165 XPS Spectrometer. All the bonding energies have been corrected by referring to the C 1s photoelectron peak at 284.8 eV. Thermo Gravimetric Analysis (TGA) was conducted with a TA Instrument Q-500 equipment, with a heating rate of 10 ^{o}C min^{-1} and nitrogen as the purge gas. Before the tests, all the samples were carefully ground to powders to ensure sufficient diffusion of heat. The measurements were conducted using ~ 20 mg samples, and weight retention/temperature curves were recorded. Morphology investigations of GO and MGO-EG were performed by Transmission Electron Microscopy (TEM) using a Hitachi HF 3300 Mode and a Scanning Electron Microscope (SEM) Vega-3 (Tescan). TEM samples were prepared by pipetting several microliters of GO and MGO-EG dispersion on to lacey carbon coated copper grids and dried. A Quantum Design 9T-PPMS magnetometer was used to record the magnetic hysteresis curve. Zeta potential was measured with a ZetaPALS Zeta potential analyser. All samples for zeta potential measurements were carefully dispersed in water solution with ultrasonic for 10 min. A Perkin Elmer's Elan 6000 Inductively Coupled Plasma-Mass Spectrometry (ICP-MS) and a Ion Chromatography (IC) DX-600 by Dionex was used to measure the concentration of cations (selenite, selenate, Ca^{2+}, Mg^{2+}) and anoins (NO_3^-, SO_4^{2-}, PO_4^{3-}) of ppb and ppm level, separately.

4.3 Results and Discussion

4.3.1 Characterization of as synthesized GO and MGO-EG

In this work, GO was prepared initially from oxidizing natural graphite using a modified Hummers Methods.[19] Then, magnetic nanoparticles *in situ* grew on GO sheets to form the magnetic particle-GO composite (MGO-EG) through a high temperature solution reflux with ethylene glycol as the reducing agent and stabilizer.

4.3.1.1 Atomic Force Microscopy (AFM) imaging

Figure 4-1 shows the Atomic Force Microscope (AFM) image of GO and the height profile of a section as marked by the line. The observed GO sheet is large (about 2 μm × 2 μm) and flat. The height profile shows that the thickness of this GO sheet is ~ 1.09 nm, which indicates that this GO sheet is a mono layer.[20] GO sheets are expected to be thicker than pristine graphite mono layer (van der Waals thickness of ~ 0.34 nm), due to the addition of covalently bounded oxygen and the displacement of the sp^3-hybridized carbon atoms that slightly above and below the original graphite plane. Most of other sheets observed during the AFM experiment have the similar thickness of ~ 1 nm as well, indicating the as prepared GO has high ratio of mono layer. The diluted GO suspension was found to be stable, homogenous and clear, which indicated that the as-prepared GO has good water dispersity, due to the introduction of hydrophilic oxygen-containing groups on the GO surfaces.

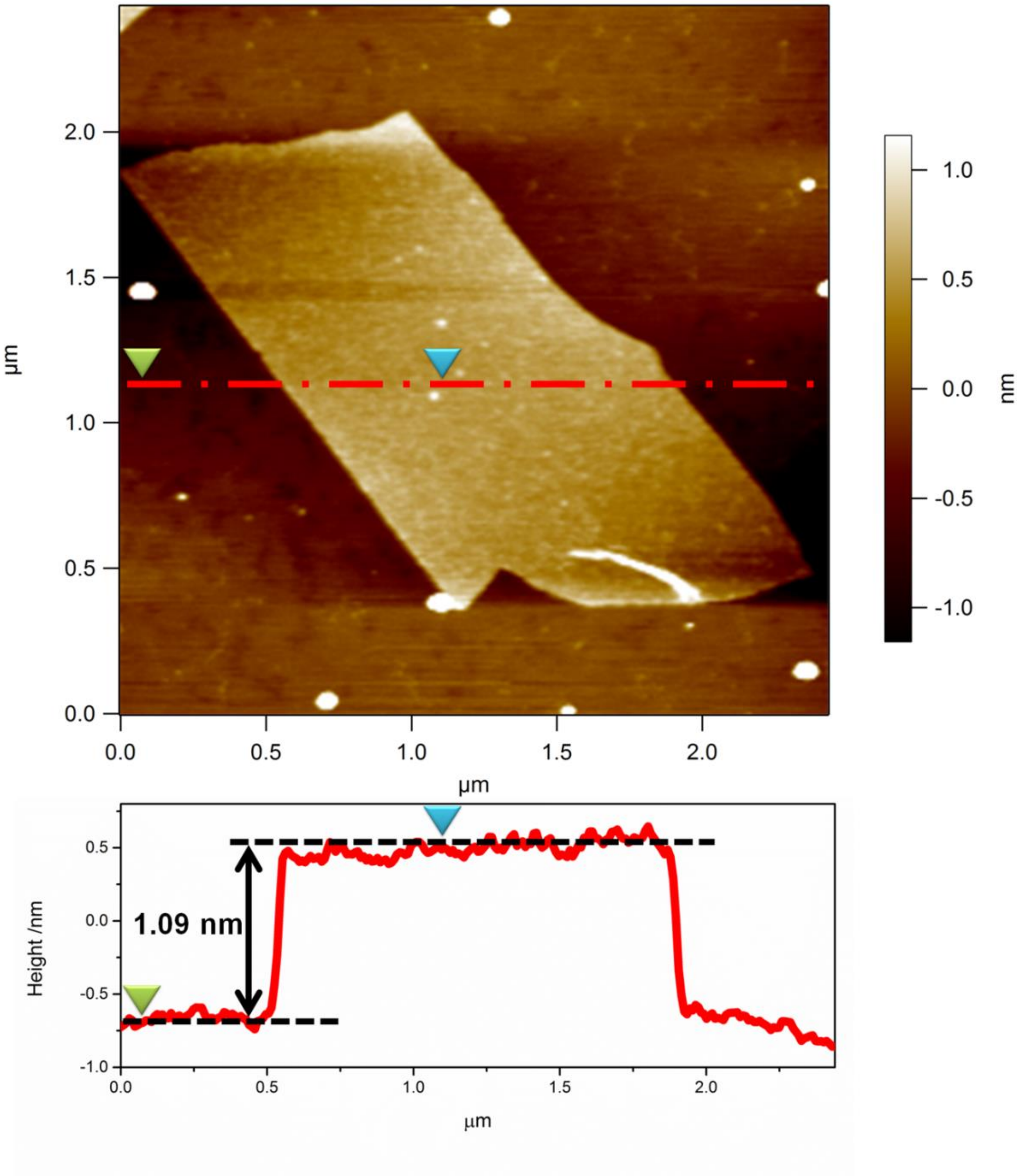

Figure 4-1 Tapping mode AFM image of GO sheets with height profile for mono layer GO (~ 1.09 nm).

4.3.1.2 Characterization by Transmission Electron Microscopy (TEM), Scanning Electron Microscope (SEM) and Energy Dispersive Spectrometry (EDS)

In good accordance with the AFM image of GO, Transmission Electron Microscopy (TEM) image (Figure 4-2 a) also shows that GO are large, transparent, silk-like sheets, entangling with each other. The morphology of MGO-EG composite is also characterized by TEM (Figure 4-2 b) and Scanning Electron Microscopy (SEM) image (Figure 4-3 a). As similarly shown in both images, a large amount of magnetic particles (with an average particle size ~ 10 nm) are distributed homogeneously on GO sheets.

Element content of MGO-EG is characterized by EDS (Figure 4-3 b). The signal of Fe (~ 17.41 atomic%) comes from magnetic particles; the signal of O (~ 44.76 atomic%) comes from both iron oxide and oxygen containing functional groups located on GO; and the signal of C (~ 37.68 atomic%) evidently comes from graphene substrate itself.

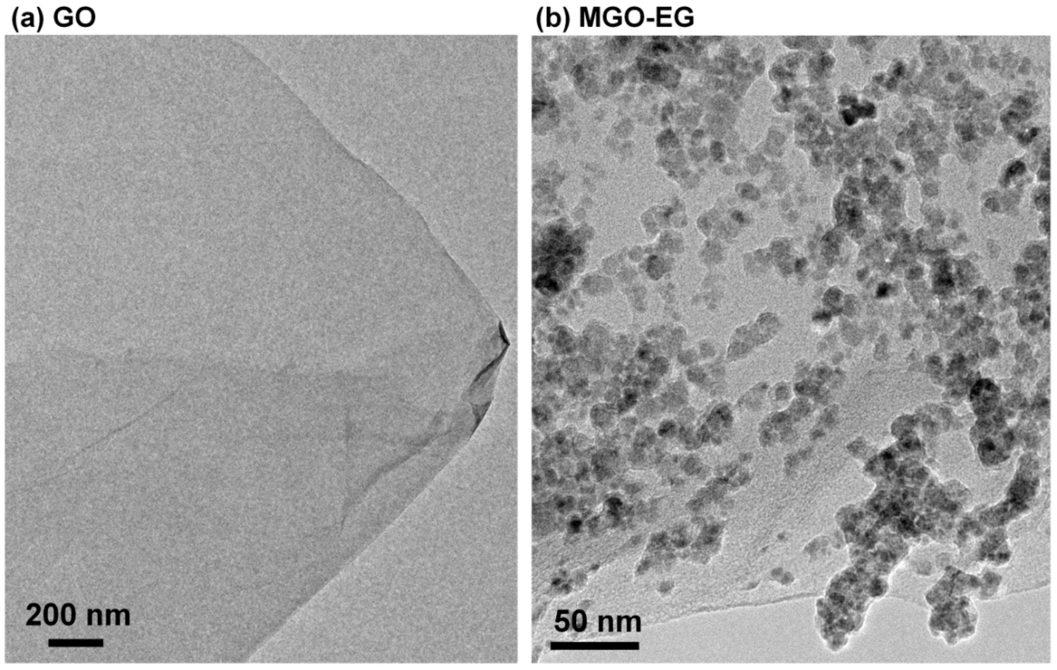

Figure 4-2 TEM images of (a) GO, and (b) MGO-EG.

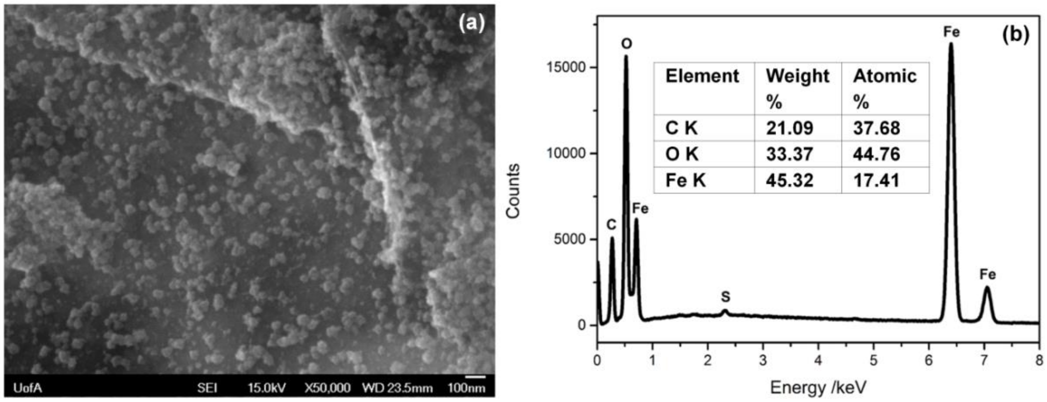

Element	Weight %	Atomic %
C K	21.09	37.68
O K	33.37	44.76
Fe K	45.32	17.41

Figure 4-3 SEM images of (a) MGO-EG and (b) EDS spectrum and element content analysis.

4.3.1.3 X-ray diffraction (XRD) analysis

Figure 4-4 shows the normalized intensities of powder X-ray diffraction (XRD) of (A) graphite, (B) GO and (C) MGO-EG. Signal intensities of the strongest peak in graphite, GO and MGO-EG are set as 1, respectively; and the other peaks are normalized according to their relative ratio. According to Bragg Equation,

$$2d\,\sin\theta = \lambda \tag{1}$$

where λ is the wavelength of X-ray Cu $K\alpha$ (0.154 nm). As calculated from 2θ = 10.4 ° in GO (002) diffraction plane, the interlayer spacing (d) of GO is 0.85 nm, which is much larger than the d-spacing of graphite (0.34 nm). The spacing difference is mainly due to the addition of oxygen-containing functional groups on the GO planes, as discussed in AFM analysis. Meanwhile, diffraction peaks of MGO-EG at 2θ = 18.3 °, 30.3 °, 35.8 °, 43.4 °, 53.5 °, 57.3 °, 63.2 °, 71.1 °, and 74.5 ° could be assigned to crystal planes (111), (220), (311), (400), (422), (511), (440), (620) and (533) of Fe_3O_4, according to JCPDS card (19-0629). The approximate particle size of Fe_3O_4 could be calculated from Sherrer's Equation,

$$D \;=\; K\,\lambda\,/(\beta\,\cos(\theta)) \tag{2}$$

where the constant K = 0.89,[21] λ is the wavelength of X-ray Cu $K\alpha$ (0.154 nm), β is the full width at half maximum (radian) of the diffraction peak (= 0.570/180×π), θ is diffraction angle (radian) (= 35.798/2/180×π), and D represents the crystallite size, which is calculated to be 14.48 nm. This approximate particle size is in good accordance with the TEM and SEM imaging results.

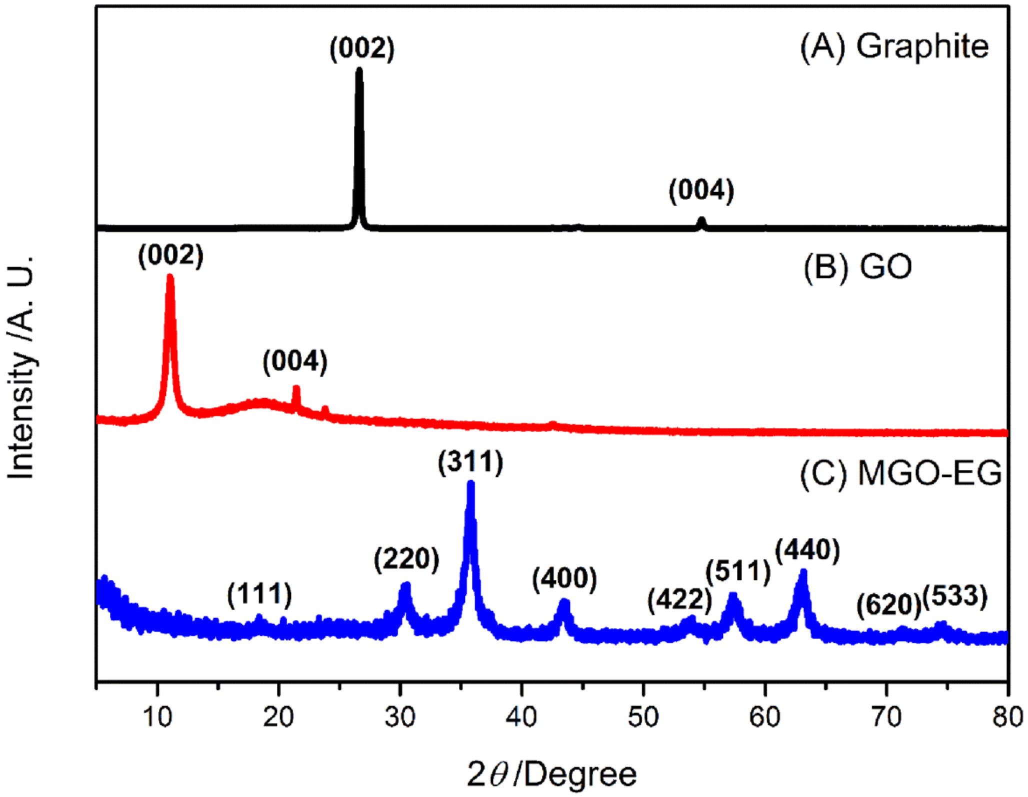

Figure 4-4 Powder X-ray diffraction patterns of (A) graphite, (B) GO and (C) MGO-EG.

4.3.1.4 Fourier Transform Infrared Spectroscopy (FTIR) analysis

Figure 4-5 shows the Fourier Transform Infrared Spectroscopy (FTIR) spectra of (A) natural graphite, (B) GO, and (C) MGO-EG powders. Broad peaks at 3000 - 3700 cm^{-1} can be observed in GO spectrum, which are attributed to –OH groups; while in MGO-EG, the corresponding peak is obviously weakened, indicating the partial loss of hydroxyl groups during the high temperature synthesis. Similarly, carboxyl groups could be evidenced from peaks in GO at 1738 cm^{-1}, 1617 cm^{-1}, 1053 cm^{-1}, 965 cm^{-1}; while in MGO-EG, these peaks are weakened and shifted in different degrees, affected by the deposition of iron oxide.

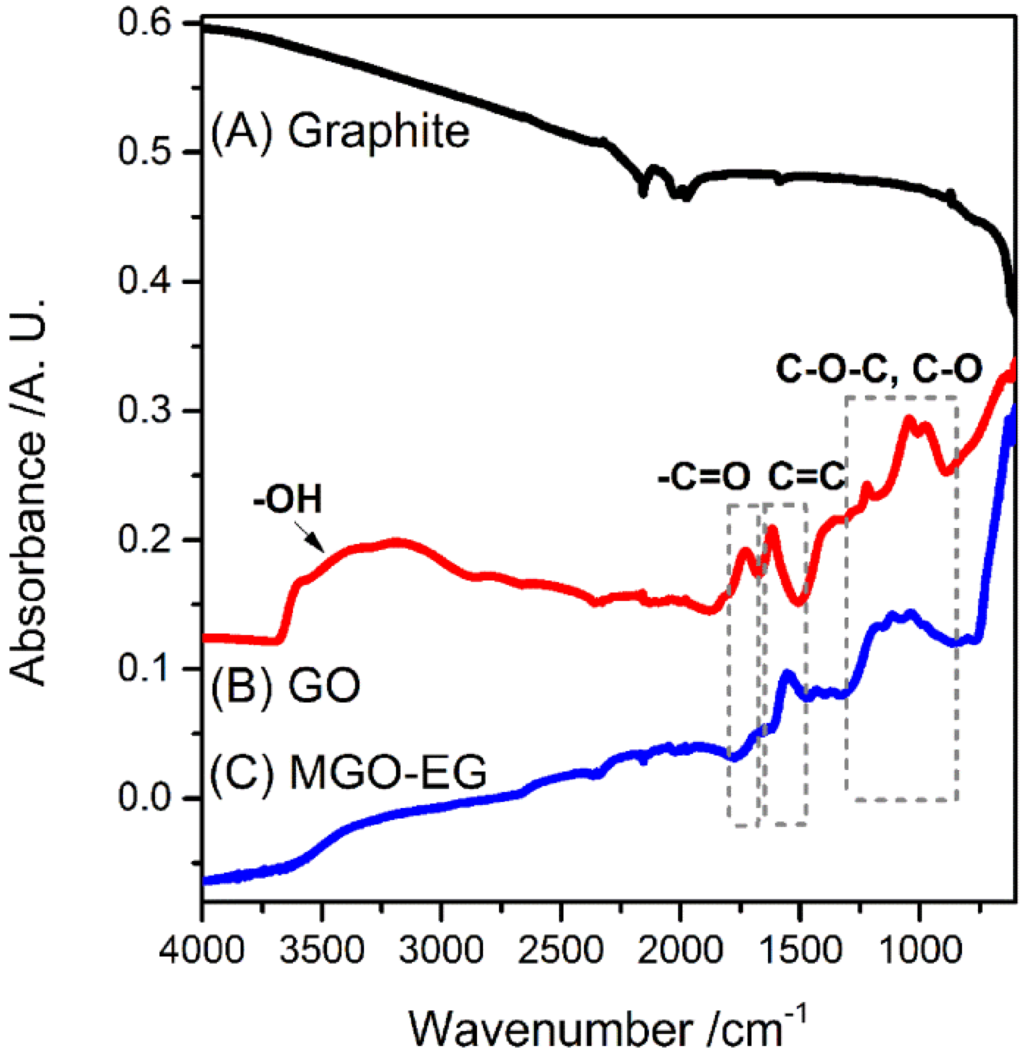

Figure 4-5 FTIR spectra of (A) graphite, (B) GO and (C) MGO-EG.

4.3.1.5 X-ray Photoelectron Spectroscopy (XPS) analysis

Figure 4-6 shows the X-ray Photoelectron Spectroscopy (XPS) spectrum of GO, MGO-EG and MGO-EG with adsorbed selenium. Deconvolution of C1s spectra (Figure 4-6) of GO indicates that there are four different types of carbon species in GO: C-C (284.6 eV) framework in graphene structure; hydroxyl carbon (C-OH) (288.8 eV) on GO surface; carbonyl carbon (C=O) (287.8 eV) and carboxyl carbon (O-C=O) (288.9 eV) on GO edges and surface defects.[22-25] In accord with FTIR spectra, the presence of oxygen-containing functional groups on GO is further confirmed by XPS. Similar peaks could be found in MGO-EG C1s spectrum with certain shift. It is noticed that the relative intensity of C-O bond and C-C bond are decreased in MGO-EG. The decrease could be attributed to the formation of new Fe-O bond and the breakage of C-OH bond. Meanwhile, iron oxides particles deposited on the GO surfaces can also impact the intensity of C-C due to the limited penetration depth of XPS detection. These effects could be observed in O1s spectra (Figure 4-6 b) as well. In O1s spectrum of GO, the peak for O-H bond (532.5 eV) is notably dominant and diminishes other peaks. However, in MGO-EG, peaks for C-O (633.1 eV) and C=O (534.0 eV) are diminished. The appearance of a new peak at 530.5 eV (Figure 4-6 b) results from the formation of Fe-O bond possibly in both Fe_3O_4 and γ-Fe_2O_3, as indicated from Fe 2p spectrum (Figure 4-6 d). Figure 4-6 d is Se 3d spectrum, presumably showing that selenate has higher bonding energy than selenite. Moreover, it is indicated from the Se double peaks that the oxidation state for both selenite and selenate do not change during the adsorption process.

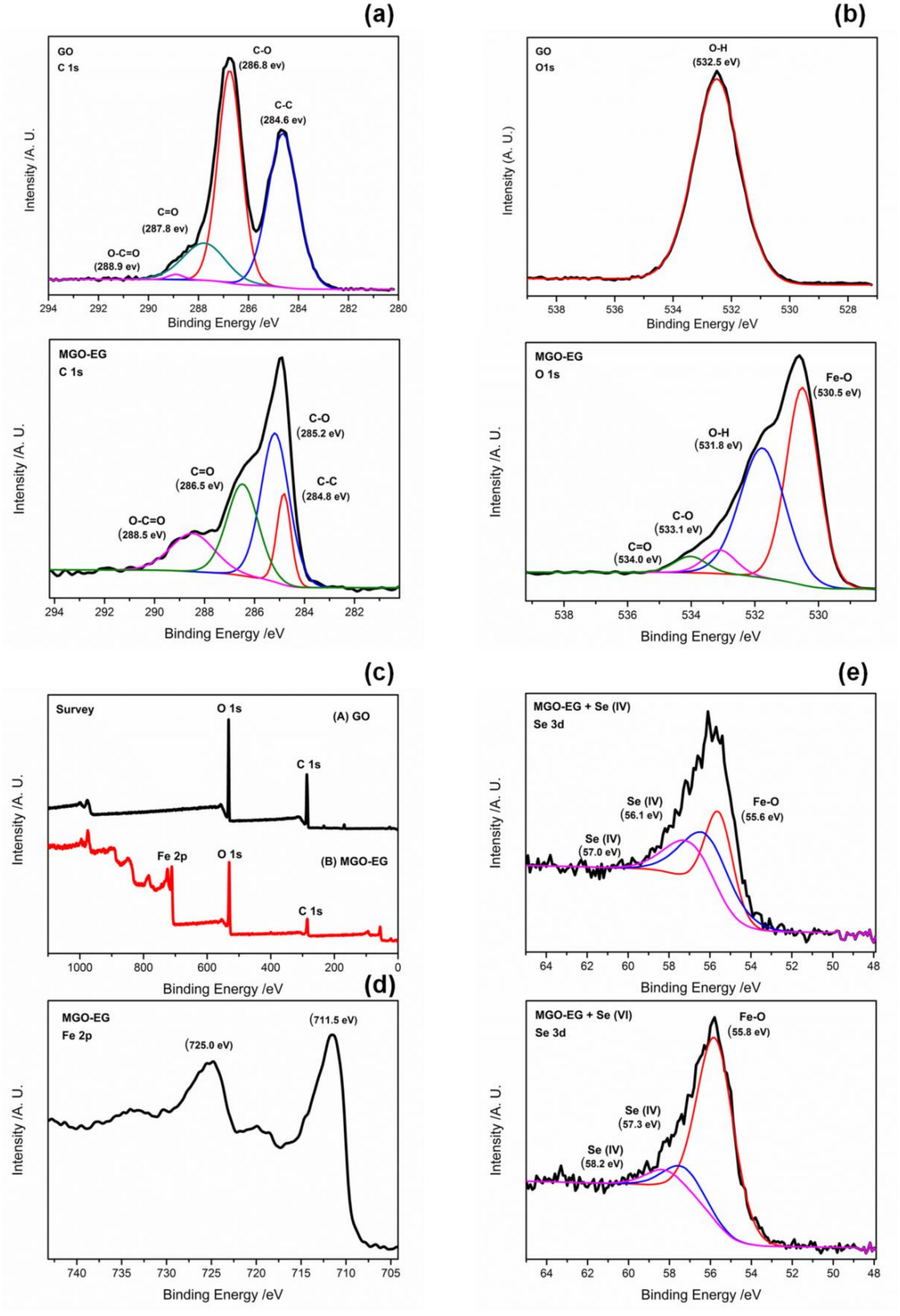

Figure 4-6 XPS patterns of (a) C1s, (b) O1s for GO and MGO-EG; (c) GO and MGO-EG survey; (d) Fe 2p; (e) Se 3d after adsorption using MGO-EG.

4.3.1.6 Thermo Gravimetric Analysis (TGA) analysis

Figure 4-7 shows the Thermo Gravimetric Analysis (TGA) curves of (A) graphite, (B) GO and (C) MGO-EG. During the heat treatment, graphite exhibited higher thermo stability with a weight loss ratio of only 4.1 % at 1000 ^{o}C. The lower thermo stability of GO and MGO-EG is because of the introduction of oxygen-containing functional groups that destroyed the multilayered stack structure of graphite, lowered the van der Waals interactions between layers, and thus accelerating the process of weight loss.[20] The weight loss of GO could be divided into three stages: the first stage related to the graduate loss of physically adsorbed water is from 30 ^{o}C to 120 ^{o}C; the second and most important stage is at around 187 ^{o}C to 220 ^{o}C, due to the decomposition of labile hydroxyl, carboxyl and epoxy groups, yielding CO, CO_2, and other steam; the third stage started from 500 ^{o}C, which could be the pyrolysis of those more stable oxygen containing groups and graphene oxide framework itself.[26] The total weight loss till 1000 ^{o}C would be 84.5 % or more. MGO-EG displayed better thermo stability than GO, with the grafting of magnetic nanoparticles that could impose a restriction on MGO-EG movement and resulting in a more homogeneous heating and avoid the heat concentration.[27] The highest derivate weight loss of MGO-EG is around 600 ^{o}C, indicating the possible breakage of Fe-C, Fe-O, and C-C bond.[28]

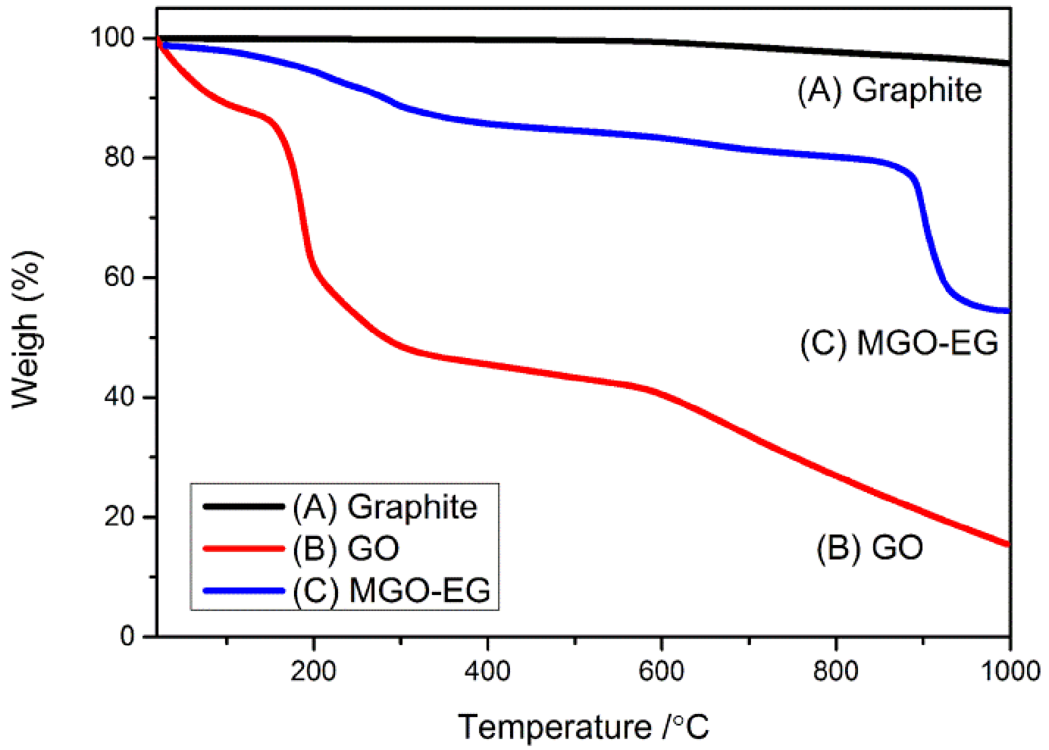

Figure 4-7 TGA curves of (A) Graphite, (B) GO, and (C) MGO-EG.

4.3.1.7 Magnetic properties of MGO-EG

Figure 4-8 shows the magnetic hysteresis curve (Figure 4-8), zoom-in magnetization curve of MGO-EG (inserted Figure 4-8 b), pictures taken before (Figure 4-8 c) and after (Figure 4-8 d) the magnetic separation in ten seconds. As indicated from Figure 4-8 a and Figure 4-8 b, during the magnetization process, the magnetization intensity of MGO-EG increases with the external magnetic field until ultimately tends to saturate. When the external magnetic intensity decreases gradually back to zero, the magnetization intensity of MGO-EG decreases toward zero as well; when a negative magnetic field is applied, it tends to saturate negatively. The magnetic hysteresis loops are close enough to make S-like superposition curves. This indicated that MGO-EG exhibits a good super paramagnetic behaviour since there was almost no remaining magnetization when the external magnetic field was removed. According to the hysteresis loop, the magnetic remanence (*M*r) of the sample is 0.47 emu g^{-1}; coercivity (*H*c) is 0.03 Oe, both are nearly zero. The specific saturation magnetization (*M*s) of the sample is 49.7 emu g^{-1}. This value is smaller than the 92 emu g^{-1} of pure Fe_3O_4 nanocrystals (diameter ~ 200 nm) reported in published literature.[29] The reduction in the value of Ms could be attributed to the rather smaller size (diameter ~ 10 nm) of the iron oxide particles and the presence of GO sheets. However, the Ms value measured here is still much higher than the previously reported values of magnetic particle-graphene oxide composites (e. g. about 1 to 8 emu g^{-1}, varies with different Fe_3O_4/GO ratio,[30] and 4.62 emu g^{-1}[31]).This favourable magnetism guarantees thorough magnetic separation after adsorption process, avoiding the pollution of introduced Fe from adsorbent, and making it possible to recycle MGO-EG. As shown in Figure 4-8 c and Figure 4-8 d, the magnetic separation could be achieved within 10 seconds under an external magnetic field of ~ 0.5 T.

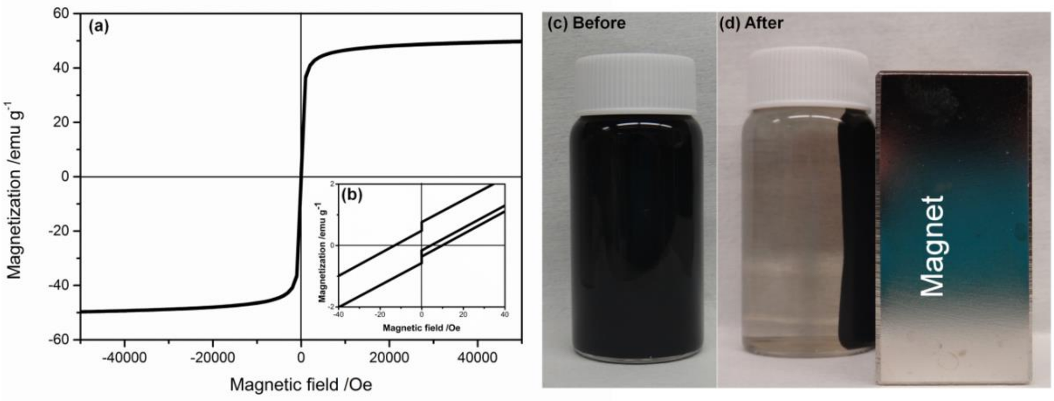

Figure 4-8 (a) Magnetic hysteresis loop of MGO-EG with a bottom inset (b) of a close view of the hysteresis loop. (c) Before and (d) after the magnetic separation after about ten seconds.

4.3.2 MGO-EG synthesis mechanism

Possible mechanisms for synthesis and adsorption are proposed based on experimental results (shown in Figure 4-9). GO was synthesized through a modified Hummers method[18] by oxidizing graphite. GO is negatively charged[32] in water solution due to the presence of hydroxyl and carbonyl groups. Positive Fe^{3+} ions would first attached to GO surface via electrostatic attraction and act as nucleation precursors. In synthesis of MGO-EG, the added Fe^{3+} was partly reduced to Fe^{2+}, thus both Fe_3O_4 and γ-Fe_2O_3 were deposited and later formed magnetic particles.[33] Ethylene Glycol (EG) acted as both a stabilizer and the reducing agent. The addition of EG could enhance the magnetic properties by producing more reduced Fe^{2+} species.

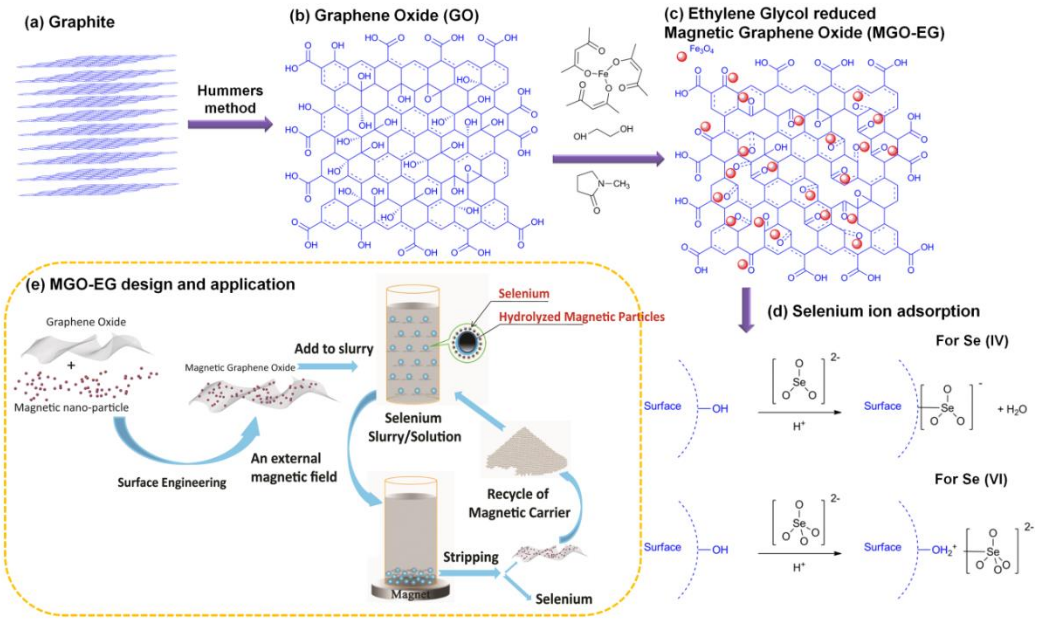

Figure 4-9 (a) Schematic of graphite structure; (b) schematic of GO structure; (c) schematic of MGO-EG structure; (d) proposed selenite (Se (IV)) and selenate (Se (VI)) adsorption reaction mechanism on MGO-EG; (e) Scheme of MG-EG synthesis, selenium adsorption on MGO-EG, and MGO-EG stripping and reuse.

4.3.3 Selenium adsorption tests with MGO-EG

MGO-EG was then applied to a series of adsorption tests in selenium solutions with different initial selenium concentrations (1 ppb to 100 ppm), pH (2 to 12), contact time (10 seconds to 24 hours), temperature (4 ^{o}C to 80 ^{o}C), different possible interfering ions (NO_3^-, SO_4^{2-}, PO_4^{3-}, Ca^{2+}, Mg^{2+}) under different pH and concentrations for a better understanding of the adsorption process of selenium ions on MGO-EG.

4.3.3.1 Definition of adsorption capacity Q (mg g^{-1}) and removal percentage q (%)

In the adsorption experiment, the adsorption capacity Q (mg g^{-1}) and removal percentage q (%) are defined as follows,

$$Q = \frac{(C_0 - C) \times V}{W} \tag{3}$$

$$q = \frac{C_0 - C}{C_0} \times 100 \tag{4}$$

where C_0 (ppm) is the initial selenite or selenate concentration, C (ppm) is the equilibrium selenite or selenate concentration after adsorption, W (g) is the adsorbent weight, and V (mL) is the volume of the solution.

Solutions of different initial selenite and selenate concentrations were used in the adsorption tests, and the results are summarized in the Q-C_0 (Figure 4-10) and q-C_0 (Figure 4-11) curves. Similar trends on for selenite and selenate could be observed from Figure 4-10. It is demonstrated in the figure that the higher the C_0 value is, the higher value of Q and q would be; the Q-C_0 and q-C_0 curves tends to reach a saturation platform eventually, indicating a saturated adsorption capacity.

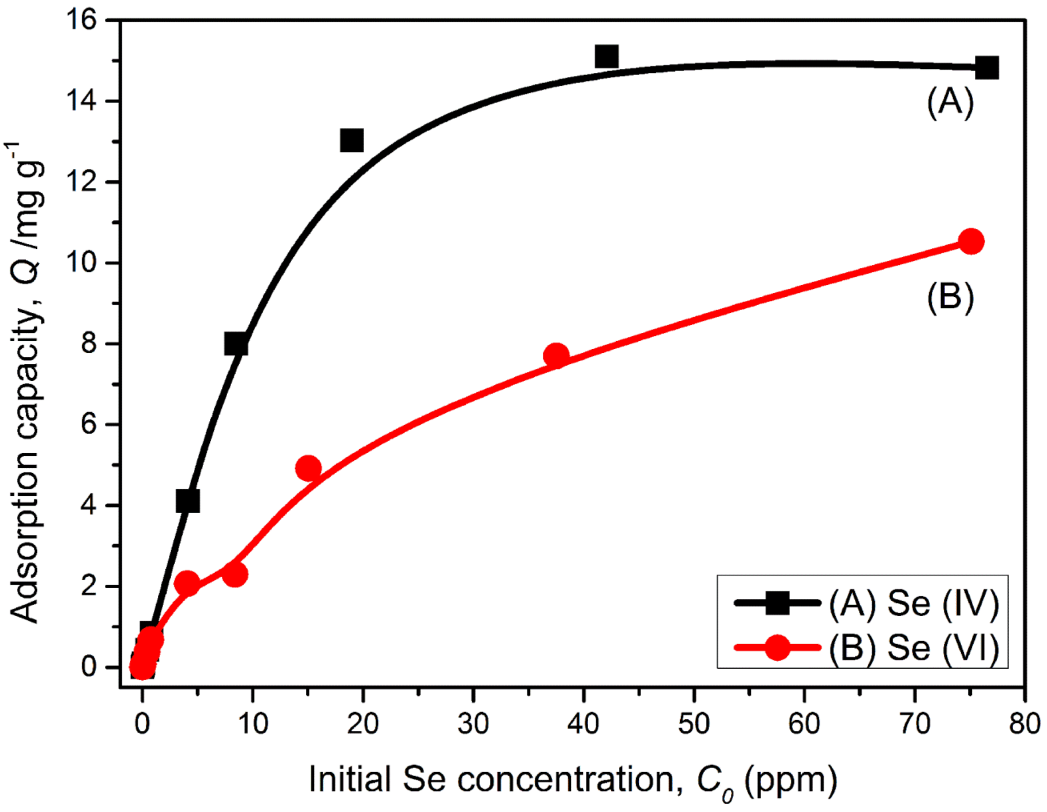

Figure 4-10 (a) Q-C_0 curves with different initial Se (IV) and Se (VI) concentrations. MGO-EG dosage 1 g L^{-1}, under neutral pH (~ 6), room temperature (~ 25 ℃), shaking rate 300 rpm, adsorption time for 24 hours.

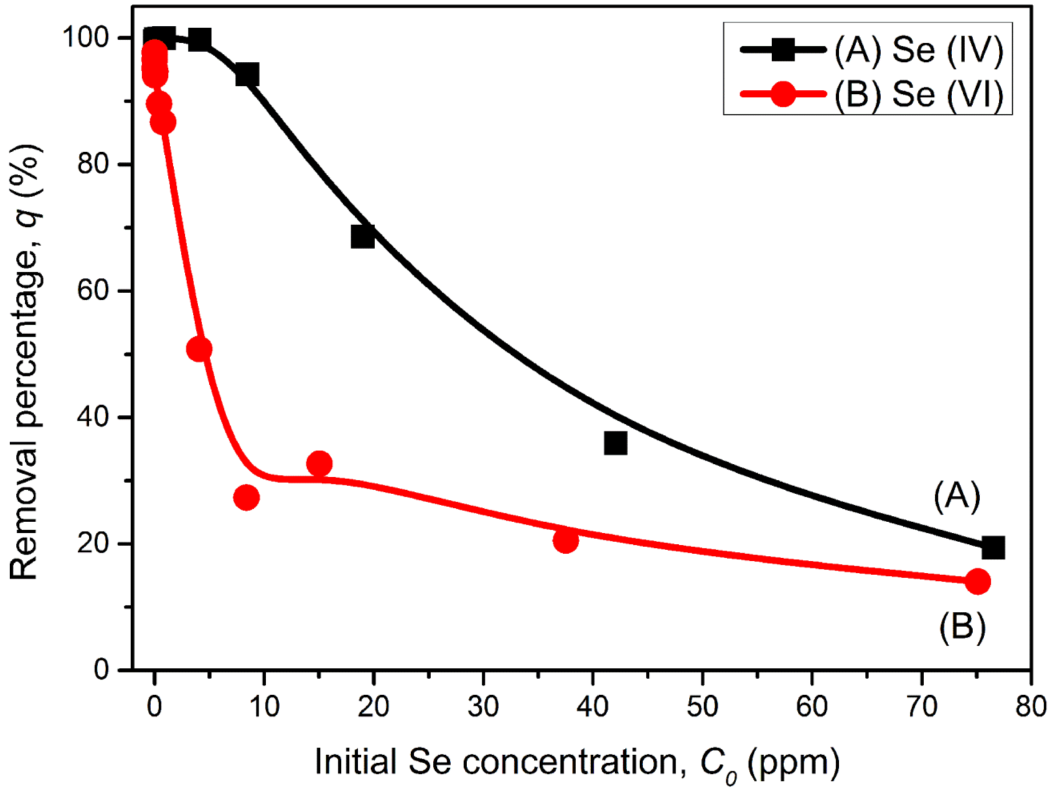

Figure 4-11 q-C_0 curves with different initial Se (IV) and Se (VI) concentrations. MGO-EG dosage 1 g L^{-1}, under neutral pH (~ 6), room temperature (~ 25 ℃), shaking rate 300 rpm, adsorption time for 24 hours.

4.3.3.2 Adsorption curves fitted with Freundlich and Langmuir adsorption Models

The adsorption capacity vs. selenite and selenate equilibrium concentration (Q-C) curves have been fitted using both Freundlich and Langmuir adsorption Model (Figure 4-12).

At a constant temperature, Freundlich Adsorption Equation[34] is expressed as:

$$Q = K \times C^n \tag{5}$$

where K and n are Freundlich Constants. When n is between 0.1 and 1, the adsorption process is considered optimal adsorption. While $n > 2$, the adsorption is significantly difficult to occur.[35, 36]

At a constant temperature, Langmuir Adsorption Equation is represented by the equation,

$$Q = \frac{a \times b \times C}{1 + b \times C} \tag{6}$$

where a and b are Langmuir Constants. a (mg g^{-1}) indicates the saturate adsorption capacity and b (L mg^{-1}) is a constant related to adsorption free energy. Figure 4-12 shows that both models could well fit the adsorption curves, and the values of the fitting parameters are listed in Table 4-1. The n values in both selenite and selenate cases are less than 1, indicating optimal adsorptions for both processes.

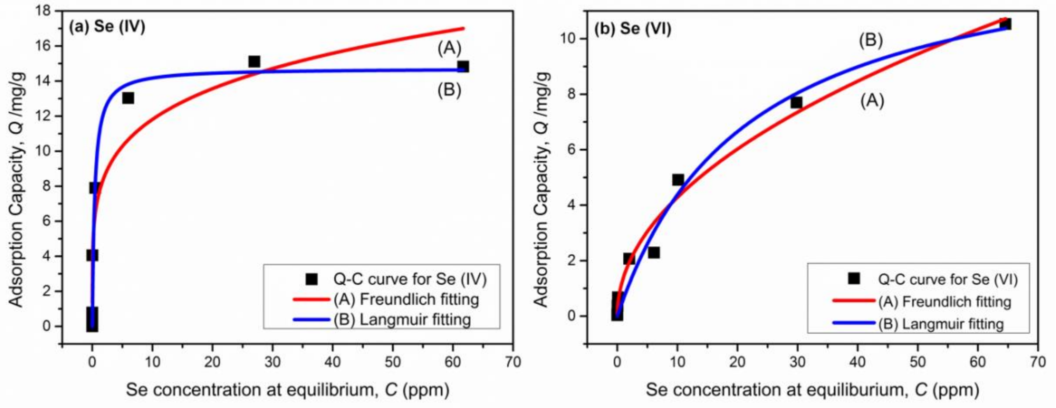

Figure 4-12 Fitting curves using Freundlich and Langmuir Models under different initial (a) Se (IV) and (b) Se (VI) concentrations.

Isotherm type	Isotherm constants	Se (IV)	Se (VI)
Freundlich	K	7.455	1.383
	n	0.200	0.491
	R_F^2	0.939	0.982
Langmuir	a [mg g^{-1}]	14.731	13.829
	b [L mg^{-1}]	2.539	0.046
	R_L^2	0.961	0.977

Table 4-1 Freundlich and Langmuir adsorption isotherm parameters for Se (IV) and Se (VI) adsorption on MGO-EG.

4.3.3.3 Effect of pH value on selenium adsorption

The pH effect on the adsorption of selenite and selenate on MGO-EG is summarized and shown in Figure 4-13. The removal percentage of selenite remains almost complete (> 99.9 %) from acidic pH to pH ~ 10 and then drastically drops at pH ~ 11, while the removal percentage of selenate gradually decreases from > 99.9 % with increasing pH and decrease sharply from pH ~ 9. As the conclusion, lower pH facilitates the adsorption of both selenite and selenate on MGO.

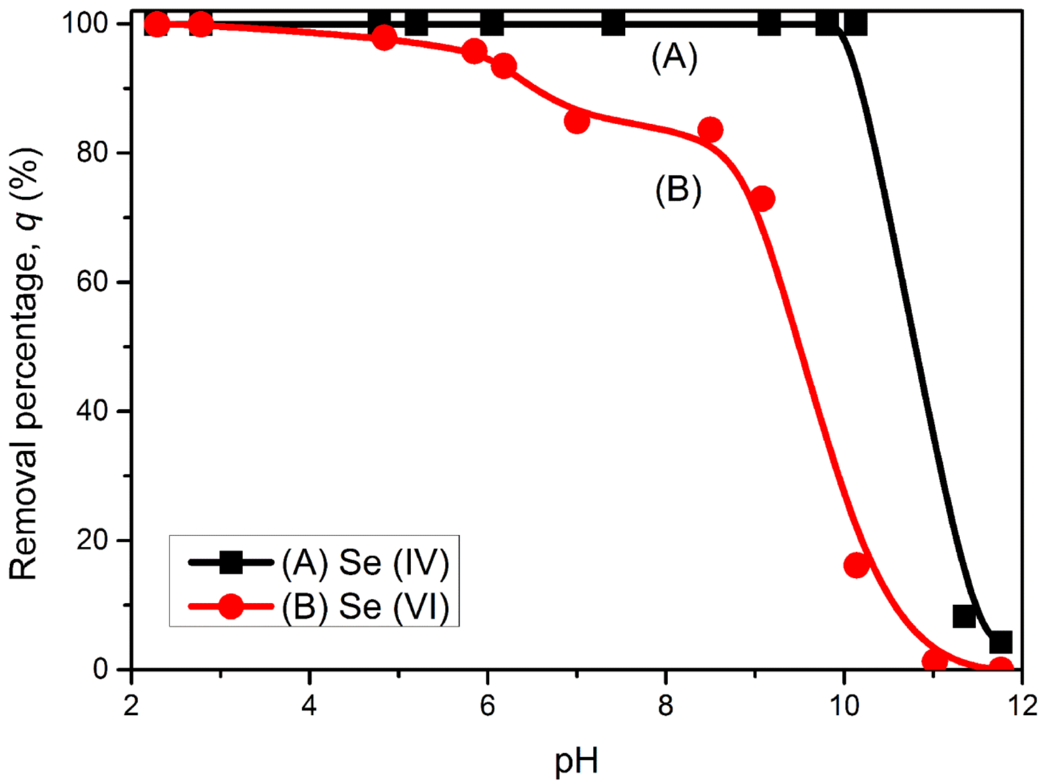

Figure 4-13 Effect of pH on selenium adsorption: MGO-EG dosage 1 g L^{-1}, initial selenium concentration 300 ppb room temperature (~ 25 ℃), shaking rate 300 rpm, adsorption time for 24 hours.

4.3.3.4 Kinetics of selenium adsorption on MGO-EG

Adsorption time (immersion time of MGO-EG in selenite and selenate solution) was recorded with initial selenite and selenate concentration of 300 ppb, MGO-EG dosage 1 g L^{-1}, under natural pH (~ 6), room temperature (~ 25 ℃), and shaking rate 300 rpm. The results in Figure 4-14 indicate that the adsorption process would be completed within ~ 10 seconds, which is much more efficient than the adsorbents reported previously, such as goethite (~ 50 hours),[2] magnetite (~ 30 hours),[12] hematite (~ 5 hours),[17] Fe/Fe_3C nanoparticles (30 min)[37] and Fe_3O_4 (10 min)[37]. The fast adsorption rate makes MGO-EG composite a suitable candidate for water treatment application in industry.

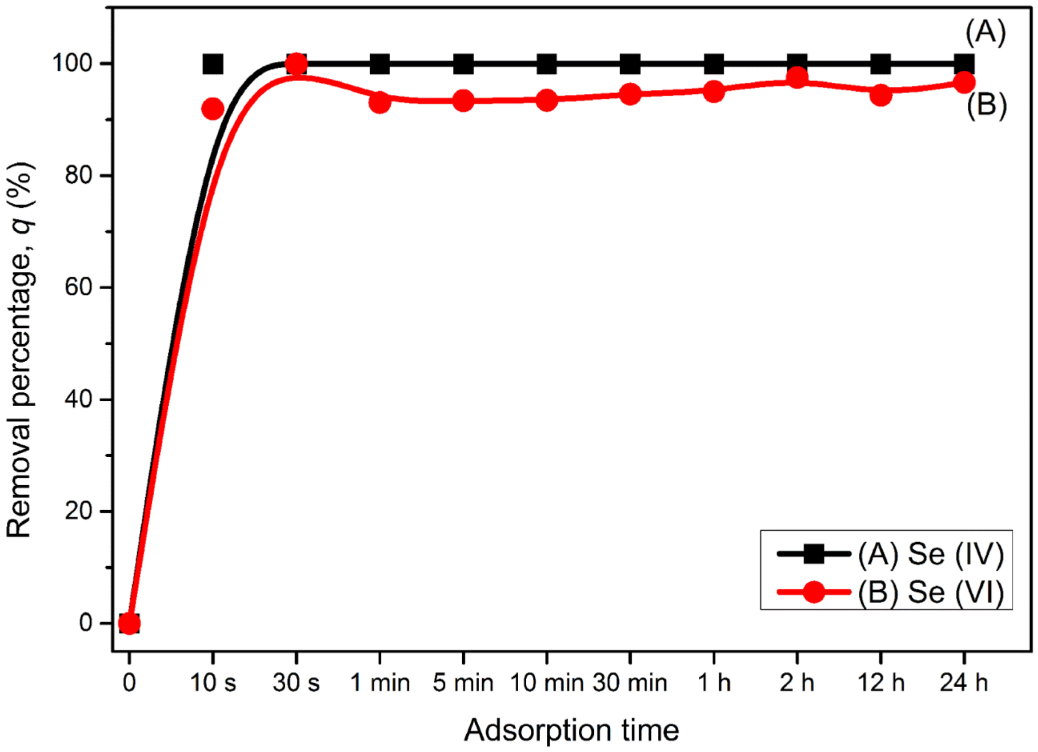

Figure 4-14 Effect of adsorption time on selenium adsorption: MGO-EG dosage 1 g L^{-1}, under neutral pH (~ 6), initial selenium concentration 300 ppb, room temperature (~ 25 ℃), shaking rate 300 rpm.

4.3.3.5 Effect of adsorption temperature on selenium adsorption

Adsorption temperature effect was also tested from 4 ^{o}C to 80 ^{o}C (Figure 4-15) with initial selenite/selenate concentration of 300 ppb, MGO-EG dosage 1 g L^{-1}, under natural pH (~ 6), and shaking rate 300 rpm for 24 hours. Higher temperature results in a slightly decreased removal percentage (~ 10 %) for selenate, while there is negligible change of removal percentage for selenite within the temperature studied (4 ^{o}C – 80 ^{o}C). The Gibbs free energy of the adsorption process is given by:

$$\mathit{\Delta} G = \mathit{\Delta} H - T\mathit{\Delta} S \tag{7}$$

Where ΔG is the Gibbs free energy (J) for selenium ion adsorption on MGO-EG, ΔH is enthalpy (J), T is temperature in Kelvin (K), ΔS is entropy (J K^{-1}). In order to make this adsorption reaction proceed spontaneously in the forward direction, ΔG has to be negative. Since $T > 0$, $\Delta S < 0$ (atoms become ordered during adsorption thus cause reduction in entropy), ΔH has to be negative, which means the selenite and selenate adsorption process is exothermal and therefore the higher the temperature the relative lower adsorption ratio. According to the figure, temperature change (4 ^{o}C – 80 ^{o}C) has ~ 10 % decrease in the removal percentage of selenate and negligible effect on selenite within the studied temperature range.

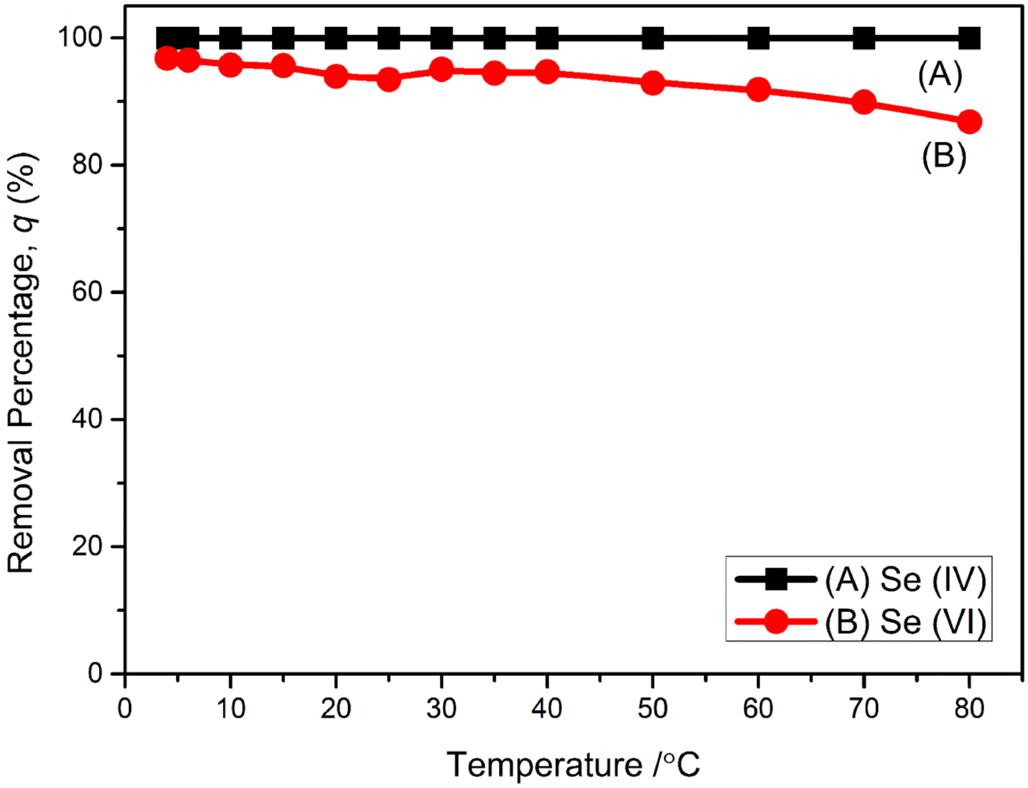

Figure 4-15 Effect of adsorption temperature on selenium adsorption: MGO-EG dosage 1 g L^{-1}, under neutral pH (~ 6), initial selenium concentration 300 ppb, shaking rate 300 rpm, adsorption time for 24 hours.

4.3.3.6 Comparison between MGO, GO and pure Fe_3O_4 particles (400 nm and 10 - 20 nm) for adsorption of selenite and selenate ions at different concentrations.

Further comparison between MGO-EG and pure Fe_3O_4 particles (400 nm and 10 - 20 nm, separately) for selenium adsorption were depicted in Figure 4-16 a for selenite and Figure 4-16 b for selenate. In Figure 4-16 a, MGO-EG and Fe_3O_4 (10 - 20 nm) demonstrate strong adsorption abilities for selenite removal with the removal percentage ~ 95 % within the initial selenite concentrations tested (C_0: 0 - 10 ppm). However, Fe_3O_4 (400 nm) has much lower adsorption efficiency (~ 20 % at C_0: 0 - 0.5 ppm, and drop gradually to zero at $C_0 = 10$ ppm) towards selenite removal. This result may imply the similar adsorption mechanisms of selenite on MGO-EG and Fe_3O_4, and the particle size of adsorbent plays an important role in the adsorption of selenite. The smaller the particle size, the higher the specific surface area. Higher surface area will dramatically increase the number of adsorption sites per unit area. In case of selenate removal, MGO-EG still holds the highest removal percentage within the initial selenite concentrations tested (C_0: 0 - 10 ppm). However, the removal percentage of selenate drops sharply with increasing initial selenate concentration. Similar to selenite removal, Fe_3O_4 (10 - 20 nm) has better removal percentage than Fe_3O_4 (400 nm) due to the larger surface area. Nevertheless, Fe_3O_4 (10 - 20 nm) exhibits much weaker affinity to selenate with a removal percentage of < 20 % at initial selenate concentration ~ 0.1 ppm. GO adsorbing ability increases with increasing initial Se concentration and possesses a relative stable saturation removal percentage of 20 % to 30 % in both cases. It could be speculated that MGO-EG show far better selenate affinity than Fe_3O_4 (10 - 20 nm) because graphene oxide plays a significant role. For one reason, the hydroxyl groups located on GO would create active adsorption sites; for the other, the conjugated π bond of partly reduced graphene oxide help with the stability of outer-sphere complex.[38]

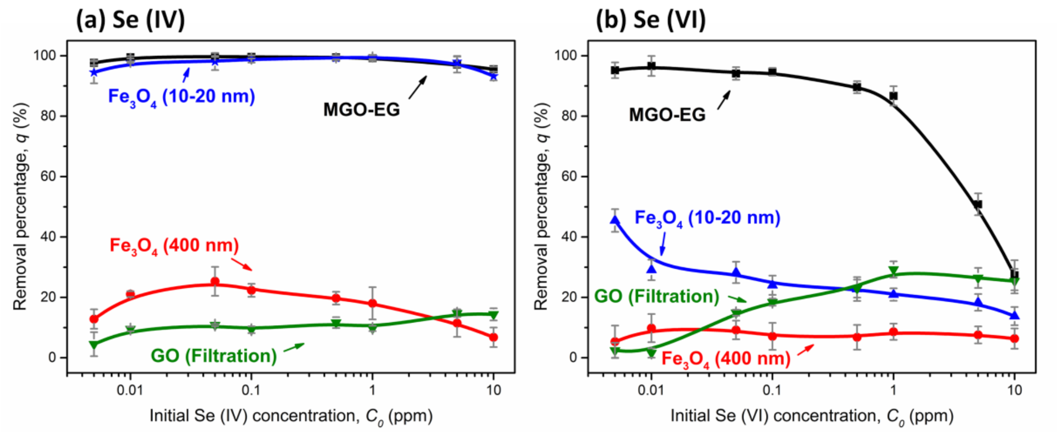

Figure 4-16 Comparison between MGO-EG, GO, pure Fe_3O_4 particles (10 - 20 nm), and pure Fe_3O_4 particles (400 nm) for (a) selenite and (b) selenate adsorption.

4.3.4 Selenium adsorption mechanism with MGO-EG

From the previous discussion, iron oxide is an important functional part of MGO-EG when applied to selenium adsorption. As previously mentioned, iron oxides ores, including magnetite,[12] goethite,[2, 13-16] and hematite[2, 17] were reported effective in selenite removal but performed poor in selenate removal.[39] Mechanism related to the formation of inner-sphere and outer-sphere complexes for selenium adsorption onto iron oxides has been studied in these reports.

Hayes et al.[40] conducted *in situ* Extended X-ray Absorption Fine Structure (EXAFS) measurements on adsorption of selenium at α-FeOOH (goethite)-water interface and indicated that selenite would form a strongly bonded, inner-sphere bidentate complex, while selenate would form a weakly bonded, outer-sphere monodentate hydrated complex. Modelling by Hayes et al.[40, 41] of cation and anion adsorption data concluded that inner-sphere complexes stability do not respond to ionic strength variations while the stability of outer-sphere complexes at a given pH varies with changing ionic strength.

Previous infrared spectroscopy and kinetic studies[16, 42-44] have indicated that strongly bonding anions, such as selenite, adsorb on iron oxides by hydroxyl ligand exchange mechanism and form an inner-sphere complex on iron oxides surface.

Compared with selenite, selenate is a weaker bonding anion, which is expected only to be adsorbed through electrostatic attraction onto iron oxides surface forming an outer-sphere complex with one water molecule between iron oxide surface site and selenate ligand.[40, 43] The outer-sphere is less stable, thus most conventional adsorbents are ineffective to selenate. As discussed previously, GO plays an important role in stabilizing the outer-sphere complex.

When added into selenium solution, surface iron oxides on MGO-EG hydrolyse and create –OH, expressed as (MGO-EG)-OH. Also, there are some remained hydroxyl groups on GO sheets, which are also considered in (MGO-EG)-OH. Based on the previous studies on selenium adsorption with iron oxides, the possible mechanism for selenium removal using MGO-EG is proposed as follows.

for selenite (inner-sphere complex),

$$\text{(MGO-EG)-OH} + SeO_3^{2-} + H^+ \rightarrow \text{(MGO-EG)-}SeO_3^{-} + H_2O \tag{8}$$

for selenate (outer-sphere complex),

$$\text{(MGO-EG)-OH} + SeO_4^{2-} + H^+ \rightarrow \text{(MGO-EG)-}OH_2^{+}\text{-}SeO_4^{2-} \tag{9}$$

The selenium removal percentage-pH curve is in good agreement with the proposed adsorption mechanism and other previous anion adsorption literatures.[45-47] The formation of both inner-sphere and outer-sphere complexes consumes H^+, therefore lower pH would be favourable for the adsorption process. Besides, the removal percentage of selenate decreases faster than that of selenite, which may imply different mechanisms for selenite and selenate adsorption on MGO-EG.

As shown in Figure 4-17, the point of zero charge [pH (PZC)] for MGO-EG is around 3, determined from zeta potential measurements. However, the location of adsorption edge (the sharp discontinuity in the absorption curve) is not necessarily the same with pH (PZC). Since the selenium adsorption free energy is combined with electrostatic interaction and chemical specific adsorption[13] by hydroxyl exchange reaction, the selenium oxyanion (negative charge) adsorption onto MGO-EG can still occur through chemical specific adsorption, even when MGO-EG surface are negative charge. Additionally, surface charge distribution on MGO-EG surface is heterogeneous with negative charges mainly attribute to carboxyl groups on MGO-EG edges and some defects on MGO-EG sheets. Therefore, selenium adsorption could still occur in certain pH range where the average surface charge is negative.

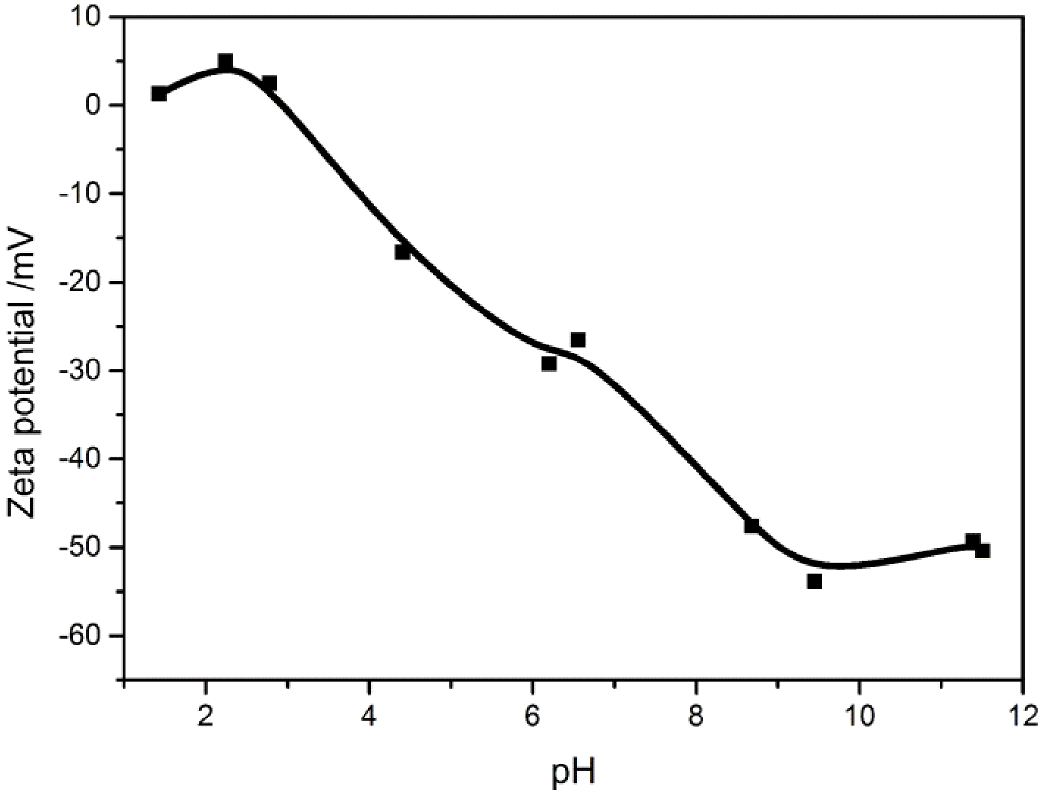

Figure 4-17 Zeta potential of MGO-EG, dispersed in water solution.

4.3.5 MGO-EG recycling tests

Another advantage that MGO-EG adsorbent possesses is that it allows fast separation by an external magnetic field after the adsorption process, which can be recycled for reuse in selenium treatment. Recycling of MGO-EG has also been tested under with the following acid-base treatment. Selenium was desorbed by washing MGO-EG with NaOH (0.1N, pH ~ 13) and reactivated by HCl (0.001 N, pH ~ 3) before reuse. MGO-EG was reused for ten times after freeze-drying under the same adsorption condition (initial selenite and selenate concentration of 300 ppb, MGO-EG dosage 1 g L^{-1}, under natural pH (~ 6), room temperature (RT), and shaking rate 300 rpm for 24 hours). As shown in Figure 4-18, MGO-EG could be reused efficiently for at least ten circles in both selenite and selenate cases.

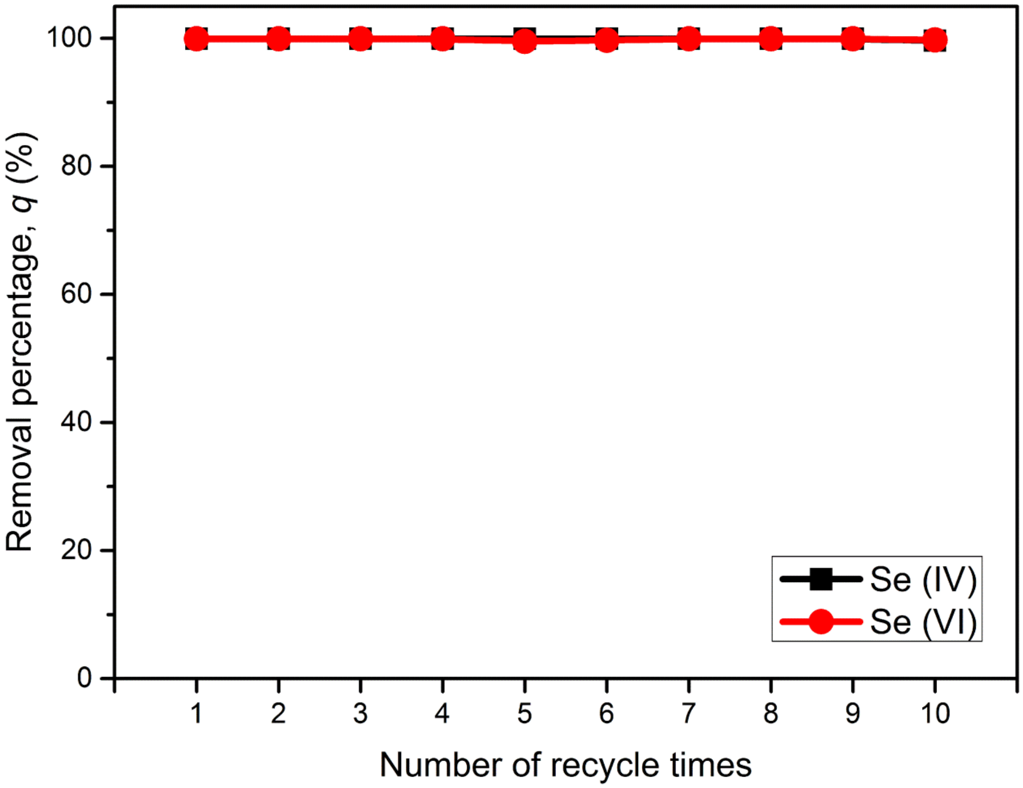

Figure 4-18 Removal percentage of selenium with different recycle times. Recycle was done using acid-washing method. Tests were done at: MGO-EG dosage 1 g L^{-1}, under neutral pH (~ 6), initial selenium concentration 300 ppb, room temperature (~ 25 ℃), shaking rate 300 rpm, adsorption time for 24 hours.

4.3.6 Effects of Interfering ions

4.3.6.1 Effects of Interfering ions of different initial concentrations

The impact of five possible interfering ions (i.e., Ca^{2+}, Mg^{2+}, NO_3^-, SO_4^{2-}, and PO_4^{3-}) on the adsorption of selenium ions by MGO-EG were tested by mixing these individual ion with 300 ppb selenite or selenate solution. Figure 4-19 summarizes the removal percentages of selenite and selenate in the presence of various interfering ions of different initial concentrations, which indicates that the interfering effects of these ions follow the order of: $PO_4^{3-} \approx SO_4^{2-} > Mg^{2+} > Ca^{2+} > NO_3^-$.

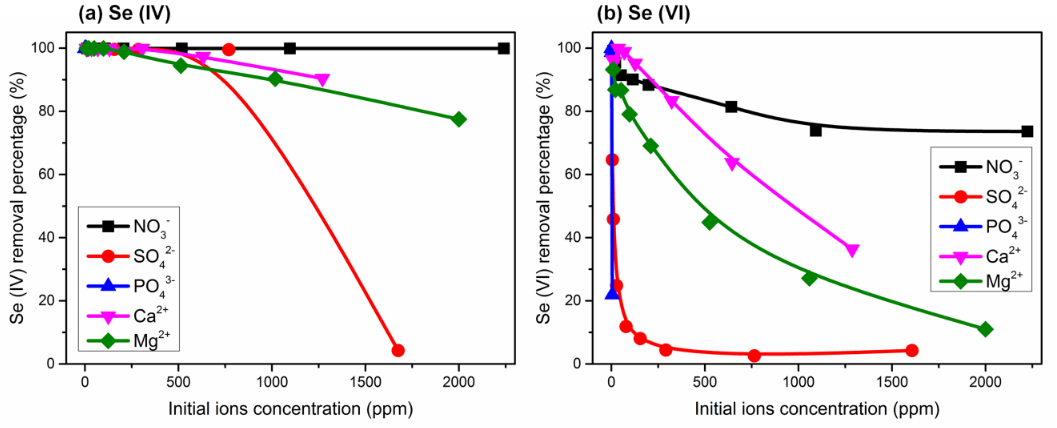

Figure 4-19 Removal percentages of (a) selenite and (b) selenate in the presence of various interfering ions of different initial concentrations. Tests were done at: MGO-EG dosage 1 g L^{-1}, under neutral pH (~ 6), initial selenium concentration 300 ppb, room temperature (~ 25 ℃), shaking rate 300 rpm, adsorption time for 24 hours.

The interfering ions could be partially adsorbed by MGO-EG as well. Figure 4-20, Figure 4-21, Figure 4-22, Figure 4-23, and Figure 4-24 show selenium ion and individual interfering ion removal percentages by MGO-EG with various initial interfering ion concentrations.

Similarly, the interfering ion removal percentage q (%) ions is defined as,

$$q = \frac{C_0 - C}{C_0} \times 100 \tag{10}$$

where C_0 (ppm) is the initial ion (i.e., Ca^{2+}, Mg^{2+}, NO_3^-, SO_4^{2-}, and PO_4^{3-}) concentration, C (ppm) is the equilibrium ion concentration after adsorption.

Figure 4-20 shows selenium and Ca^{2+} removal percentage by MGO-EG with different initial Ca^{2+} concentrations from 0 ppm to ~ 1300 ppm (selenium concentration remains 300 ppb). It is noticed that selenium removal percentage gradually decreases with increasing Ca^{2+} concentration. At initial Ca^{2+} concentration of ~ 1300 ppm, selenite removal percentage decreases from ~ 100 % to ~ 90 %, while selenate removal percentage decrease from ~ 95 % to ~ 40 %. However, trace adsorption of Ca^{2+} by MGO-EG can be observed.

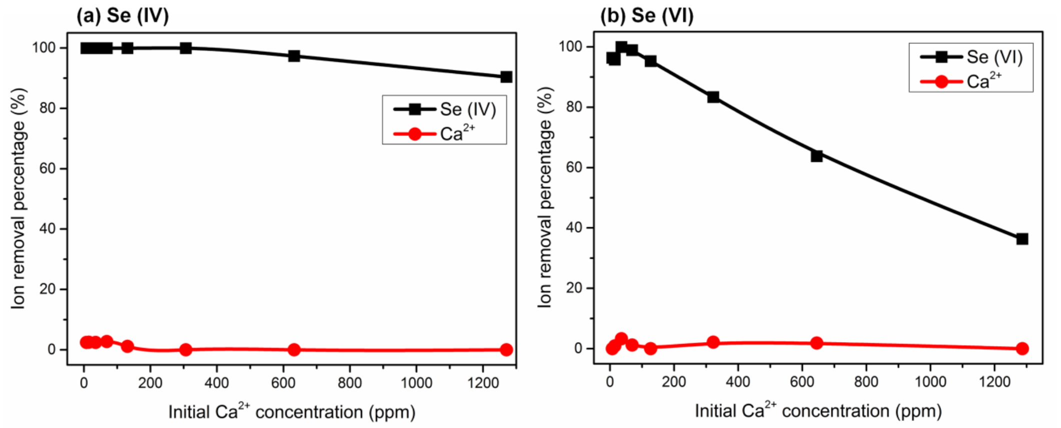

Figure 4-20 Selenium and Ca^{2+} removal percentage by MGO-EG with different initial Ca^{2+} concentrations. Tests were done at: MGO-EG dosage 1 g L^{-1}, under neutral pH (~ 6), initial selenium concentration 300 ppb, room temperature (~ 25 ℃), shaking rate 300 rpm, adsorption time for 24 hours.

Figure 4-21 shows selenium and Mg^{2+} removal percentage by MGO-EG with different initial Mg^{2+} concentrations from 0 ppm to ~ 2000 ppm (selenium concentration remains 300 ppb). It also manifests that selenite removal percentage gradually decreases with increasing Mg^{2+} concentration while selenate removal percentage decrease intensively with increasing Mg^{2+} concentration. At initial Mg^{2+} concentration of ~ 2000 ppm, selenite removal percentage decreases from ~ 100 % to ~ 80 %, while selenate removal percentage decrease from ~ 95 % to ~ 10 %. Similar to Ca^{2+}, only about 2 % adsorption of Mg^{2+} by MGO-EG can be observed.

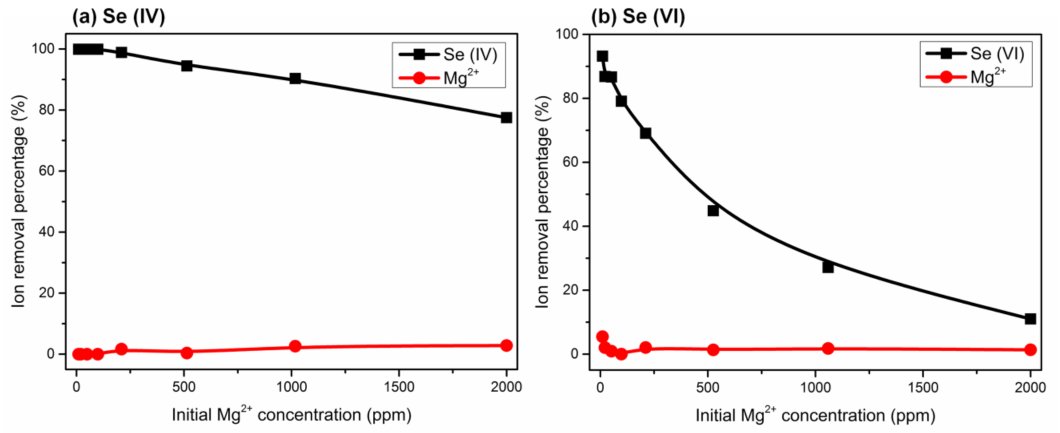

Figure 4-21 Selenium and Mg^{2+} removal percentage by MGO-EG with different initial Mg^{2+} concentrations. Tests were done at: MGO-EG dosage 1 g L^{-1}, under neutral pH (~ 6), initial selenium concentration 300 ppb, room temperature (~ 25 ℃), shaking rate 300 rpm, adsorption time for 24 hours.

Figure 4-22 shows selenium and NO_3^- removal percentage by MGO-EG with different initial NO_3^- concentrations from 0 ppm to ~ 2250 ppm (selenium concentration remains 300 ppb). It is illustrated that NO_3^- would have negligible effect on selenite adsorption and certain influence (20 %, at ~ 2250 ppm) on selenate adsorption. About 5 % adsorption of NO_3^- by MGO-EG can be observed.

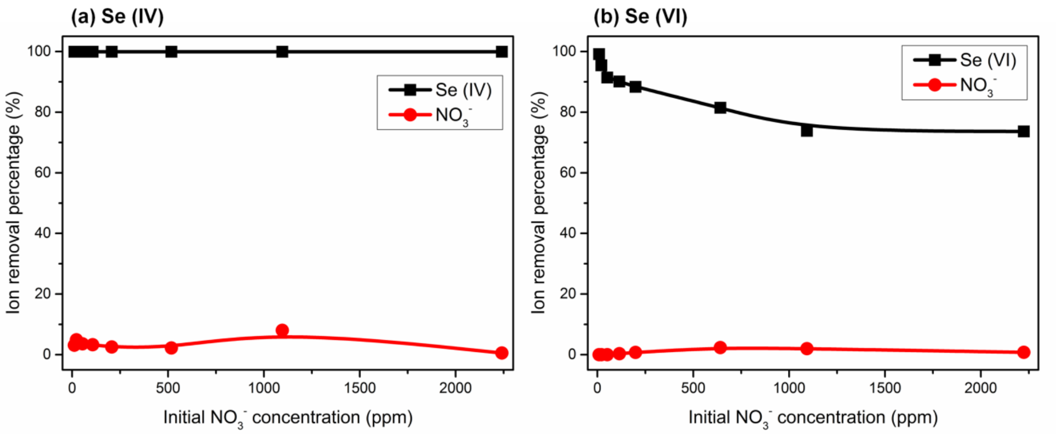

Figure 4-22 Selenium and NO_3^- removal percentage by MGO-EG with different initial NO_3^- concentrations. Tests were done at: MGO-EG dosage 1 g L^{-1}, under neutral pH (~ 6), initial selenium concentration 300 ppb, room temperature (~ 25 ℃), shaking rate 300 rpm, adsorption time for 24 hours.

Ca^{2+} (Figure 4-20), Mg^{2+} (Figure 4-21) and NO_3^- (Figure 4-22) affect selenium removal percentage in similar ways that they have little effect on selenite removal percentage but certain degrees of influence on selenate removal percentage. Moreover, negligible percent of Ca^{2+}, Mg^{2+} and NO_3^- can be adsorbed by MGO-EG. Thus the influence of decreasing selenium removal percentage is possibly due to the increasing ion strength. As mentioned previously that the stability of outer-sphere complex can be notably affected by varying ion strength while inner-sphere complex does not respond to ion strength change.[40, 41]

Figure 4-23 shows selenium and SO_4^{2-} removal percentage by MGO-EG with different initial SO_4^{2-} concentrations from 0 ppm to ~ 1700 ppm (selenium concentration remains 300 ppb). Since sulphur and selenium belong to the same group in the elements periodic table, sulphate has similar structure with selenite and selenate, and similar affinity to MGO-EG bonding sites. As indicated from Figure 4-23, SO_4^{2-} would have obvious effect on selenite removal percentage at concentration > 800 ppm and dramatic influence (95 %, at ~ 2000 ppm) on selenate adsorption, even from low SO_4^{2-} concentrations. It is also concluded that certain amount of SO_4^{2-} (~ 20 % at initial SO_4^{2-} concentration of 1600 ppm) could be adsorbed by MGO-EG. Therefore, SO_4^{2-} can influence the selenium adsorption on MGO-EG not only by varying ion strength but also by competing adsorption on MGO-EG and occupy certain adsorbing sites.

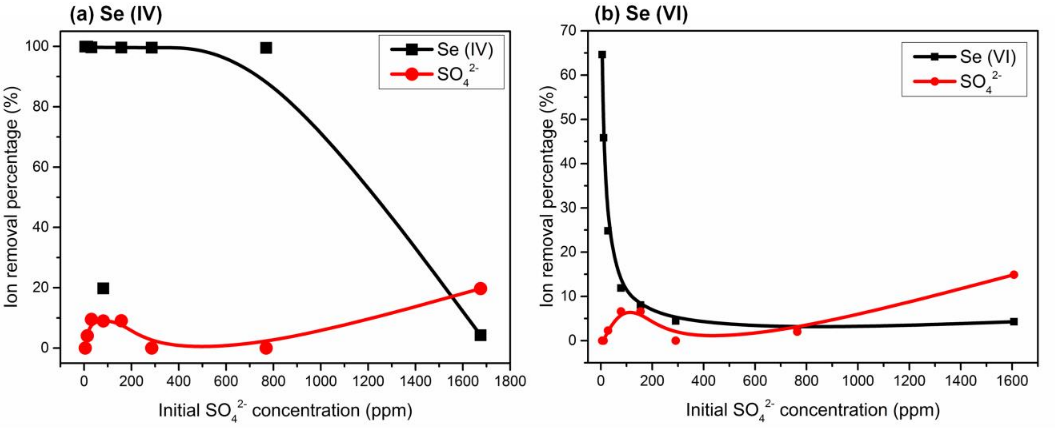

Figure 4-23 Selenium and SO_4^{2-} removal percentage by MGO-EG with different initial SO_4^{2-} concentrations. Tests were done at: MGO-EG dosage 1 g L^{-1}, under neutral pH (~ 6), initial selenium concentration 300 ppb, room temperature (~ 25 ℃), shaking rate 300 rpm, adsorption time for 24 hours.

Figure 4-24 shows selenium and PO_4^{3-} removal percentage by MGO-EG with different initial PO_4^{3-} concentrations from 0 ppm to ~ 1.5 ppm (selenium concentration remains 300 ppb). Phosphate, a strong bonding anion species, is expected to have strong affinity with MGO-EG, with near 100 % removal percentage at PO_4^{3-} concentration of ~ 1.5 ppm. PO_4^{3-} has evident interference on selenate adsorption (selenate removal percentage decreases from 100 % to only 20 %) even with trace PO_4^{3-} concentration (< 2 ppm). PO_4^{3-} influence on selenite removal percentage is negligible within tested initial PO_4^{3-} concentrations, due to the large adsorption ability of MGO-EG.

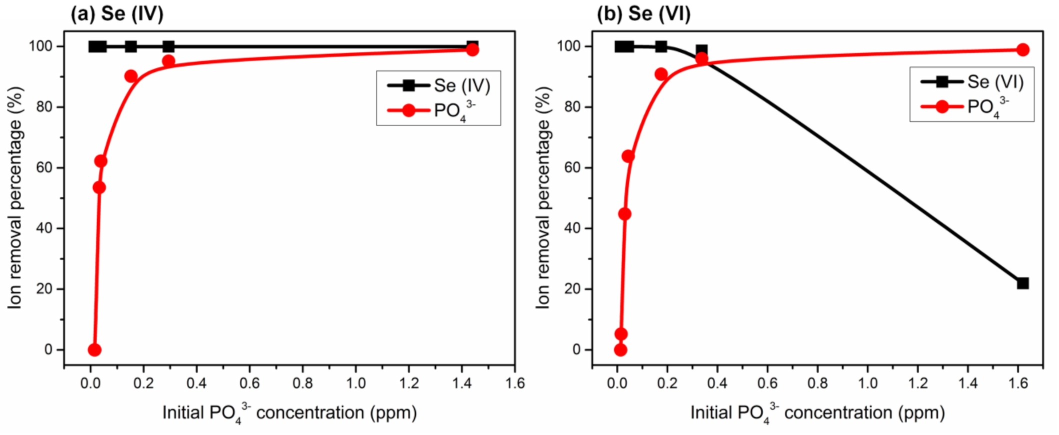

Figure 4-24 Selenium and PO_4^{3-} removal percentage by MGO-EG with different initial PO_4^{3-} concentrations. Tests were done at: MGO-EG dosage 1 g L^{-1}, under neutral pH (~ 6), initial selenium concentration 300 ppb, room temperature (~ 25 ℃), shaking rate 300 rpm, adsorption time for 24 hours.

4.3.6.2 Effects of Interfering ions under different pH

The impact of the five possible interfering ions (i.e., Ca^{2+}, Mg^{2+}, NO_3^-, SO_4^{2-}, and PO_4^{3-}) on the adsorption of selenium ions by MGO-EG under different pH were also conducted, with the results summarized in Figure 4-25. It is demonstrated from the figure that at the same initial interfering ion concentration (20 ppm), the interfering effects of different ions follow the order of: PO_4^{3-} > SO_4^{2-} > Mg^{2+} ≈ Ca^{2+} ≈ NO_3^-. It is also noticed that the selenium removal percentage-pH curves show similar trends with and without the interfering ions: the removal percentage of selenite remains almost 100 % for pH < 10 (in case of PO_4^{3-}, pH < 6) and then drastically drops, while the removal percentage of selenate gradually decreases with increasing pH, which indicates that lower pH facilitates the selenium adsorption on MGO-EG with and without the interfering ions.

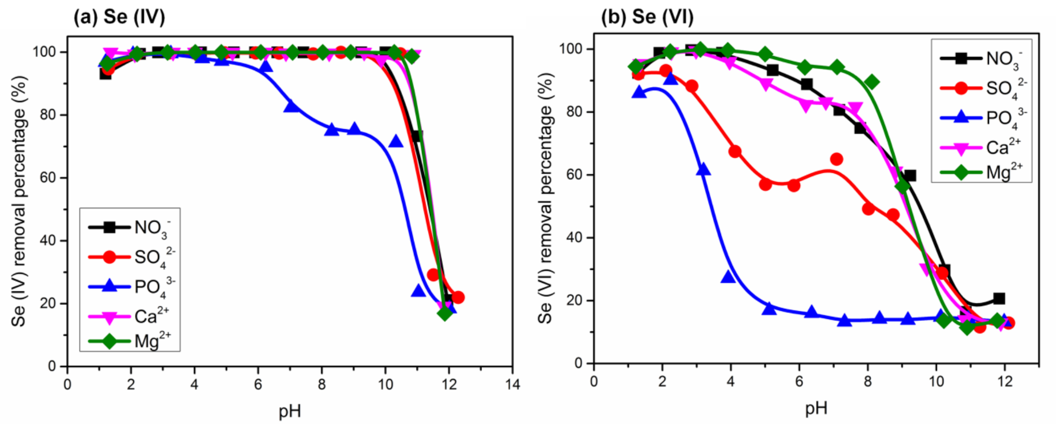

Figure 4-25 Removal percentages of (a) selenite and (b) selenate in the presence of various interfering ions at different pH. Tests were done at: MGO-EG dosage 1 g L^{-1}, initial selenium concentration 300 ppb, initial interfering ions concentration 20 ppm, room temperature (~ 25 ℃), shaking rate 300 rpm, adsorption time for 24 hours.

Interfering ions removal percentage by MGO-EG were measured individually under different pH.

Ca^{2+} (Figure 4-26) and Mg^{2+} (Figure 4-27) demonstrate similar trends under different pH at the same initial ion concentration (20 ppm). Ca^{2+} and Mg^{2+} barely have any adsorption by MGO-EG when pH < ~ 9, while they are strongly removed probably by Ca^{2+} and Mg^{2+} precipitation at high pH value.

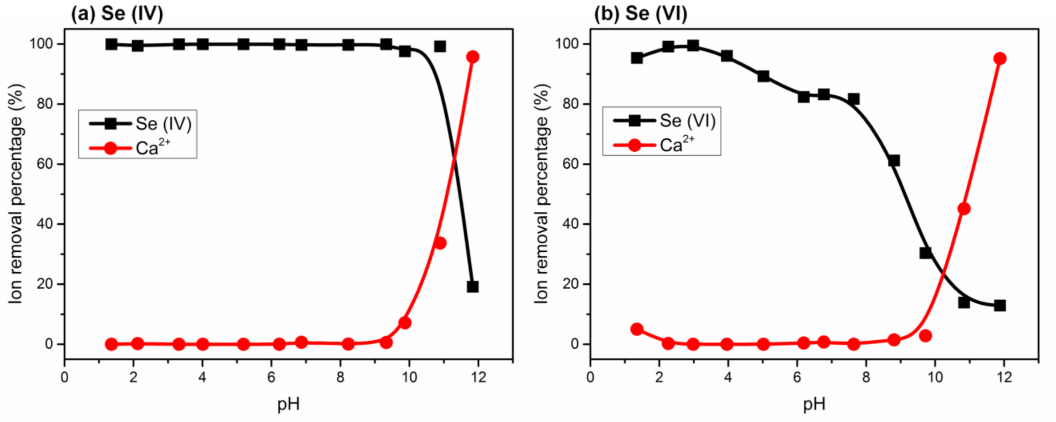

Figure 4-26 Selenium and Ca^{2+} removal percentage by MGO-EG with different pH. Tests were done at: MGO-EG dosage 1 g L^{-1}, initial selenium concentration 300 ppb, room temperature (~ 25 ℃), shaking rate 300 rpm, adsorption time for 24 hours.

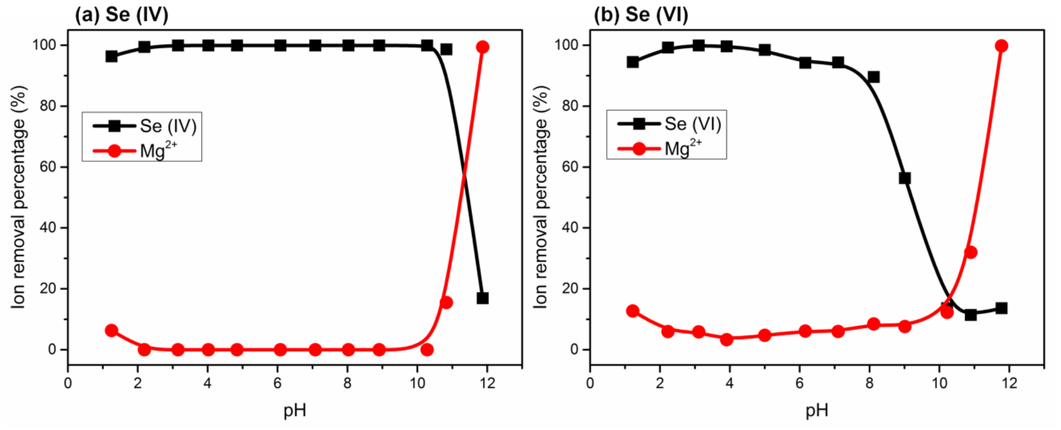

Figure 4-27 Selenium and Mg^{2+} removal percentage by MGO-EG with different pH. Tests were done at: MGO-EG dosage 1 g L^{-1}, initial selenium concentration 300 ppb, room temperature (~ 25 ℃), shaking rate 300 rpm, adsorption time for 24 hours.

NO_3^- (Figure 4-28) only show little adsorption (< 20 %) on MGO-EG with varying pH. However, NO_3^- can still impact the selenium, especially selenate, adsorption on MGO-EG possibly by changing the ion strength of the solution.

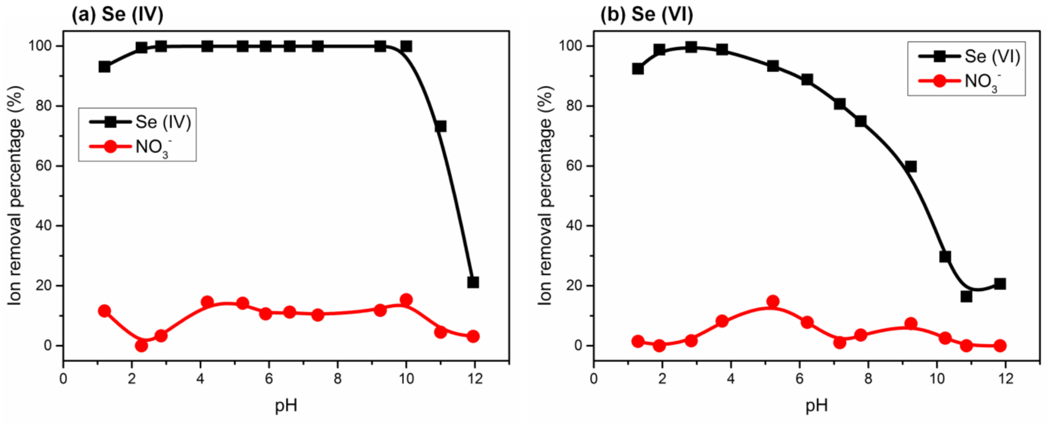

Figure 4-28 Selenium and NO_3^- removal percentage by MGO-EG with different pH. Tests were done at: MGO-EG dosage 1 g L^{-1}, initial selenium concentration

300 ppb, room temperature (~ 25 ℃), shaking rate 300 rpm, adsorption time for 24 hours.

As is shown in Figure 4-29, SO_4^{2-} and selenium ions compete while both of their adsorption of MGO-EG can be weakened by increasing pH.

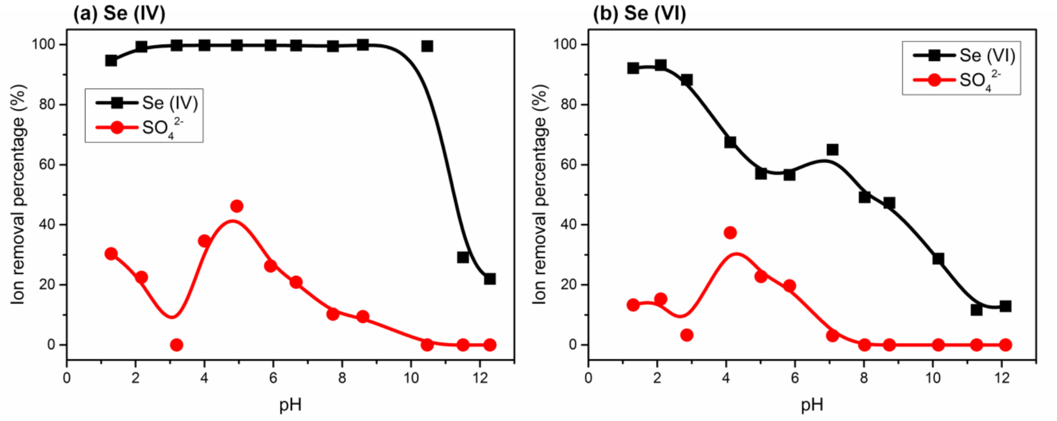

Figure 4-29 Selenium and SO_4^{2-} removal percentage by MGO-EG with different pH. Tests were done at: MGO-EG dosage 1 g L^{-1}, initial selenium concentration 300 ppb, room temperature (~ 25 ℃), shaking rate 300 rpm, adsorption time for 24 hours.

The strong interfering ion, PO_4^{3-} (Figure 4-30), can reach a nearly complete adsorption by MGO-EG at pH ~ 2 and then weakened by increasing pH. The selenate removal percentage is distinctly interference by PO_4^{3-} that the adsorption edge (the dramatic decrease) is pH ~ 2.

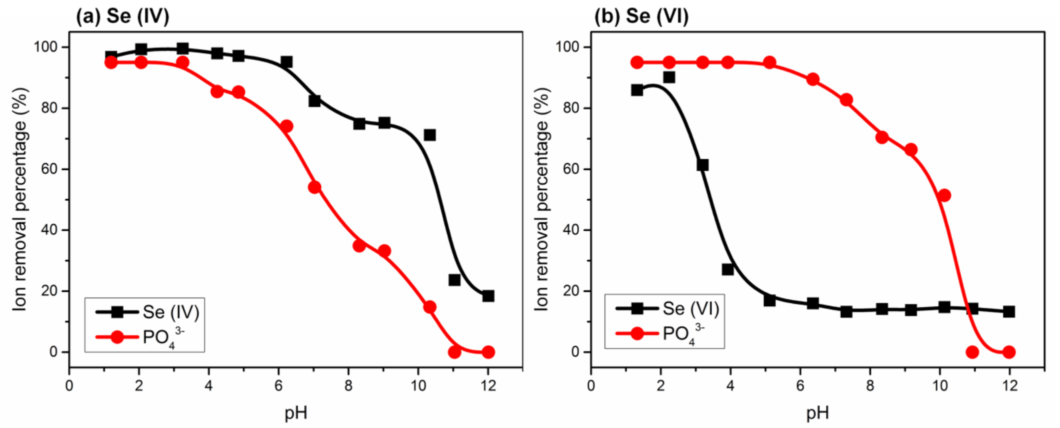

Figure 4-30 Selenium and PO_4^{3-} removal percentage by MGO-EG with different pH. Tests were done at: MGO-EG dosage 1 g L^{-1}, initial selenium concentration 300 ppb, room temperature (~ 25 ℃), shaking rate 300 rpm, adsorption time for 24 hours.

4.4 Conclusions

Selenium pollution through aqueous media has been a serious problem globally. Although effective for selenite removal, conventional adsorbents typically can remove less than 50 % of selenate. To effectively adsorb selenate, the major selenium specious in water, as well as selenite, a novel adsorbent MGO-EG has been synthesized and characterized. MGO-EG thesis process includes the oxidation of graphite GO and a high temperature solution reaction for magnetic particle deposition. AFM, TEM and SEM characterization results provided the observation of abundant magnetic particles (with an average particle size of ~ 10 nm) dispersed uniformly on GO monolayers. XRD, XPS and FTIR characterizations confirm the chemical composition and structure of MGO-EG. Significant high selenium removal percentage was achieved with selenium water solutions (> 99.9 % for selenite and ~ 95 % for selenate) in only about ten seconds. In acidic condition (pH ~ 2), the removal percentages for both selenite and selenate can reach > 99.9 %. MGO-EG remains the same selenium adsorption efficiency for at least ten times of recycles. Its high selenium removal efficiency indicates the potential use of MGO-EG for industry water treatment.

4.5 References

[1] W. H. Organization, Guidelines for Drinking-water Quality. **2011**.

[2] M. Rovira, J. Giménez, M. Martínez, X. Martínez-Lladó, J. de Pablo, V. Marti, L. Duro, Sorption of selenium (IV) and selenium (VI) onto natural iron oxides: goethite and hematite. *Journal of hazardous materials*. **2008**, *150,* 279.

[3] F. M. Fordyce, *Selenium deficiency and toxicity in the environment*, Springer, **2013**.

[4] L. Twidwell, "The Removal of Arsenic, Selenium and Metals from Aqueous Solution by Iron Precipitation and Reduction Techniques", presented at *TMS2011 Annual Meeting, San Diego, CA*, 2011.

[5] K. C. Kemp, H. Seema, M. Saleh, K. Mahesh, V. Chandra, K. S. Kim, Environmental applications using graphene composites: water remediation and gas adsorption. *Nanoscale*. **2013**.

[6] V. Chandra, J. Park, Y. Chun, J. W. Lee, I.-C. Hwang, K. S. Kim, Water-dispersible magnetite-reduced graphene oxide composites for arsenic removal. *ACS nano*. **2010**, *4,* 3979.

[7] A. Y. Romanchuk, A. S. Slesarev, S. N. Kalmykov, D. V. Kosynkin, J. M. Tour, Graphene oxide for effective radionuclide removal. *Physical Chemistry Chemical Physics*. **2013**, *15*, 2321.

[8] Z. Niu, J. Chen, H. H. Hng, J. Ma, X. Chen, A leavening strategy to prepare reduced graphene oxide foams. *Advanced Materials*. **2012**, *24*, 4144.

[9] F. Liu, S. Chung, G. Oh, T. S. Seo, Three-dimensional graphene oxide nanostructure for fast and efficient water-soluble dye removal. *ACS Applied Materials & Interfaces*. **2012**, *4*, 922.

[10] M. Z. Iqbal, A. A. Abdala, Oil spill cleanup using graphene. *Environmental Science and Pollution Research*. **2012**, 1.

[11] F. Ahme, D. F. Rodrigues, Investigation of acute effects of graphene oxide on wastewater microbial community: A case study. *Journal of hazardous materials*. **2013**.

[12] M. Martinez, J. Gimenez, J. De Pablo, M. Rovira, L. Duro, Sorption of selenium (IV) and selenium (VI) onto magnetite. *Applied surface science*. **2006**, *252*, 3767.

[13] L. S. Balistrieri, T. Chao, Selenium adsorption by goethite. *Soil Science Society of America Journal*. **1987**, *51*, 1145.

[14] P. Zhang, D. L. Sparks, Kinetics of selenate and selenite adsorption/desorption at the goethite/water interface. *Environmental science & technology*. **1990**, *24*, 1848.

[15] M. Duc, G. Lefevre, M. Fedoroff, J. Jeanjean, J. Rouchaud, F. Monteil-Rivera, J. Dumonceau, S. Milonjic, Sorption of selenium anionic species on

apatites and iron oxides from aqueous solutions. *Journal of environmental radioactivity*. **2003**, *70*, 61.

[16] R. Parfitt, J. Russell, Adsorption on hydrous oxides. IV. Mechanisms of adsorption of various ions on goethite. *Journal of Soil Science*. **1977**, *28*, 297.

[17] M. Duc, G. Lefevre, M. Fédoroff, Sorption of selenite ions on hematite. *Journal of colloid and interface science*. **2006**, *298*, 556.

[18] W. Lv, D.-M. Tang, Y.-B. He, C.-H. You, Z.-Q. Shi, X.-C. Chen, C.-M. Chen, P.-X. Hou, C. Liu, Q.-H. Yang, Low-temperature exfoliated graphenes: vacuum-promoted exfoliation and electrochemical energy storage. *Acs Nano*. **2009**, *3*, 3730.

[19] S.-M. Paek, E. Yoo, I. Honma, Enhanced cyclic performance and lithium storage capacity of SnO2/graphene nanoporous electrodes with three-dimensionally delaminated flexible structure. *Nano Letters*. **2008**, *9*, 72.

[20] S. Stankovich, D. A. Dikin, R. D. Piner, K. A. Kohlhaas, A. Kleinhammes, Y. Jia, Y. Wu, S. T. Nguyen, R. S. Ruoff, Synthesis of graphene-based nanosheets via chemical reduction of exfoliated graphite oxide. *Carbon*. **2007**, *45*, 1558.

[21] R. Anthony, John Wiley & Sons, **1984**.

[22] C. Hontoria-Lucas, A. Lopez-Peinado, J. d. D. López-González, M. Rojas-Cervantes, R. Martin-Aranda, Study of oxygen-containing groups in a series of graphite oxides: physical and chemical characterization. *Carbon*. **1995**, *33*, 1585.

[23] H. He, T. Riedl, A. Lerf, J. Klinowski, Solid-state NMR studies of the structure of graphite oxide. *The Journal of Physical Chemistry*. **1996**, *100*, 19954.

[24] A. Lerf, H. He, M. Forster, J. Klinowski, Structure of graphite oxide revisited. *The Journal of Physical Chemistry B*. **1998**, *102*, 4477.

[25] H. He, J. Klinowski, M. Forster, A. Lerf, A new structural model for graphite oxide. *Chemical physics letters*. **1998**, *287*, 53.

[26] Y. Xue, H. Chen, D. Yu, S. Wang, M. Yardeni, Q. Dai, M. Guo, Y. Liu, F. Lu, J. Qu, Oxidizing metal ions with graphene oxide: the in situ formation of magnetic nanoparticles on self-reduced graphene sheets for multifunctional applications. *Chemical Communications*. **2011**, *47*, 11689.

[27] J. Shen, M. Shi, H. Ma, B. Yan, N. Li, M. Ye, Hydrothermal synthesis of magnetic reduced graphene oxide sheets. *Materials Research Bulletin*. **2011**, *46*, 2077.

[28] J. Shen, Y. Hu, M. Shi, N. Li, H. Ma, M. Ye, One Step Synthesis of Graphene Oxide− Magnetic Nanoparticle Composite. *The Journal of Physical Chemistry C*. **2010**, *114*, 1498.

[29] H. Deng, X. Li, Q. Peng, X. Wang, J. Chen, Y. Li, Monodisperse Magnetic Single ‐ Crystal Ferrite Microspheres. *Angewandte Chemie*. **2005**, *117*, 2842.

[30] F. He, J. Fan, D. Ma, L. Zhang, C. Leung, H. L. Chan, The attachment of Fe3O4 nanoparticles to graphene oxide by covalent bonding. *Carbon*. **2010**, *48*, 3139.

[31] X. Yang, X. Zhang, Y. Ma, Y. Huang, Y. Wang, Y. Chen, Superparamagnetic graphene oxide–Fe3O4 nanoparticles hybrid for controlled targeted drug carriers. *Journal of Materials Chemistry*. **2009**, *19*, 2710.

[32] B. Konkena, S. Vasudevan, Understanding Aqueous Dispersibility of Graphene Oxide and Reduced Graphene Oxide through p K a Measurements. *The Journal of Physical Chemistry Letters*. **2012**, *3*, 867.

[33] K. Zhou, Y. Zhu, X. Yang, C. Li, One-pot preparation of graphene/Fe3O4 composites by a solvothermal reaction. *New Journal of Chemistry*. **2010**, *34*, 2950.

[34] H. Freundlich, Über die adsorption in lösungen. *Engelmann, Leipzig*. **1906**.

[35] N. Ahalya, R. Kanamadi, T. Ramachandra, Biosorption of chromium (VI) from aqueous solutions by the husk of Bengal gram (Cicer arientinum). *Electronic Journal of Biotechnology*. **2005**, *8*, 0.

[36] K. a. N. KADIRVELU, C., Agricultural by-products as metal adsorbents: sorption of lead (II) from aqueous solutions onto coir-pith carbon. *Environmental Technology*. **2000**, *21*, 1091.

[37] R. López de Arroyabe Loyo, S. I. Nikitenko, A. C. Scheinost, M. Simonoff, Immobilization of selenite on Fe3O4 and Fe/Fe3C ultrasmall particles. *Environmental science & technology*. **2008**, *42*, 2451.

[38] D. R. Eaton, Outer sphere complexes as intermediates in coordination chemistry. *Reviews of chemical intermediates*. **1988**, *9*, 201.

[39] S. Shin, J. Jang, Thiol containing polymer encapsulated magnetic nanoparticles as reusable and efficiently separable adsorbent for heavy metal ions. *Chemical Communications*. **2007**, 4230.

[40] K. F. Hayes, A. L. Roe, G. E. BROWN JR, K. O. Hodgson, J. O. Leckie, G. A. Parks, In situ X-ray absorption study of surface complexes: Selenium oxyanions on α-FeOOH. *Science*. **1987**, *238*, 783.

[41] K. F. Hayes, C. Papelis, J. O. Leckie, Modeling ionic strength effects on anion adsorption at hydrous oxide/solution interfaces. *Journal of Colloid and Interface Science*. **1988**, *125*, 717.

[42] D. Yates, T. Healy, Mechanism of anion adsorption at the ferric and chromic oxide/water interfaces. *Journal of Colloid and Interface Science*. **1975**, *52*, 222.

[43] J. B. Harrison, V. E. Berkheiser, Anion interactions with freshly prepared hydrous iron oxides. *Clays Clay Miner*. **1982**, *30*, 97.

[44] R. Cornell, P. Schindler, Infrared study of the adsorption of hydroxycarboxylic acids onα-FeOOH and amorphous Fe (III) hydroxide. *Colloid and Polymer Science*. **1980**, *258*, 1171.

[45] L. S. Balistrieri, T. Chao, Adsorption of selenium by amorphous iron oxyhydroxide and manganese dioxide. *Geochimica et Cosmochimica Acta*. **1990**, *54*, 739.

[46] M. M. Benjamin, K. F. Hayes, J. O. Leckie, Removal of toxic metals from power-generation waste streams by adsorption and coprecipitation. *Journal (Water Pollution Control Federation)*. **1982**, 1472.

[47] F. HINGTON, A. Posner, J. Quirk, Adsorption of selenite by goethite. **1968**.

Chapter 5 Conclusions and Future Work

5.1 Conclusions

Selenium enrichment is becoming a global environmental problem. Typically only < 50 %[1] selenate could be efficiently removal. This work applied graphene oxide-magnetic iron oxide to selenium ions removal from laboratory simulated water for the first time and obtained significant selenium removal percentage (> 99.9 % for selenite with both MGO and MGO-EG; ~ 80 % with MGO for selenate and ~ 95 % for selenate with MGO-EG) within only ten seconds. This study inspires new ideas of selenium removal from practical wastewater.

The major discoveries and conclusions in this study are summarized as follows:

1) Magnetic Particle-Graphene Oxide Composites (MGO) and Magnetic Particle-Graphene Oxide Composites reduced by Ethylene Glycol (MGO-EG) were synthesized by the two-step method: oxidation of graphite to Graphene Oxide (GO) with a modified Hummers method;[2] and the novel high temperature solution reaction for magnetic particle deposition. The products from these methods are reliable.

2) GO, MGO and MGO-EG were characterized with XRD, FTIR, XPS, AFM, TEM, SEM, TGA, etc for their chemical compositions and surface morphologies. AFM, TEM and SEM results provided the observation of abundant magnetic particles (with an average particle size of ~ 10 nm) dispersed uniformly on GO monolayers. XRD, XPS and FTIR characterizations confirm the chemical

composition and structure of MGO and MGO-EG. Further magnetic property tests show the saturation magnetization of 13.47 emu g^{-1} for MGO and 49.7 emu g^{-1} for MGO-EG, indicating the better magnetic properties with the addition of EG. The excellent magnetic properties further guaranteed the success of magnetic separation.

3) In selenium ion adsorption, the MGO and MGO-EG composites show efficient and high binding capacity for selenite and selenate, with removal percentage for selenite (> 99.9 %) and selenate (~ 80 % with MGO, ~ 95 % with MGO-EG) within only ten seconds. With the addition of EG, MGO-EG shows higher adsorption capacity than MGO.

4) Selenium adsorption conditions can impact the removal percentage of MGO and MGO-EG. Acidic pH enhances the adsorption of Selenium ions on MGO and MGO-EG. The removal percentage of selenate increases to > 95 % at pH ~ 2 with MGO and to > 99.9 % with MGO-EG. The selenium adsorption process with MGO and MGO-EG only take ten seconds, while reported adsorbents normally take hours.[3-6] Lower temperature favors selenate adsorption on MGO-EG, while the temperature difference is minor (~ 10 %), while there is negligible change of removal percentage for selenite within the temperature studied (4 ^{o}C – 80 ^{o}C).

5) Both MGO and MGO-EG can be stripped (by washing with alkali) and reused (by reactivated with acid). The selenium removal ability remains almost the same within ten recycles.

6) Potential interfering ions (NO_3^-, SO_4^{2-}, PO_4^{3-}, Ca^{2+}, and Mg^{2+}) effect were evaluated with selenium adsorption by MGO-EG under different interfering ions concentrations and various pH values. It was concluded that at natural pH, the interfering effects among different ions are: $PO_4^{3-} \approx SO_4^{2-} > Mg^{2+} > Ca^{2+} > NO_3^-$; while at the same initial concentration (20 ppm), the interfering effects among different ions are: $PO_4^{3-} > SO_4^{2-} > Mg^{2+} \approx Ca^{2+} \approx NO_3^-$.

7) Comparison between MGO/MGO-EG, pure iron oxide (with two different particle diameter: 10 - 20 nm and 400 nm), and GO indicated that iron oxide is the main adsorbing part, especially in selenite adsorption; GO plays an important role in selenate adsorption; the 10 – 20 nm iron oxide particles have better adsorption ability than the 400 nm iron oxide.

8) Possible mechanism was proposed for MGO and MGO-EG synthesis and the selenium adsorption process. Selenite and selenate are adsorption on MGO and MGO-EG with the formation of inner-sphere complex and outer-sphere complex, respectively. The outer-sphere complex is less stable, which may explain why selenate is much more difficult to be adsorbed by normal adsorbents, such as iron oxides. With this better understanding of the adsorption reaction process, more potential progress can be made to improve the adsorption capacity and further benefit the public.

9) Furthermore, MGO-EG was applied in mine impacted water as a preliminary test in complicated ions environment. Two different water samples are used in this study (Sample A and B) each with approximate selenium concentration of ~ 300 ppb with other interfering ion (~ 60 ppm NO_3^-, ~ 2000

SO_4^{2-}, ~ 5 ppb PO_4^{3-}, ~ 40 ppm Ca^{2+}, ~ 20 ppm Mg^{2+}). 67% selenium removal was obtained for Sample A and 42% selenium removal was obtained from sample B, both at pH ~ 2. A key difference in the samples is the alkalinity (pH of sample A ~ 7.74, pH of sample B ~ 8.33), which possibly explains the difference between the two different removal percentages. Although the preliminary selenium removal percentages are not as impressive as the laboratory simulated water, it is still promising to enhance the selenium removal percentage by adjusting the MGO-EG dosage, pH value, interfering ions pre-removal, etc.

In summary, our results show that MGO and MGO-EG composites have excellent removal capability of selenite and selenate in aqueous solutions which can be used for practical applications in removal of selenium ions.

5.2 Future Work

5.2.1 Adsorption mechanism study with EXAFS (Extended X-ray Absorption Fine Structure)

A monochromatic X-ray beam is focused on the sample (Figure 5-1). The photon energy of the X-rays is gradually increased so that it can traverse one of the absorption edges of the elements that the sample contains. Below the absorption edge, the photons cannot excite the electrons of the relevant atomic level and thus absorption is low. However, when the photon energy is just sufficient to excite the electrons, a large increase in absorption occurs, known as the absorption edge. The resulting photoelectrons have a lower kinetic energy and can be backscattered by the neighboring atoms of the emitting atom. The probability of backscattering is dependent on the photoelectrons energy. The backscattering of the photoelectron affects whether the X-ray photon is absorbed in the first place. Therefore, the possibility of X-ray absorption will depend on the photon energy, since the photoelectron energy will depend on the photon energy. The net effect is a series of oscillations on the high photon energy side of the absorption edge. These oscillations can be used to determine the atomic number, distance and coordination number of the neighboring atoms of the X-ray aimed element. Moreover, synchrotron radiation is applied in EXAFS experiments, since it is necessary to scan with all the photon energies.[7-9]

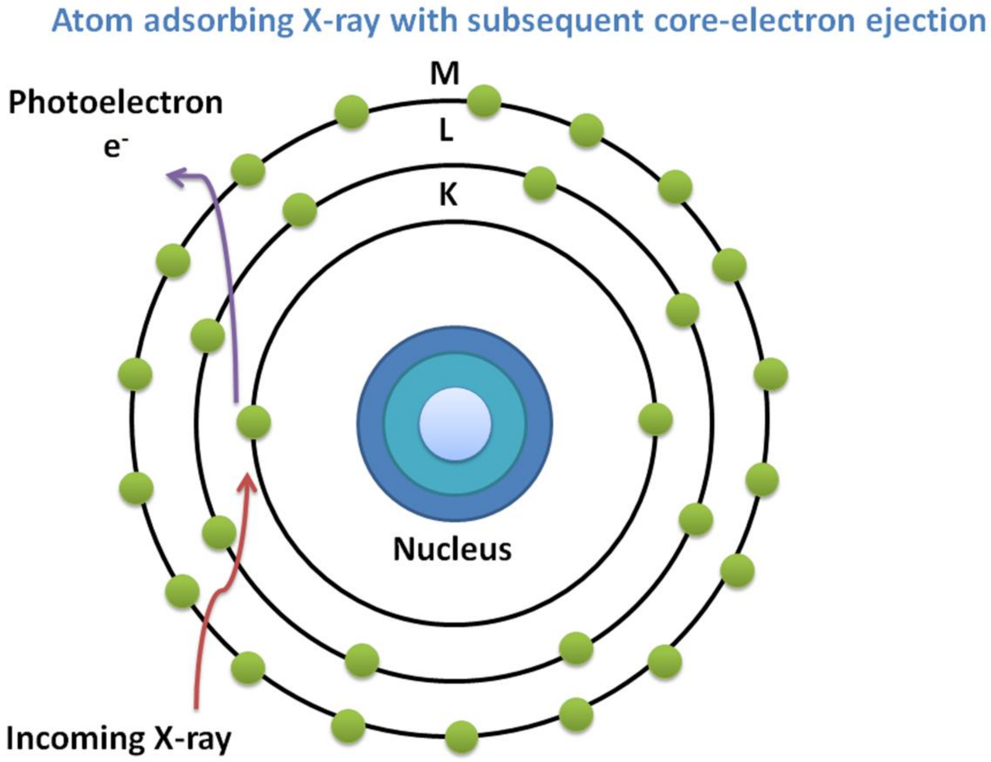

Figure 5-1 The wave vector of a photoelectron.[8]

With EXAFS, it is possible to determine the exact adsorbing site on MGO/MGO-EG, since EXAFS could provide the information of the neighboring atom, the coordination number, and distance between atoms. EXAFS is not limited to crystals, which could extend EXAFS to wilder applications (in this thesis, the crystallinity of GO is poor). EXAFS could provide a better explanation of the inner-sphere and outer-sphere complexes mode by accurate molecular model fitting.

---

[8] Figure5-1 is adapted from ChemWiki-UC Davis (http://chemwiki.ucdavis.edu/Physical_Chemistry/Spectroscopy/X-ray_Spectroscopy/XAS%3A_Theory)

5.2.2 Surface properties and interaction using AFM and SFA

Inspired by the interesting surface properties of GO, MGO, and MGO-EG, a completed study focusing on the surface properties and interaction by AFM and SFA (Surface Force Apparatus) would benefit the basic surface science study and further contribute to the surface modification of graphene related materials.

As discussed previously, AFM could be used to measure the surface roughness, and image the morphology of GO, MGO, and MGO-EG.

SFA can be used to measure the physical forces between GO-GO and MGOs-MGOs surfaces, including van der Waals, electrostatic forces, adhesion and capillary forces, and friction forces with a distance resolution of less than 1Å.[10] Incorporation of other techniques, such as x-ray scattering, IR spectroscopy, fluorescence microscopy and AFM, allows for different measurements to be made on a sample at the same time.

It operates on one central simple-cantilever spring to generate both coarse and fine motions over a total range of 7 orders of magnitude (from millimeters to ångstroms). The normal forces, for example, can be calculated by equation,[11]

$$\Delta F(D) = k(D_{applied} - D_{meas}) \qquad (1)$$

Though SFA has already been utilized for studying various types of tribological and rheological systems and materials such as nanoparticles, polymers, hydrocarbons, polysaccharides, biological materials, self-assembled monolayers, dye molecules and metal thin films, study of graphene-related materials using SFA has not been reported yet.[10] SFA could be applied to study the surface integrations between GO, MGO and MGO-EG in air; GO, MGO and

MGO-EG interaction with water; and MGO and MGO-EG interaction with selenium water solution.

5.2.3 Interfering ions control

Consider the selenium oxyanions removal effected by interfering ions, as discussed in the previous chapters, the interfering ions control would be reasonable future work. Attention should be paid especially on CRO and FRO water tests with interfering ions pretreatment. Highly interfering ions (SO_4^{2-}, PO_4^{3-}, etc.) should be pre-treated either by adsorption with low priced adsorbent (eg. activated carbon), ion exchange resin, precipitation, ion flotation, or reverse osmosis.[1]

Future work will focus on the effect of interfering ions with different ion strength at different pH and the affectivity of different pretreatment methods. The combination of different treatment methods and the total cost will also be considered.

5.2.4 Universal adsorption potential for other heavy metal ions (Cr^{2+}, Pb^{2+} ,Zn^{2+}, As, Hg^{2+}, Cu^{2+}, etc.) and organic dyes

According to the previous literature review[12-17] and adsorption data, a wider application for heavy metal ions by MGO/MGO-EG is promising. Exploration of more possible ion species removal would indicate the feasibility of using MGO/MGO-EG as a universal ion adsorbent in the industry.

5.3 References

[1] L. Twidwell, "The Removal of Arsenic, Selenium and Metals from Aqueous Solution by Iron Precipitation and Reduction Techniques", presented at *TMS2011 Annual Meeting, San Diego, CA*, 2011.

[2] W. Lv, D.-M. Tang, Y.-B. He, C.-H. You, Z.-Q. Shi, X.-C. Chen, C.-M. Chen, P.-X. Hou, C. Liu, Q.-H. Yang, Low-temperature exfoliated graphenes: vacuum-promoted exfoliation and electrochemical energy storage. *Acs Nano*. **2009**, *3*, 3730.

[3] M. Duc, G. Lefevre, M. Fédoroff, Sorption of selenite ions on hematite. *Journal of colloid and interface science*. **2006**, *298*, 556.

[4] M. Martinez, J. Gimenez, J. De Pablo, M. Rovira, L. Duro, Sorption of selenium (IV) and selenium (VI) onto magnetite. *Applied surface science*. **2006**, *252*, 3767.

[5] R. López de Arroyabe Loyo, S. I. Nikitenko, A. C. Scheinost, M. Simonoff, Immobilization of selenite on Fe3O4 and Fe/Fe3C ultrasmall particles. *Environmental science & technology*. **2008**, *42*, 2451.

[6] M. Rovira, J. Giménez, M. Martínez, X. Martínez-Lladó, J. de Pablo, V. Marti, L. Duro, Sorption of selenium (IV) and selenium (VI) onto natural iron oxides: goethite and hematite. *Journal of hazardous materials*. **2008**, *150*, 279.

[7] B. K. Teo, D. C. Joy, *EXAFS spectroscopy: techniques and applications*, Plenum Press New York, **1981**.

[8] B. K. Teo, *EXAFS: basic principles and data analysis*, Vol. 9, Springer-Verlag Berlin, **1986**.

[9] D. Koningsberger, R. Prins, X-ray absorption: principles, applications, techniques of EXAFS, SEXAFS and XANES. **1987**.

[10] J. Israelachvili, Y. Min, M. Akbulut, A. Alig, G. Carver, W. Greene, K. Kristiansen, E. Meyer, N. Pesika, K. Rosenberg, Recent advances in the surface forces apparatus (SFA) technique. *Reports on Progress in Physics*. **2010**, *73*, 036601.

[11] J. Israelachvili, Thin film studies using multiple-beam interferometry. *Journal of Colloid and Interface Science*. **1973**, *44*, 259.

[12] V. Chandra, J. Park, Y. Chun, J. W. Lee, I.-C. Hwang, K. S. Kim, Water-dispersible magnetite-reduced graphene oxide composites for arsenic removal. *ACS nano*. **2010**, *4*, 3979.

[13] C. Wang, C. Feng, Y. Gao, X. Ma, Q. Wu, Z. Wang, Preparation of a graphene-based magnetic nanocomposite for the removal of an organic dye from aqueous solution. *Chemical Engineering Journal*. **2011**, *173*, 92.

[14] K. Takai, T. Suzuki, T. Enoki, H. Nishihara, T. Kyotani, Structure and magnetic properties of curved graphene networks and the effects of bromine and potassium adsorption. *Physical Review B*. **2010**, *81*, 205420.

[15] G. Xie, P. Xi, H. Liu, F. Chen, L. Huang, Y. Shi, F. Hou, Z. Zeng, C. Shao, J. Wang, A facile chemical method to produce superparamagnetic graphene oxide–Fe3O4 hybrid composite and its application in the removal of dyes from aqueous solution. *Journal of Materials Chemistry*. **2012**, *22*, 1033.

[16] J. Li, S. Zhang, C. Chen, G. Zhao, X. Yang, J. Li, X. Wang, Removal of Cu (II) and fulvic acid by graphene oxide nanosheets decorated with Fe3O4 nanoparticles. *ACS Applied Materials & Interfaces*. **2012**, *4*, 4991.

[17] J. Woo áLee, S. Bin áKim, Enhanced Cr (VI) removal using iron nanoparticle decorated graphene. *Nanoscale*. **2011**, *3*, 3583.

Appendix

The original data obtained by ICP-MS are listed in the following tables. The detection limit (DL) for selenium by ICP-MS is 0.0002 ppm.

Initial selenium concentration (ppm)	Selenium concentration after adsorption (ppm)
0.0385	0.0016
0.0883	0.0058
0.430	0.004
0.853	0.0032
4.13	0.0133
8.49	0.056
42.1	28.3
76.5	63.3

Appendix 1 Selenite concentration after adsorption with MGO with different initial selenite concentration. MGO dosage 1 g L^{-1}, under neutral pH (~ 6), room temperature (~ 25 ℃), shaking rate 300 rpm, adsorption time for 24 hours.

Initial selenium concentration (ppm)	Selenium concentration after adsorption (ppm)
0.0376	0.0085
0.0803	0.0229
0.421	0.114
0.784	0.369
4.06	2.03
8.39	5.39
37.5	28.3
75.1	65.6

Appendix 2 Selenate concentration after adsorption with MGO with different initial selenite concentration. MGO dosage 1 g L^{-1}, under neutral pH (~ 6), room temperature (~ 25 ℃), shaking rate 300 rpm, adsorption time for 24 hours.

pH	Selenium concentration after adsorption (ppm)
2.08	0.0020
2.99	0.0015
5.9	0.0004
6.98	0.0023
9.16	0.0006
10.32	0.0003
11.28	0.323

Appendix 3 Effect of pH on selenite adsorption: MGO dosage 1 g L^{-1}, initial selenium concentration 300 ppb room temperature (~ 25 ℃), shaking rate 300 rpm, adsorption time for 24 hours.

pH	Selenium concentration after adsorption (ppm)
2.05	0.0141
3.06	0.0168
5.43	0.0648
6.95	0.0734
9.39	0.102
10.31	0.260
11.34	0.354

Appendix 4 Effect of pH on selenate adsorption: MGO dosage 1 g L^{-1}, initial selenium concentration 300 ppb room temperature (~ 25 ℃), shaking rate 300 rpm, adsorption time for 24 hours.

Adsorption time	Selenium concentration after adsorption (ppm)
10 s	0.626
30 s	0.613
1 min	0.536
5 min	0.568
10 min	0.572
30 min	0.538
1 h	0.494
2 h	0.404
12 h	0.301
24 h	0.225

Appendix 5 Effect of adsorption time on selenite adsorption: MGO dosage 1 g L^{-1}, under neutral pH (~ 6), initial selenium concentration 300 ppb, room temperature (~ 25 ℃), shaking rate 300 rpm.

Adsorption time	Selenium concentration after adsorption (ppm)
10 s	0.0753
30 s	0.0764
1 min	0.0766
5 min	0.0776
10 min	0.0738
30 min	0.0488
1 h	0.0489
2 h	0.0426
12 h	0.0502
24 h	0.0516

Appendix 6 Effect of adsorption time on selenate adsorption: MGO dosage 1 g L^{-1}, under neutral pH (~ 6), initial selenium concentration 300 ppb, room temperature (~ 25 ℃), shaking rate 300 rpm.

Number of recycle times	Selenium removal ratio by reused MGO-EG (%)
1	0.0602
2	< DL
3	0.0009
4	0.0019
5	0.0023
6	0.0029
7	0.0025
8	0.0040
9	0.0044
10	0.0053

Appendix 7 Removal percentage of selenite with different recycle times. Recycle was done using acid-washing method. Tests were done at: MGO dosage 1 g L^{-1}, under neutral pH (~ 6), initial selenium concentration 300 ppb, room temperature (~ 25 ℃), shaking rate 300 rpm, adsorption time for 24 hours.

Number of recycle times	Selenium removal ratio by reused MGO-EG (%)
1	0.1470
2	0.2540
3	0.238
4	0.253
5	0.253
6	0.255
7	0.263
8	0.261
9	0.262
10	0.249

Appendix 8 Removal percentage of selenate with different recycle times. Recycle was done using acid-washing method. Tests were done at: MGO dosage 1 g L^{-1}, under neutral pH (~ 6), initial selenium concentration 300 ppb, room temperature (~ 25 ℃), shaking rate 300 rpm, adsorption time for 24 hours.

Initial selenium concentration (ppm)	Selenium concentration after adsorption (ppm)
< DL	< DL
0.0043	< DL
0.0086	< DL
0.0385	< DL
0.0883	< DL
0.430	< DL
0.853	< DL
4.13	0.0108
8.49	0.487
19.0	5.97
42.1	27.0
76.5	61.7
434	403
870	798

Appendix 9 Selenite concentration after adsorption with MGO-EG with different initial selenite concentration. MGO-EG dosage 1 g L^{-1}, under neutral pH (~ 6), room temperature (~ 25 ℃), shaking rate 300 rpm, adsorption time for 24 hours.

Initial selenium concentration (ppm)	Selenium concentration after adsorption (ppm)
0.0088	< DL
0.0042	< DL
0.0059	< DL
0.0376	0.0022
0.0803	0.0043
0.421	0.0439
0.784	0.104
4.06	2.00
8.39	6.10
15.1	10.1
37.5	29.8
75.1	64.6
433	407
861	804

Appendix 10 Selenate concentration after adsorption with MGO-EG with different initial selenate concentration. MGO-EG dosage 1 g L^{-1}, under neutral pH (~ 6), room temperature (~ 25 ℃), shaking rate 300 rpm, adsorption time for 24 hours.

pH before adsorption	pH after adsorption	Selenium concentration after adsorption (ppm)
2.27	2.24	< DL
2.78	2.84	< DL
4.78	4.22	< DL
5.20	4.53	< DL
6.05	4.71	< DL
7.41	4.88	< DL
9.16	5.25	< DL
9.81	5.37	< DL
10.13	7.06	< DL
11.35	10.85	0.275
11.76	11.62	0.287

Appendix 11 Effect of pH on selenite adsorption: MGO-EG dosage 1 g L^{-1}, initial selenium concentration 300 ppb room temperature (~ 25 ℃), shaking rate 300 rpm, adsorption time for 24 hours.

pH before adsorption	pH after adsorption	Selenium concentration after adsorption (ppm)
2.29	2.10	< DL
2.78	2.51	< DL
4.84	4.17	0.0064
5.85	4.24	0.0127
6.18	4.69	0.0195
7.00	4.70	0.0452
8.50	4.64	0.0492
9.08	4.92	0.0811
10.14	6.03	0.251
11.02	11.30	0.296
11.76	8.55	0.309

Appendix 12 Effect of pH on selenate adsorption: MGO-EG dosage 1 g L^{-1}, initial selenium concentration 300 ppb room temperature (~ 25 ℃), shaking rate 300 rpm, adsorption time for 24 hours.

Adsorption time	Selenium concentration after adsorption (ppm)
10 s	< DL
30 s	< DL
1 min	< DL
5 min	< DL
10 min	< DL
30 min	< DL
1 h	< DL
2 h	< DL
12 h	< DL
24 h	< DL

Appendix 13 Effect of adsorption time on selenite adsorption: MGO-EG dosage 1 g L^{-1}, under neutral pH (~ 6), initial selenium concentration 300 ppb, room temperature (~ 25 ℃), shaking rate 300 rpm.

Adsorption time	Selenium concentration after adsorption (ppm)
10 s	0.0242
30 s	< DL
1 min	0.0209
5 min	0.0199
10 min	0.0196
30 min	0.0163
1 h	0.0149
2 h	0.0074
12 h	0.0169
24 h	0.0100

Appendix 14 Effect of adsorption time on selenate adsorption: MGO-EG dosage 1 g L^{-1}, under neutral pH (~ 6), initial selenium concentration 300 ppb, room temperature (~ 25 ℃), shaking rate 300 rpm.

Adsorption temperature (℃)	Selenium concentration after adsorption (ppm)
4	< DL
6	< DL
10	< DL
15	< DL
20	< DL
25	< DL
30	< DL
35	< DL
40	< DL
50	< DL
60	< DL
70	< DL
80	< DL

Appendix 15 Effect of adsorption temperature on selenite adsorption: MGO-EG dosage 1 g L^{-1}, under neutral pH (~ 6), initial selenium concentration 300 ppb, shaking rate 300 rpm, adsorption time for 24 hours.

Adsorption temperature (℃)	Selenium concentration after adsorption (ppm)
4	0.0097
6	0.0104
10	0.0129
15	0.0131
20	0.0182
25	0.0197
30	0.0148
35	0.0166
40	0.0159
50	0.0213
60	0.0244
70	0.0303
80	0.0396

Appendix 16 Effect of adsorption temperature on selenate adsorption: MGO-EG dosage 1 g L^{-1}, under neutral pH (~ 6), initial selenium concentration 300 ppb, shaking rate 300 rpm, adsorption time for 24 hours.

Number of recycle times	Selenium removal ratio by reused MGO-EG (%)
1	> 99.93
2	> 99.93
3	> 99.93
4	> 99.93
5	> 99.93
6	> 99.93
7	> 99.93
8	> 99.93
9	> 99.93
10	99.65

Appendix 17 Removal percentage of selenite with different recycle times. Recycle was done using acid-washing method. Tests were done at: MGO-EG dosage 1 g L^{-1}, under neutral pH (~ 6), initial selenium concentration 300 ppb, room temperature (~ 25 ℃), shaking rate 300 rpm, adsorption time for 24 hours.

Number of recycle times	Selenium removal ratio by reused MGO-EG
1	> 99.93
2	> 99.93
3	> 99.93
4	> 99.93
5	99.51
6	99.71
7	> 99.93
8	> 99.93
9	> 99.93
10	99.75

Appendix 18 Removal percentage of selenate with different recycle times. Recycle was done using acid-washing method. Tests were done at: MGO-EG dosage 1 g L^{-1}, under neutral pH (~ 6), initial selenium concentration 300 ppb, room temperature (~ 25 °C), shaking rate 300 rpm, adsorption time for 24 hours.

Initial Ca^{2+} concentration (ppm)	Initial Se concentration (ppm)	Ca^{2+} concentration after adsorption (ppm)	Se concentration after adsorption (ppm)
7.75	0.251	7.56	< DL
14.9	0.251	14.5	< DL
35.2	0.245	34.4	< DL
68.7	0.248	66.8	< DL
131	0.258	130	< DL
306	0.257	308	< DL
632	0.261	633	0.0070
1270	0.273	1279	0.0262

Appendix 19 Selenite and Ca^{2+} removal percentage by MGO-EG with different initial Ca^{2+} concentrations. Tests were done at: MGO-EG dosage 1 g L^{-1}, under neutral pH (~ 6), initial selenium concentration 300 ppb, room temperature (~ 25 ℃), shaking rate 300 rpm, adsorption time for 24 hours.

Initial Ca^{2+} concentration (ppm)	Initial Se concentration (ppm)	Ca^{2+} concentration after adsorption (ppm)	Se concentration after adsorption (ppm)
7.35	0.257	7.49	0.0094
15.1	0.258	15.0	0.0110
35.8	0.256	34.6	< DL
69.2	0.259	68.3	0.0029
127	0.258	128	0.0123
322	0.263	315	0.0437
645	0.268	633	0.0971
1287	0.285	1293	0.181

Appendix 20 Selenate and Ca^{2+} removal percentage by MGO-EG with different initial Ca^{2+} concentrations. Tests were done at: MGO-EG dosage 1 g L^{-1}, under neutral pH (~ 6), initial selenium concentration 300 ppb, room temperature (~ 25 ℃), shaking rate 300 rpm, adsorption time for 24 hours.

Initial Mg^{2+} concentration (ppm)	Initial Se concentration (ppm)	Mg^{2+} concentration after adsorption (ppm)	Se concentration after adsorption (ppm)
9.98	0.247	10.1	< DL
19.94	0.254	20.0	< DL
49.2	0.258	49.9	< DL
99.0	0.255	101	< DL
209	0.259	206	0.0030
513	0.273	511	0.0152
1017	0.293	991	0.0283
2075	0.329	2016	0.0741

Appendix 21 Selenite and Mg^{2+} removal percentage by MGO-EG with different initial Mg^{2+} concentrations. Tests were done at: MGO-EG dosage 1 g L^{-1}, under neutral pH (~ 6), initial selenium concentration 300 ppb, room temperature (~ 25 ℃), shaking rate 300 rpm, adsorption time for 24 hours.

Initial Mg^{2+} concentration (ppm)	Initial Se concentration (ppm)	Mg^{2+} concentration after adsorption (ppm)	Se concentration after adsorption (ppm)
10.0	0.243	9.48	0.0165
21.6	0.247	21.2	0.0325
51.8	0.250	51.4	0.0333
97.6	0.243	99.2	0.0507
211	0.248	207	0.0766
525	0.263	518	0.145
1059	0.293	1040	0.213
2152	0.336	2123	0.299

Appendix 22 Selenate and Mg^{2+} removal percentage by MGO-EG with different initial Mg^{2+} concentrations. Tests were done at: MGO-EG dosage 1 g L^{-1}, under neutral pH (~ 6), initial selenium concentration 300 ppb, room temperature (~ 25 ℃), shaking rate 300 rpm, adsorption time for 24 hours.

Initial NO_3^- concentration (ppm)	Initial Se concentration (ppm)	NO_3^- concentration after adsorption (ppm)	Se concentration after adsorption (ppm)
11.34	0.253	10.98	< DL
22.45	0.259	21.35	< DL
54.12	0.246	52.17	< DL
107.1	0.260	103.6	< DL
206.6	0.264	201.4	< DL
517.7	0.261	506	< DL
1096	0.263	1008	< DL
2241	0.258	2229	< DL

Appendix 23 Selenite and NO_3^- removal percentage by MGO-EG with different initial NO_3^- concentrations. Tests were done at: MGO-EG dosage 1 g L^{-1}, under neutral pH (~ 6), initial selenium concentration 300 ppb, room temperature (~ 25 ℃), shaking rate 300 rpm, adsorption time for 24 hours.

Initial NO_3^- concentration (ppm)	Initial Se concentration (ppm)	NO_3^- concentration after adsorption (ppm)	Se concentration after adsorption (ppm)
8.77	0.256	8.90	0.0022
20.90	0.260	21.43	0.0119
51.50	0.264	57.88	0.0227
114.9	0.260	114.48	0.0258
199.0	0.258	197.5	0.0300
641.3	0.259	626.2	0.0480
1093	0.263	1072	0.0688
2224	0.258	2206	0.0681

Appendix 24 Selenate and NO_3^- removal percentage by MGO-EG with different initial NO_3^- concentrations. Tests were done at: MGO-EG dosage 1 g L^{-1}, under neutral pH (~ 6), initial selenium concentration 300 ppb, room temperature (~ 25 ℃), shaking rate 300 rpm, adsorption time for 24 hours.

Initial SO_4^{2-} concentration (ppm)	Initial Se concentration (ppm)	SO_4^{2-} concentration after adsorption (ppm)	Se concentration after adsorption (ppm)
5.04	0.283	5.25	< DL
13.7	0.256	13.14	< DL
31.2	0.254	28.23	0.0009
81.3	0.265	73.99	0.212
157.1	0.252	142.9	0.0010
285.9	0.258	330.6	0.0011
769.3	0.258	778.0	0.0013
1675.2	0.262	1344.7	< DL

Appendix 25 Selenite and SO_4^{2-} removal percentage by MGO-EG with different initial SO_4^{2-} concentrations. Tests were done at: MGO-EG dosage 1 g L^{-1}, under neutral pH (~ 6), initial selenium concentration 300 ppb, room temperature (~ 25 ℃), shaking rate 300 rpm, adsorption time for 24 hours.

Initial SO_4^{2-} concentration (ppm)	Initial Se concentration (ppm)	SO_4^{2-} concentration after adsorption (ppm)	Se concentration after adsorption (ppm)
5.58	0.265	5.61	0.0936
10.9	0.259	11.10	0.140
28	0.257	27.36	0.194
78.6	0.252	73.42	0.222
154.4	0.269	144.2	0.247
291.4	0.270	336.6	0.258
764.2	0.274	748.9	0.267
1607.1	0.268	1367.7	0.257

Appendix 26 Selenate and SO_4^{2-} removal percentage by MGO-EG with different initial SO_4^{2-} concentrations. Tests were done at: MGO-EG dosage 1 g L^{-1}, under neutral pH (~ 6), initial selenium concentration 300 ppb, room temperature (~ 25 ℃), shaking rate 300 rpm, adsorption time for 24 hours.

Initial PO_4^{3-} concentration (ppm)	Initial Se concentration (ppm)	PO_4^{3-} concentration after adsorption (ppm)	Se concentration after adsorption (ppm)
0.0142	0.234	0.0149	< DL
0.0160	0.232	0.0163	< DL
0.0325	0.237	0.0151	< DL
0.0384	0.240	0.0145	< DL
0.152	0.241	0.0149	< DL
0.294	0.242	0.0143	< DL
1.44	0.250	0.0161	< DL

Appendix 27 Selenite and PO_4^{3-} removal percentage by MGO-EG with different initial PO_4^{3-} concentrations. Tests were done at: MGO-EG dosage 1 g L^{-1}, under neutral pH (~ 6), initial selenium concentration 300 ppb, room temperature (~ 25 ℃), shaking rate 300 rpm, adsorption time for 24 hours.

Initial PO_4^{3-} concentration (ppm)	Initial Se concentration (ppm)	PO_4^{3-} concentration after adsorption (ppm)	Se concentration after adsorption (ppm)
0.0134	0.251	0.0161	< DL
0.0152	0.247	0.0144	< DL
0.0299	0.251	0.0165	< DL
0.0434	0.250	0.0157	< DL
0.175	0.249	0.0160	< DL
0.337	0.250	0.0135	0.0033
1.62	0.258	0.0180	0.201

Appendix 28 Selenate and PO_4^{3-} removal percentage by MGO-EG with different initial PO_4^{3-} concentrations. Tests were done at: MGO-EG dosage 1 g L^{-1}, under neutral pH (~ 6), initial selenium concentration 300 ppb, room temperature (~ 25 ℃), shaking rate 300 rpm, adsorption time for 24 hours.

Initial pH	pH after adsorption	Initial Ca^{2+} concentration (ppm)	Ca^{2+} concentration after adsorption (ppm)	Se concentration after adsorption (ppm)
1.36	4.84	15.5	15.7	< DL
2.12	2.07	15.5	15.5	0.0018
3.32	3.32	15.5	15.7	< DL
4.01	3.88	15.5	15.6	< DL
5.19	4.28	15.5	15.7	< DL
6.23	4.54	15.5	15.6	< DL
6.87	4.94	15.5	15.4	0.0009
8.23	4.68	15.5	15.5	0.0009
9.33	5.29	15.5	15.4	< DL
9.87	7.28	15.5	14.4	0.0072
10.89	7.43	15.5	10.3	0.0024
11.84	11.96	15.5	0.661	0.243

Appendix 29 Selenite and Ca^{2+} removal percentage by MGO-EG with different pH. Tests were done at: MGO-EG dosage 1 g L^{-1}, initial selenium concentration 300 ppb, room temperature (~ 25 ℃), shaking rate 300 rpm, adsorption time for 24 hours.

Initial pH	pH after adsorption	Initial Ca^{2+} concentration (ppm)	Ca^{2+} concentration after adsorption (ppm)	Se concentration after adsorption (ppm)
1.35	1.58	15.4	14.6	0.0139
2.26	2.29	15.4	15.4	0.0026
2.98	3.02	15.4	15.6	0.0015
3.96	3.90	15.4	15.7	0.0118
5.02	4.36	15.4	15.6	0.0322
6.19	4.81	15.4	15.3	0.0529
6.77	5.07	15.4	15.3	0.0503
7.64	5.03	15.4	15.5	0.0549
8.81	5.65	15.4	15.2	0.116
9.72	6.23	15.4	15.0	0.209
10.84	7.47	15.4	8.44	0.258
11.88	11.84	15.4	0.741	0.261

Appendix 30 Selenate and Ca^{2+} removal percentage by MGO-EG with different pH. Tests were done at: MGO-EG dosage 1 g L^{-1}, initial selenium concentration 300 ppb, room temperature (~ 25 ℃), shaking rate 300 rpm, adsorption time for 24 hours.

Initial pH	pH after adsorption	Initial Mg^{2+} concentration (ppm)	Mg^{2+} concentration after adsorption (ppm)	Se concentration after adsorption (ppm)
1.25	1.43	19.94	18.7	0.0109
2.19	2.10	19.94	20.0	0.0017
3.15	3.16	19.94	20.3	< DL
4.02	3.99	19.94	20.8	< DL
4.84	4.44	19.94	20.6	< DL
6.08	4.88	19.94	20.5	< DL
7.08	4.97	19.94	20.4	< DL
8.03	5.75	19.94	20.8	< DL
8.91	5.90	19.94	20.3	< DL
10.28	5.16	19.94	20.4	< DL
10.83	7.20	19.94	16.8	0.0040
11.87	11.86	19.94	0.121	0.249

Appendix 31 Selenite and Mg^{2+} removal percentage by MGO-EG with different pH. Tests were done at: MGO-EG dosage 1 g L^{-1}, initial selenium concentration 300 ppb, room temperature (~ 25 ℃), shaking rate 300 rpm, adsorption time for 24 hours.

Initial pH	pH after adsorption	Initial Mg^{2+} concentration (ppm)	Mg^{2+} concentration after adsorption (ppm)	Se concentration after adsorption (ppm)
1.22	1.35	21.6	18.9	0.0165
2.23	2.09	21.6	20.3	0.0023
3.11	3.12	21.6	20.3	< DL
3.91	3.92	21.6	20.9	0.0011
5.00	4.39	21.6	20.6	0.0046
6.16	4.92	21.6	20.3	0.0173
7.10	4.84	21.6	20.3	0.0169
8.12	5.05	21.6	19.8	0.0312
9.01	5.70	21.6	20.0	0.131
10.22	6.75	21.6	19.0	0.259
10.90	7.62	21.6	14.7	0.266
11.78	11.83	21.6	0.045	0.259

Appendix 32 Selenate and Mg^{2+} removal percentage by MGO-EG with different pH. Tests were done at: MGO-EG dosage 1 g L^{-1}, initial selenium concentration 300 ppb, room temperature (~ 25 ℃), shaking rate 300 rpm, adsorption time for 24 hours.

Initial pH	pH after adsorption	Initial NO_3^- concentration (ppm)	NO_3^- concentration after adsorption (ppm)	Se concentration after adsorption (ppm)
1.20	1.18	22.45	19.8	0.0206
2.28	2.27	22.45	22.8	0.0016
2.85	2.77	22.45	21.7	< DL
4.20	4.01	22.45	19.2	< DL
5.23	4.41	22.45	19.3	< DL
5.90	5.00	22.45	20.1	< DL
6.60	4.84	22.45	19.9	< DL
7.42	5.10	22.45	20.2	< DL
9.24	5.07	22.45	19.8	< DL
10.00	6.75	22.45	19.0	< DL
11.00	7.50	22.45	21.4	0.0802
11.95	11.56	22.45	21.7	0.237

Appendix 33 Selenite and NO_3^- removal percentage by MGO-EG with different pH. Tests were done at: MGO-EG dosage 1 g L^{-1}, initial selenium concentration 300 ppb, room temperature (~ 25 ℃), shaking rate 300 rpm, adsorption time for 24 hours.

Initial pH	pH after adsorption	Initial NO_3^- concentration (ppm)	NO_3^- concentration after adsorption (ppm)	Se concentration after adsorption (ppm)
1.29	1.22	20.9	20.6	0.0226
1.91	1.78	20.9	23.0	0.0036
2.84	2.82	20.9	20.5	0.0010
3.74	2.62	20.9	19.2	0.0035
5.22	4.32	20.9	17.8	0.0200
6.22	4.57	20.9	19.3	0.0334
7.17	4.75	20.9	20.7	0.0579
7.78	5.16	20.9	20.2	0.0751
9.24	5.82	20.9	19.4	0.121
10.24	6.43	20.9	20.4	0.211
10.86	7.48	20.9	23.6	0.251
11.84	11.4	20.9	21.2	0.238

Appendix 34 Selenate and NO_3^- removal percentage by MGO-EG with different pH. Tests were done at: MGO-EG dosage 1 g L^{-1}, initial selenium concentration 300 ppb, room temperature (~ 25 ℃), shaking rate 300 rpm, adsorption time for 24 hours.

Initial pH	pH after adsorption	Initial SO_4^{2-} concentration (ppm)	SO_4^{2-} concentration after adsorption (ppm)	Se concentration after adsorption (ppm)
1.29	1.36	31.2	21.726	0.0159
2.17	2.01	31.2	24.174	0.0021
3.19	3.32	31.2	32.844	0.0008
4.00	4.14	31.2	20.4	0.0007
4.94	4.49	31.2	16.779	0.0007
5.92	4.70	31.2	23.001	0.0007
6.66	4.90	31.2	24.684	0.0009
7.73	6.39	31.2	27.999	0.0017
8.60	5.68	31.2	28.254	< DL
10.47	7.10	31.2	31.773	0.0016
11.51	7.61	31.2	56.661	0.213
12.29	12.04	31.2	46.308	0.234

Appendix 35 Selenite and SO_4^{2-} removal percentage by MGO-EG with different pH. Tests were done at: MGO-EG dosage 1 g L^{-1}, initial selenium concentration 300 ppb, room temperature (~ 25 ℃), shaking rate 300 rpm, adsorption time for 24 hours.

Initial pH	pH after adsorption	Initial SO_4^{2-} concentration (ppm)	SO_4^{2-} concentration after adsorption (ppm)	Se concentration after adsorption (ppm)
1.30	1.42	28	24.276	0.0236
2.10	2.01	28	23.715	0.0205
2.86	2.68	28	27.081	0.0352
4.12	4.09	28	17.544	0.0976
5.01	4.42	28	21.624	0.129
5.84	4.62	28	22.491	0.130
7.09	4.87	28	27.132	0.105
8.02	5.07	28	29.478	0.152
8.74	5.10	28	27.999	0.158
10.16	6.33	28	32.946	0.214
11.27	8.15	28	51.306	0.265
12.11	11.99	28	49.98	0.261

Appendix 36 Selenate and SO_4^{2-} removal percentage by MGO-EG with different pH. Tests were done at: MGO-EG dosage 1 g L^{-1}, initial selenium concentration 300 ppb, room temperature (~ 25 ℃), shaking rate 300 rpm, adsorption time for 24 hours.

Initial pH	pH after adsorption	Initial PO_4^{3-} concentration (ppm)	PO_4^{3-} concentration after adsorption (ppm)	Se concentration after adsorption (ppm)
1.20	1.47	20.01	< DL	0.0096
2.06	2.09	20.01	< DL	0.0021
3.25	3.45	20.01	< DL	0.0014
4.24	4.59	20.01	2.91	0.0060
4.85	5.63	20.01	2.94	0.0086
6.23	5.73	20.01	5.18	0.0144
7.03	6.62	20.01	9.18	0.0530
8.31	7.25	20.01	13.02	0.0754
9.03	7.25	20.01	13.36	0.0744
10.33	7.67	20.01	17.04	0.0864
11.04	8.50	20.01	28.22	0.229
12.01	12.35	20.01	31.53	0.245

Appendix 37 Selenite and PO_4^{3-} removal percentage by MGO-EG with different pH. Tests were done at: MGO-EG dosage 1 g L^{-1}, initial selenium concentration 300 ppb, room temperature (~ 25 ℃), shaking rate 300 rpm, adsorption time for 24 hours.

Initial pH	pH after adsorption	Initial PO_4^{3-} concentration (ppm)	PO_4^{3-} concentration after adsorption (ppm)	Se concentration after adsorption (ppm)
1.32	1.39	19.99	< DL	0.0421
2.24	2.05	19.99	< DL	0.0296
3.20	3.04	19.99	< DL	0.116
3.92	3.96	19.99	< DL	0.219
5.12	4.47	19.99	< DL	0.249
6.36	5.90	19.99	2.10	0.252
7.32	5.80	19.99	3.44	0.260
8.34	6.24	19.99	5.91	0.257
9.17	6.37	19.99	6.71	0.259
10.13	7.28	19.99	9.71	0.256
10.93	6.94	19.99	21.57	0.257
11.98	12.09	19.99	31.60	0.260

Appendix 38 Selenate and PO_4^{3-} removal percentage by MGO-EG with different pH. Tests were done at: MGO-EG dosage 1 g L^{-1}, initial selenium concentration 300 ppb, room temperature (~ 25 ℃), shaking rate 300 rpm, adsorption time for 24 hours.

Initial Se concentration (ppm)	Final Se concentration (ppm) (measurement 1)	Final Se concentration (ppm) (measurement 2)	Final Se concentration (ppm) (measurement 3)
10	0.322	0.174	0.2033
5	0.0485	0.013	0.016
1	0.004	0.0007	0.0023
0.5	< DL	0.005	0.0008
0.1	0.0002	0.0014	< DL
0.05	< DL	0.0009	< DL
0.01	< DL	0.0003	0.0006
0.005	< DL	0.0003	0.0002
10	0.322	0.174	0.2033

Appendix 39 Selenite concentration after adsorption with MGO-EG with different initial selenite concentration. MGO-EG dosage 1 g L^{-1}, under neutral pH (~ 6), room temperature (~ 25 ℃), shaking rate 300 rpm, adsorption time for 24 hours.

Initial Se concentration (ppm)	Final Se concentration (ppm) (measurement 1)	Final Se concentration (ppm) (measurement 2)	Final Se concentration (ppm) (measurement 3)
10	0.669	0.186	0.588
5	0.357	0.048	0.1025
1	0.065	0.0356	0.0759
0.5	0.033	0.0199	0.0272
0.1	0.0086	0.0125	0.0102
0.05	0.0049	0.0070	0.0080
0.01	0.0050	0.0045	0.0052
0.005	0.0036	0.0034	0.0039
10	0.669	0.186	0.588

Appendix 40 Selenate concentration after adsorption with MGO-EG with different initial selenite concentration. MGO-EG dosage 1 g L^{-1}, under neutral pH (~ 6), room temperature (~ 25 ℃), shaking rate 300 rpm, adsorption time for 24 hours.

Initial Se concentration (ppm)	Final Se concentration (ppm) (measurement 1)	Final Se concentration (ppm) (measurement 2)	Final Se concentration (ppm) (measurement 3)
10	0.4	1.167	3.6
5	0.1	0.5925	0.9
1	0.016	0.0303	0.051
0.5	0.0191	0.0294	0.0390
0.1	0.0016	0.0005	0.0003
0.05	0.0003	0.0002	< DL
0.01	< DL	< DL	< DL
0.005	< DL	< DL	< DL
10	0.4	1.167	3.6

Appendix 41 Selenite concentration after adsorption with MGO with different initial selenite concentration. MGO dosage 1 g L^{-1}, under neutral pH (~ 6), room temperature (~ 25 ℃), shaking rate 300 rpm, adsorption time for 24 hours.

Initial Se concentration (ppm)	Final Se concentration (ppm) (measurement 1)	Final Se concentration (ppm) (measurement 2)	Final Se concentration (ppm) (measurement 3)
10	6.4	7.411	8.2
5	0.6956	1.3755	2
1	0.1410	0.1963	0.1701
0.5	0.1035	0.1057	0.1349
0.1	0.0213	0.0247	0.0224
0.05	0.0182	0.0169	0.0202
0.01	0.0044	0.0042	0.0036
0.005	0.0028	0.0025	0.0027

Appendix 42 Selenate concentration after adsorption with MGO with different initial selenite concentration. MGO dosage 1 g L^{-1}, under neutral pH (~ 6), room temperature (~ 25 ℃), shaking rate 300 rpm, adsorption time for 24 hours.

Initial Se concentration (ppm)	Final Se concentration (ppm) (measurement 1)	Final Se concentration (ppm) (measurement 2)	Final Se concentration (ppm) (measurement 3)
10	9.386	10.5	9.258
5	4.529	4.5571	4.4855
1	0.8882	0.8950	0.8918
0.5	0.4599	0.4496	0.4509
0.1	0.0893	0.0863	0.0895
0.05	0.0454	0.0446	0.0454
0.01	0.0084	0.0087	0.0085
0.005	0.0043	0.0044	0.0042

Appendix 43 Selenite concentration after adsorption with GO with different initial selenite concentration. GO dosage 1 g L^{-1}, under neutral pH (~ 6), room temperature (~ 25 ℃), shaking rate 300 rpm, adsorption time for 24 hours.

Initial Se concentration (ppm)	Final Se concentration (ppm) (measurement 1)	Final Se concentration (ppm) (measurement 2)	Final Se concentration (ppm) (measurement 3)
10	10.02	2.2376	9.494
5	5.00	2.9664	4.9145
1	0.851	12.018	0.8405
0.5	0.4059	14.178	0.4033
0.1	0.0772	15.993	0.0741
0.05	0.0349	19.327	0.0343
0.01	0.0072	17.515	0.0071
0.005	0.0037	16.516	0.0036

Appendix 44 Selenate concentration after adsorption with GO with different initial selenite concentration. GO dosage 1 g L^{-1}, under neutral pH (~ 6), room temperature (~ 25 ℃), shaking rate 300 rpm, adsorption time for 24 hours.

Initial Se concentration (ppm)	Final Se concentration (ppm) (measurement 1)	Final Se concentration (ppm) (measurement 2)	Final Se concentration (ppm) (measurement 3)
10	9	8.3679	8.783
5	4	3.9134	3.9235
1	0.778	0.6917	0.7706
0.5	0.3985	0.3770	0.3895
0.1	0.0814	0.0778	0.0815
0.05	0.0436	0.0382	0.0411
0.01	0.0093	0.0084	0.0089
0.005	0.0048	0.0045	0.0047

Appendix 45 Selenite concentration after adsorption with Fe_3O_4 (400 nm) with different initial selenite concentration. Fe_3O_4 (400 nm) dosage 1 g L^{-1}, under neutral pH (~ 6), room temperature (~ 25 ℃), shaking rate 300 rpm, adsorption time for 24 hours.

Initial Se concentration (ppm)	Final Se concentration (ppm) (measurement 1)	Final Se concentration (ppm) (measurement 2)	Final Se concentration (ppm) (measurement 3)
10	10.13	9.4611	8.933
5	4.75	4.2841	4.491
1	0.94	0.8783	0.905
0.5	0.49	0.4484	0.455
0.1	0.0977	0.0921	0.0897
0.05	0.0470	0.0443	0.0458
0.01	0.0095	0.0089	0.0093
0.005	0.0049	0.0045	0.0047

Appendix 46 Selenate concentration after adsorption with Fe_3O_4 (400 nm) with different initial selenite concentration. Fe_3O_4 (400 nm) dosage 1 g L^{-1}, under neutral pH (~ 6), room temperature (~ 25 ℃), shaking rate 300 rpm, adsorption time for 24 hours.

Initial Se concentration (ppm)	Final Se concentration (ppm) (measurement 1)	Final Se concentration (ppm) (measurement 2)	Final Se concentration (ppm) (measurement 3)
10	0.4	0.9638	0.284
5	0.1	0.1240	0.099
1	0.004	0.0517	0.0015
0.5	0.001	0.0121	0.0036
0.1	<DL	0.0014	0.0006
0.05	<DL	0.0006	<DL
0.01	<DL	0.0004	<DL
0.005	0.0003	0.0004	0.0003

Appendix 47 Selenite concentration after adsorption with Fe_3O_4 (10 - 20 nm) with different initial selenite concentration. Fe_3O_4 (10 - 20 nm) dosage 1 g L^{-1}, under neutral pH (~ 6), room temperature (~ 25 ℃), shaking rate 300 rpm, adsorption time for 24 hours.

Initial Se concentration (ppm)	Final Se concentration (ppm) (measurement 1)	Final Se concentration (ppm) (measurement 2)	Final Se concentration (ppm) (measurement 3)
10	5.4	5.107	5.853
5	3.6	3.3553	3.6815
1	0.7578	0.6933	0.7004
0.5	0.3761	0.3662	0.3974
0.1	0.0817	0.0758	0.0742
0.05	0.0402	0.0383	0.0401
0.01	0.0085	0.0079	0.0081
0.005	0.0042	0.0045s	0.0042

Appendix 48 Selenate concentration after adsorption with Fe_3O_4 (10 - 20 nm) with different initial selenite concentration. Fe_3O_4 (10 - 20 nm) dosage 1 g L^{-1}, under neutral pH (~ 6), room temperature (~ 25 ℃), shaking rate 300 rpm, adsorption time for 24 hours.